Study and implementation of beam lines and devices for the acceleration, transport and manipulation of laser-accelerated particle beams

Thesis for obtaining the degree of Philosophiae Doctor (Ph.D.)

University of Rome "La Sapienza", department of physics

–

Institut National de la Recherche Scientifique, centre Énergie Matériaux Télécommunications

Scientific supervisors:

Luigi Palumbo
Patrizio Antici

Evaluators:

Emmanuel D'Humières
Danilo Giulietti

Ph.D. candidate:

Massimiliano Sciscìò

Accademic year 2016/2017

Table of contents

Foreword

Undertaking the path of academic research as an alternative to a more conventional professional position as an engineer has not been straightforwardly planned, easy choice.
After having graduated from my Master's degree, in July 2013, I did two promising job interviews and nothing seemed to lead me to extending my university studies further. What I had not taken into account were the persuasive skills of Patrizio Antici who had been my thesis supervisor for the previous six months. He had made me familiar with the topic of proton acceleration via laser-plasma interaction and collaborating with him had given very good results. During a lunch break at the department of Applied Science for Engineering of the university of Rome "La Sapienza" we had the conversation that would have determined the following three and a half years of my life, at least from the scientific point of view. He told me about the interesting prospects of continuing the work that we had started together and suggested me to apply for a doctoral student position at "La Sapienza". My journey through diverging electron beams and unreliable proton sources, too high emittances and unwieldy beam lines, unclear manuscripts and fussy referees, had just begun. The collaboration with Patrizio became even stronger about one year later, as he accepted to become my thesis supervisor at the Institut National de la Recherche Scientifique, when I signed an agreement for an Italian-Canadian joint doctorate.
Doing my Ph.D. under Patrizio's direction has been an extremely rewarding experience, from the scientific and personal point of view, that I would repeat at any time. This is the reason why the first acknowledgment spontaneously goes to Patrizio, for having guided me throughout these years, for having given me some hard and challenging times but also often enjoyable and amusing moments, for the many advises and the mentoring, and for the continuous support he has given and still is giving me today. I truly thank him for everything.

My doctoral studies would not have been possible without the endorsement and the supervision of Prof. Luigi Palumbo, the thesis director at my home university in Rome. He has welcomed me in his research group and has always supported my work and my initiatives, driving me to the pursuit of valuable scientific results and cultural growth.

During this experience I have had the possibility of cooperating with the particle accelerator group of "La Sapienza", learning from some of the best scientists operating in this field. It is impossible to list them all, but among them, I would like to thank especially Mauro Migliorati, Andrea Mostacci, Livia Lancia and Luca Ficcadenti, who I have had the pleasure to work with in a continuous way.

I would like to thank the staff members of the Canadian institute INRS, the partner university for the joint supervision of my Ph.D., I have had the honor to collaborate with. Among them, a special thank goes to Prof. Kieffer, Dr. Fourmaux and Dr. Payeur.

I warmly thank Prof. Giulietti and Prof. D'Humières for having evaluated this thesis and having given me useful advises for improving its quality.

For the scientific collaborations and the many delightful moments spent together, for example when running the experiments during the last period of my doctorate, I truly thank Marianna Barberio of the university UniCal. She has been more than a collaborator to me: by helping me with all the issues related to material science applications of this work, she became almost an additional supervisor and definitely a dear friend. For all what she has done for me, she has my deepest gratitude.

The last three years would not have been as delightful as they have, without the companionship of my fellow doctoral students. An enormous thank goes to all of them: Anna, Francesco, Martina, Stefano and Marco, the other Ph.D. students at “La Sapienza”; Simona and Antonia from UniCal and ELI-Hu; Giacomo, Alessandro, Alessandra, Matteo, Riccardo, Rajesh, Marta and Andrea from INRS. A profuse thank to the friends who stood by my side from outside of the academic world: Francesco, Roberta, Oliviero, Alessia, Alessandro, Francesca, Alessandro, Andrea and many others. Last but not least, I thank Fabio…after the Bachelor’s and Master’s degree, this Ph.D. is the ultimate course of study that we have undertaken together, as good, true friends.

Finally, the most heartfelt thank goes to my family, my mother and my father, my siblings, for having supported my choices once again, for having made sacrifices and loving me for what I am. All this allowed me to pursue my studies and educational growth. Most of all, I heartily thank Jennyfer, for having been the closest and beloved person I have had in these years.

Without the persons I have mentioned, this work would not have been possible. There are many others, I might have forgotten: my ultimate thank goes to them.

I acknowledge the financial and institutional support that I have received from academic and scientific establishments during the period of my Ph.D. studies. Therefore, I thank the Istituto Nazionale di Fisica Nucleare (INFN) for having granted me with a full scholarship, the University of Rome “La Sapienza”, the Insititut National de la Recherche Scientifique - Énergie Matériaux Télécommunications (INRS-EMT), the Lawrence Livermore National Laboratories (LLNL), the European Scientific Institute (ESI) and the ELI-NP project.

This manuscript is written in American English and it includes a translation in French of the thesis’ executive summary. Since the work I report of has been performed as a group, I use “we” instead of “I” throughout almost all parts of this document where the scientific results are discussed. The figures, the equations and the tables have a separate numbering for each chapter. The same applies to the bibliographic references that are listed at the end of the single chapters.

Might the reader have a pleasurable reading of this thesis.

Rome, February 2017

Executive summary

The study of laser-driven particle beams represents an important field in nowadays research, both from the theoretical and experimental point of view.
Differently from conventional, radio-frequency (RF) technology-based accelerators, laser-driven particle sources accelerate particles (both electrons and ions) with electric fields that are generated by the interaction of intense laser pulses (>$10^{18}\ W \cdot cm^{-2}$) and matter. TW-power class laser systems, or even novel PW-power class systems, can produce a plasma where electric fields are generated that allow accelerating particles over very short distances. The accelerating field reaches up to TV/m over a few µm in the case of proton acceleration and up to tens of GV/m over hundreds of µm in the case of electron acceleration. This allows overcoming the limits of conventional accelerating schemes based on RF fields, which are limited to accelerating gradients in the range of MV/m (up to ∼100 MV/m for the state-of-the-art technology), due to electric breakdown effects.
At current, laser-accelerated electrons have reached maximum energies in the range of a few GeV, whereas for protons, tens of MeV energy beams are routinely achievable.

The features of laser-generated particle beams, in terms of energy, bunch charge, bunch duration and laminarity, enable these sources to be considered as a potential alternative to conventional particle sources. Applications such as Free Electron Lasers (FEL) for the case of electrons or Ion Beam Analysis (IBA) for the case of protons, are readily exploitable with the beam energies that are available today. However, some parameters of laser-driven beams, such as the large energy spread (a few percent for electrons and up to 100 % for protons) and strong divergence at the source (a few mrad for electrons and fractions of radiant for protons) represent an obstacle for having reliable, controlled beams that can be implemented for these applications. For these reasons, the transport, the tailoring and the manipulation of the laser driven particle bunch is challenging but necessary.

The objective of this work is to study the implementation of conventional accelerator devices for laser-driven particle beam lines. Focusing devices such as solenoids and quadrupoles and other components such as RF accelerating cavities, or beam energy-selection systems allow transporting and manipulating the particle beam from the initial source to the experimental end station. They are commonly used on conventional facilities and can be adapted and optimized to the parameters of typical laser-plasma particle sources, leading to improved performances of the laser-driven beam lines. Studying these beam lines can yield to novel beam shaping techniques, opening the path to innovative applications.

For analysing these laser-driven beam lines we adopted the same methodology as used for conventional accelerators. We have involved the use of numerical codes for the analysis of beam dynamics problems, aiming at optimizing the laser-driven beam lines' components. Using different simulation tools, we have implemented an iteration process that allows improving the performance of the beam lines by recursively optimizing the particle beam parameters and the features of the beam line's elements.

We address both, electron and proton beam lines, studying the following aspects: for laser-driven electron beam lines, we indicate goal parameters that a laser-plasma electron source needs to achieve in order to allow a beam transport line that maintains the quality of the initial electron bunch, enabling FEL applications. We consider the RMS normalized emittance and the transverse dimension of the beam as key performance indicators for these applications.
Concerning laser-accelerated proton beams, we propose a beam line configuration, capable of lowering the energy spread of the bunch to a few tens percent, keeping a reasonably high particle flux. We aim at obtaining final beam parameters that allow implementing applications of IBA.

The first section of the thesis is devoted to the analysis of laser-driven electron beam lines. We propose the use of conventional accelerator magnetic devices (such as quadrupoles and solenoids) as an easy implementable solution when the laser-plasma accelerated beam requires to be transported and optimized.
The implementation of the conventional beam line's devices has been studied with a parametric approach, employing particle optics and particle tracking codes that analyze the transport and the geometric shaping of the electron beam. We focus on both, high energy electron beams in the GeV range (8 GeV, as theoretically foreseen by simulations), as produced on petawatt (PW) class laser systems, and on lower energy electron beams in the hundreds of MeV range (350 MeV), as nowadays routinely obtained on commercially available multi-hundred TW laser systems. For both scenarios, our study allows understanding what are the crucial parameters that enable laser-plasma accelerators to compete with conventional ones and allow for a beam transport.
We analyze different configurations of beam lines, from a simple quadrupole triplet to more complex symmetric (and even achromatic) lattice structures, testing their beam transport efficiency in terms of the final normalized RMS emittance and transverse beam dimension. Implementing focusing elements that provide a magnetic focusing gradient in the range of hundreds of T/m, we aim at compensating the intrinsic divergence of the electron beam, which is in the range of several mrad. Furthermore, we compare the final beam emittance of the laser-accelerated electrons to what is obtainable with conventional accelerators that are used to drive FEL sources.
Considering the case of electrons accelerated to 350 MeV, we aim to achieve competitive values implementing a transport line based on a quadrupole triplet lattice. We identify the requirements at the laser-plasma source (in terms of energy spread and transverse divergence) that the electron beam needs to meet in order to compete with conventional FEL sources. The numerical calculations we report, show that suitable working points require a trade-off combination between low beam divergence and narrow energy spread: the laser-accelerated electron beam needs to have a divergence of $\leq$1 mrad and an energy spread of $\leq$1 % in order to be transported and maintain a reasonable normalized RMS emittance value of $\sim$1 mm mrad, i.e. the typical working point parameter of conventional FEL driving accelerators.

The second section of this work deals with laser-driven proton beam lines. The possibility of combining an energy selection device (ES) for lowering the energy spread of the particles, with a focusing stage that captures and transports the beam from the laser-plasma source, has been

studied. Considering the parameters required by IBA applications, we aim to achieve a final energy spread of a few tens percent and a high bunch charge (in the nC range).
For the initial proton beam (i.e. at the source), we took as reference the typical parameters achievable with the most consolidated acceleration mechanism, the so-called Target Normal Sheath Acceleration (TNSA) mechanism. This mechanism routinely produces proton beams with an energy in the order of tens of MeV, a high beam charge (up to 10^{13} protons per shot) and a short bunch duration (in the ps range, at the laser-plasma source), using commercial TW-power class laser systems, representing a complementary solution to conventional sources for several applications. Nevertheless, the broadband energy spectrum of TNSA generated protons (up to 100 %) is an open issue that limits experiments and applications that require monochromatic proton beams.
Our study is based on beam dynamics and particle tracking simulations, with the goal of analyzing and developing a beam line for laser-driven proton beams, including devices for energy selection and beam focusing: a beam line made of compact permanent magnet quadrupoles (PMQ) transports the proton beam from the laser-plasma source to a magnetic chicane made with permanent magnets that accounts for the energy selection of the beam.
The range of energy we investigate goes from 2 to 20 MeV, i.e. the energies that can be obtained for ion acceleration using a commercial 250 TW-power laser system and are typical of many applications in IBA. The key technical features of the energy-selector have been studied in a parametric way, in order to allow an optimization of the device in the energy range of interest. An optimized solution of the ES is based on $\sim$0.95 T dipoles with a length of 10 cm and provides a final energy spread of $\sim$20 %.
As next step, for this ES we adapt the beam line upstream the selection device for tuning the transmission efficiency of the protons. Lowering the divergence of the protons is necessary for allowing an efficient energy selection process: we have estimated the required divergence to be of a few mrad. With the use of an array of PMQs with focusing gradients of 160 and 300 T/m, we obtain an efficient collimation of the proton beam into the ES.
To conclude, we performed start-to-end particle tracking simulations of the optimized beam line, achieving a final energy spread of $\leq$20 % with an overall efficiency of $\geq$1 % in terms of particles transmitted from the laser-plasma source.
Our scientific results concerning the beam transport and beam shaping of TNSA proton beams pave the way to innovative applications, where quasi-monoenergetic beams with a high bunch charge are required, such as in the domain of material science and IBA.

Résumé

L'étude des faisceaux de particules générés par laser représente un domaine important dans les recherches scientifiques actuelles, tant du point de vue théorique que du point de vue expérimental.
Contrairement aux accélérateurs de particules conventionnels utilisant des sources radiofréquences (RF), les sources de particules générées par laser permettent l'accélération des particules (à la fois des électrons et des ions) dans des champs électriques extrêmes par l'interaction d'impulsions laser ultra-intenses (>$10^{18}\ W \cdot cm^{-2}$*) avec la matière. Les systèmes laser de classe TW, ou encore les nouveaux systèmes de classe de puissance PW, peuvent produire un plasma dans lesquels des champs électriques très élevés sont générés, permettant d'accélérer les particules sur de très courtes distances. Le champ d'accélération atteint TV/m sur quelques µm dans le cas de l'accélération des protons et jusqu'à des dizaines de GV/m sur des centaines d'µm dans le cas de l'accélération des électrons. Cela permet de surmonter les limites des schémas d'accélération conventionnels basés sur des champs RF, qui se limitent aux gradients d'accélération dans la gamme de MV/m (jusqu'à* $\sim$*100 MV/m pour la technologie de pointe), en raison du phénomène de claquage.*
À l'heure actuelle, les électrons accélérés par laser atteignent des énergies maximales dans la gamme de quelques GeV, alors que pour les protons, des faisceaux d'énergie de quelques dizaines de MeV sont routinièrement réalisables.

Les caractéristiques des faisceaux de particules générés par laser, en termes d'énergie, de charge par pulse, de durée du pulse et de laminarité, permettent de considérer ces sources comme une alternative potentielle aux sources de particules conventionnelles. Des applications telles que les lasers à électrons libres (Free Electron Lasers, FEL) pour le cas des électrons ou l'analyse par faisceau ionique (Ion Beam Analysis, IBA) pour le cas des protons, sont facilement exploitables avec les énergies de faisceaux que l'on peut atteindre aujourd'hui. Cependant, certains paramètres de ces faisceaux de particules tels que le grand étalement en énergie (quelques pour cent pour les électrons et jusqu'à 100 % pour les protons) et la forte divergence à la source (quelques mrad pour les électrons et quelques fractions de radian pour les protons) représentent un obstacle de taille afin d'obtenir des faisceaux fiables et contrôlables pouvant être mis en œuvre dans ces applications. Pour ces raisons, le transport, la confection et la manipulation du paquet de particules générées par laser sont difficiles, mais nécessaires.

L'objectif de ce travail est d'étudier la mise en place de dispositifs d'accélération conventionnels pour les lignes de faisceaux de particules générés laser. Les dispositifs de mise au point tels que les solénoïdes et les quadripôles et d'autres composants tels que les cavités d'accélération RF ou les systèmes de sélection d'énergie du faisceau permettent de transporter et de manipuler le faisceau de particules de la source initiale à la station expérimentale. Ils sont couramment utilisés sur des installations conventionnelles et peuvent être adaptés ainsi qu'optimisés aux paramètres des sources de particules par accélération laser-plasma, ce qui permet d'améliorer les performances des lignes de faisceaux générés par laser. L'étude de ces lignes des faisceaux peut donner lieu à de nouvelles techniques de mise en forme de faisceau, ouvrant ainsi la voie aux applications innovantes.

Pour l'analyse de ces lignes à faisceau laser, nous avons adopté la même méthodologie utilisée pour les accélérateurs conventionnels. Nous avons implémenté de codes numériques pour l'analyse des problèmes de dynamique du faisceau, visant à optimiser les composantes des lignes de faisceau par laser. En utilisant différents outils de simulation, nous avons mis en place un processus d'itération qui permet d'améliorer la performance des lignes de faisceau en optimisant récursivement les paramètres du faisceau de particules et les caractéristiques des éléments de la ligne du faisceau.
Nous abordons à la fois les lignes de faisceaux d'électrons et de protons, en étudiant les aspects suivants: pour les lignes de faisceaux d'électrons, nous déterminons les paramètres optimaux qu'une source d'électrons laser-plasma doit atteindre afin de permettre le transport du faisceau, tout en maintenant les caractéristiques initiales du paquet d'électrons. Cela permet ultimement d'appliquer ce faisceau pour le laser à électrons libres (FEL). Nous considérons l'émittance normalisée RMS et la dimension transversale du faisceau comme des indicateurs-clés de performance pour ces applications.
En ce qui concerne les faisceaux de protons accélérés par laser, nous proposons une configuration de ligne de faisceau, capable de réduire l'étalement de l'énergie du spectre à quelques dizaines de pour cent, tout en conservant un flux de particules raisonnablement élevé. Nous visons à obtenir des paramètres de faisceau finaux qui permettent d'implémenter des applications d'analyse par faisceau ionique (IBA).

La première section de la thèse est consacrée à l'analyse des lignes de faisceau d'électrons générés par laser. Nous proposons l'utilisation de dispositifs magnétiques utilisés dans des accélérateurs conventionnels (tels que les quadripôles et les solénoïdes) comme une solution facile à mettre en œuvre lorsque le faisceau accéléré par laser-plasma doit être transporté et optimisé.
La mise en œuvre des dispositifs de la ligne de faisceau conventionnelle a été étudiée avec une approche paramétrique, en utilisant les paramètres optiques de particules et des codes de suivi des particules qui analysent le transport et la mise en forme géométrique du faisceau d'électrons. Nous nous concentrons sur les faisceaux d'électrons à haute énergie dans la gamme GeV (8 GeV, théoriquement prévu par les simulations), tel que produit sur les systèmes laser de classe petawatt (PW) ainsi sur les faisceaux d'électrons à énergie plus basse dans les centaines de MeV (350 MeV), tel qu'ils sont produits de nos jours à partir des systèmes laser à plusieurs centaines de TW disponibles sur le marché. Pour les deux scénarios, notre étude permet de comprendre quels sont les paramètres cruciaux qui permettent aux accélérateurs par laser-plasma de concurrencer les appareils conventionnels et de permettre un transport de faisceau adéquat.
Nous analysons différentes configurations de lignes de faisceau, d'un simple triplet quadripolaire à des structures en symétriques (et même achromatiques) plus complexes, en testant leur efficacité de transport de faisceau en termes d'émittance RMS normalisée finale et de dimension transversale du faisceau. En mettant en œuvre des éléments de focalisation qui fournissent un gradient de focalisation magnétique dans la gamme de centaines de T/m, nous visons à compenser la divergence intrinsèque du faisceau d'électrons, qui se situe dans la gamme de plusieurs mrad. En outre, nous comparons l'émittance du faisceau final des électrons à accélération par laser à ce que l'on peut obtenir avec les accélérateurs classiques utilisés pour diriger les sources FEL.

Dans le cas des électrons accélérés à 350 MeV, nous cherchons à obtenir des valeurs compétitives pour une ligne de transport basée sur un réseau triplet quadripolaire. Nous identifions les exigences à la source laser-plasma (en termes de d'étalement spectral de l'énergie et de divergence transversale) que le faisceau d'électrons doit répondre pour concurrencer les sources conventionnelles FEL. Les calculs numériques que nous rapportons montrent que les points de travail appropriés nécessitent une combinaison de compromis entre une divergence de faisceau faible et un étalement d'énergie étroit: le faisceau d'électrons accéléré par laser doit avoir une divergence de ≤1 mrad et un étalement spectral d'énergie de
*≤1 % afin d'être transporté et de maintenir une valeur d'émittance RMS normalisée raisonnable de ∼1 mm*mrad, c'est-à-dire le paramètre de travail typique des accélérateurs conventionnels effectuant appliqués au FEL.*

La deuxième partie de ce travail porte sur les lignes de faisceaux de protons générés par laser. La possibilité de combiner un dispositif de sélection d'énergie (ES) pour abaisser l'étalement en énergie des particules, avec un stade de focalisation qui capture et transporte le faisceau à partir de la source laser-plasma, a été étudié. Compte tenu des paramètres requis par les applications IBA, nous visons à obtenir un étalement énergétique final de quelques dizaines de pourcents ainsi qu'une charge élevée du paquet de protons (dans la gamme du nC).
Pour le faisceau de protons initial (c'est-à-dire à la source), nous avons pris comme référence les paramètres typiques réalisables avec le mécanisme d'accélération le plus consolidé, le mécanisme Target-Normal Sheath Acceleration (TNSA). Ce mécanisme génère systématiquement des faisceaux de protons avec une énergie de l'ordre des dizaines de MeV, une charge de faisceau élevée (jusqu'à 10^{13} protons par pulse) et une courte durée de pulse (dans la gamme ps, à la source laser-plasma) en utilisant des systèmes laser commerciaux de classe TW, représentant une solution complémentaire aux sources conventionnelles pour plusieurs applications. Néanmoins, le spectre énergétique à large bande des protons générés par TNSA (jusqu'à 100 %) est un problème ouvert qui limite les expériences et les applications nécessitant des faisceaux de protons monochromatiques.

Notre étude est basée sur la dynamique du faisceau et les simulations de suivi des particules, dans le but d'analyser et de développer une ligne de faisceau pour les faisceaux de protons générés par laser, y compris les dispositifs de sélection d'énergie et de mise au point du faisceau: Une ligne de faisceau composée de quadripôles à aimants permanents compacts (PMQ) transmet le faisceau de protons de la source laser-plasma à une chicane magnétique fabriquée avec des aimants permanents permettant la sélection d'énergie du faisceau.
La gamme d'énergie que nous étudions va de 2 à 20 MeV, c'est-à-dire les énergies qui peuvent être obtenues avec de systèmes laser commerciaux de 250 TW et sont typiques pour de nombreuses applications comme l'IBA. Les caractéristiques techniques clés du sélecteur d'énergie ont été étudiées de manière paramétrique, afin de permettre une optimisation de l'appareil dans la gamme d'énergie d'intérêt. Une solution optimisée du sélecteur d'énergie est basée sur des dipôles d'environ 0,95 T, ayant une longueur de 10 cm et fournit un étalement spectral d'énergie final d'environ 20 %.
Comme étape suivante pour ce sélecteur d'énergie, nous adaptons la ligne de faisceau en amont du dispositif de sélection pour optimiser l'efficacité de transmission des protons. L'abaissement

de la divergence des protons est nécessaire pour permettre un processus efficace de sélection d'énergie: nous avons estimé que la divergence requise était de quelques mrad. Avec l'utilisation d'un réseau de PMQ avec des gradients de mise au point de 160 et 300 T/m, nous obtenons une collimation efficace du faisceau de protons dans le sélecteur.
Pour conclure, nous avons effectué des simulations de suivi des particules de bout en bout de la ligne de faisceau optimisée, obtenant un étalement énergétique final de moins de 20% avec une efficacité globale de plus de 1 % en termes de particules transmises par la source laser-plasma. Nos résultats concernant le transport du faisceau et la mise en forme des faisceaux de protons TNSA ouvrent la voie à des applications innovantes, où des faisceaux quasi-monoénergétiques à forte charge sont nécessaires, comme dans le domaine de la science des matériaux et de l'IBA.

1. Introduction: scientific context and objective of the thesis

The acceleration and, more in general, the physics of elementary particles is a continuing challenge that has been interesting scientist and engineers since the end of the 19th century.
Ever since the fundamental particles electron, proton and neutron were discovered, at the beginning of the last century, accelerated particles are of high importance for studies of fundamental physics and have a huge number of applications in the most various fields of our daily life.
Applications of accelerated particles and the machines that allow producing them, i.e. particle accelerators, can be found in areas such as physics, medicine, biology, pharmacy, environment, material science and even cultural heritage.
Since the end of the 1920s, particle acceleration is achieved with conventional accelerator facilities that use static electric fields or radio frequency (RF) electromagnetic fields to increase the energy of the particles up to the GeV range (even TeV in the case of the LHC synchrotron at CERN).

1.1 Conventional accelerators: brief history and state of the art

In the 20s the first accelerating machines were designed using DC (direct current) electric fields, i.e. non-time varying electric fields, such as in the case of the Cockroft-Walton accelerator (see Fig. 1) or the Van der Graaff generator [1] [2]. In 1932 Cockroft and Walton used a DC generator to accelerate protons in a vacuum tube up to an energy of $\sim$800 keV, at the Cavendish Laboratory in Cambridge. The limit of these DC machines based on static fields, however, was given by the breakdown limit of the electric field of a few MV/m.
As an alternative, Wideroe developed in 1928 the concept of the first AC (alternate current) - or RF - accelerator that used time-varying electric fields to accelerate particles [3]. The principles of Wideroe's findings can be applied to charged particles in general and are considered as the grounding ideas of modern RF accelerators. His work has been taken over by Ernest Lawrence who invented the cyclotron (Nobel prize in physics, 1939) [4]. At the Berkeley National Laboratory, a cyclotron has been built in the 40s, able to accelerate protons up to an energy of 730 MeV.
Since then, proton accelerators have gained an increasing interest in our society and engineers make strong efforts to satisfy more and more demanding requirements for improving and constructing them. The development of RF-technology based accelerating machines, for both electrons and ions, has led to various types of accelerators such as cyclotrons, linear accelerators, circular accelerators etc.
Modern accelerators are used for research and industrial purposes and allow obtaining particle beams at high energies. However, even with the use of RF fields, the accelerating gradient of conventional accelerators is limited by the breakdown in vacuum of the electromagnetic field: conventional accelerating devices, i.e. electromagnetic resonant cavities, only can achieve field gradients in the range of tens MV/m (up to $\sim$100 MV/m for the state-of-the-art prototypes). Hence, conventional facilities require extremely long accelerating distances for achieving high

beam energies. Accelerators for both, basic research purposes (e.g. CERN in Switzerland or SLAC in the USA) and industrial purposes (e.g. proton-based cancer treatment facilities or synchrotron-light sources such as ESRF in France) require large-scale facilities with a cost that can reach billions of dollars.

As an example, at the SLAC laboratory, in California, electron beams are accelerated up to an energy of 30 GeV by the longest existing linear accelerator (about 3 km length) and are used for driving a coherent light source (LCLS). The Large Hadron Collider (LHC) [5], a gigantic synchrotron at CERN, is located inside a circular underground tunnel of 27 km circumference (see Fig. 2) and is capable of accelerating protons up to a central mass energy of 14 TeV (i.e. colliding 2 protons at 7 TeV).

Fig. 1 – A Cockroft-Walton generator using a static electric field in the order of magnitude of a few MV/m, to accelerate charged particles.

Fig. 3 reports the Livingston chart, i.e. a graph that represents the tendency of energy increase in particle accelerators (both electrons and protons). From the slope of the dotted line, it was estimated that the top energy should be increasing by an order of magnitude about every 7-10 years. The fast growth rate that has been achieved in the past decades (until the 90s, as can be seen in Fig. 3), has been accomplished by the introduction of new accelerator technologies at frequent intervals. However, the colored markers, indicating the energy range of the LHC accelerator and its upcoming upgrade HE-LHC (considered as the most advanced particle accelerator in terms of beam energy), indicate a much lower slope. The intrinsic limits of RF-based technology in terms of maximum achievable energy are reaching a saturation point.

Scientist and engineers from the accelerator community are therefore constantly looking for alternative sources of energetic particles that could be more compact and of reduced cost.

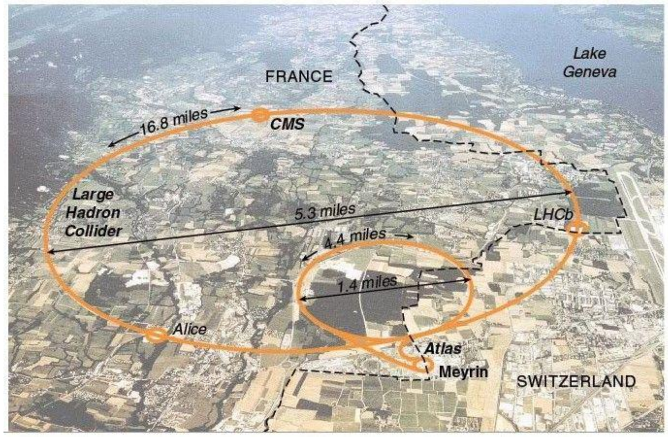

Fig. 2 – Map of the CERN accelerator facility. The outer ring indicates the circumference of the LHC tunnel.

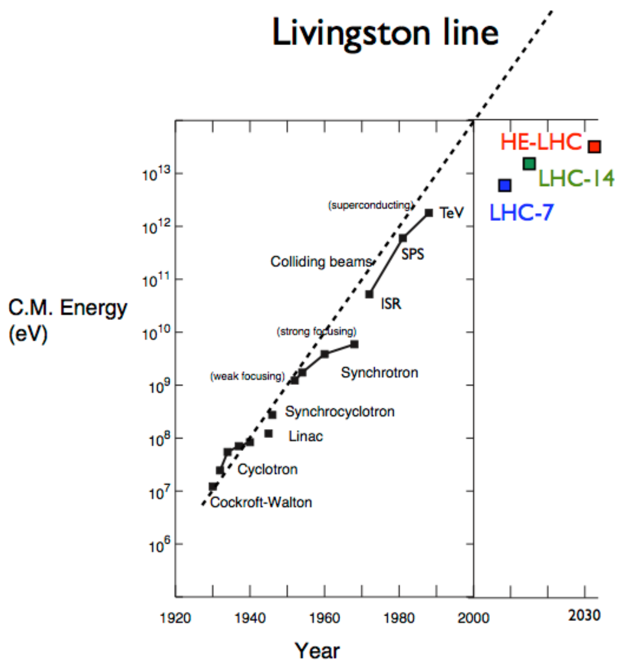

Fig. 3 – The Livingston chart shows the trend of modern accelerating technologies, yielding more and more energetic particle beams. The colored sports indicate the energy of LHC (and its future upgrades), as state-of-the-art particle collider.

1.2 Laser- accelerators: brief history and state of the art

One of the most important turning points in the evolution of laser technology was the invention of the Chirped Pulse Amplification (CPA) by Strickland and Mourou, in 1985 [6]. Compared to the previous systems, lasers implementing the CPA technology allowed achieving an improvement in terms of peak power and temporal compression of the laser pulse. In the first decade of this century, laser systems have been built achieving pulse energies in the range of multiple Joules within a ps duration (even down to tens of fs), i.e. with a power in the hundreds of TW range. The on-target intensity that is achievable with these systems, by focusing the laser light down to a spot size of a few tens μm^2 , is up to $10^{20}\ W \cdot cm^{-2}$.
Novel, upcoming laser systems combine a power in the multi PW range with a pulse duration of a few tens fs, allowing an intensity of the focused pulse of $> 10^{21}\ W \cdot cm^{-2}$.

The advent of high-power lasers has opened up possibilities of laser-based particle acceleration. This novel type of accelerators represent an alternative to RF technology based accelerators: differently from conventional RF accelerators, laser-driven particle sources accelerate particles (both electrons and ions) with electric fields that are generated by the interaction of intense laser pulses and matter in a plasma state. The use of TW-power class laser systems, or even novel PW-power class systems, leads to a plasma that can withstand electric fields up to TV/m, which enables accelerating particles within very short distances.
Henceforth, several laser facilities have been built in recent years with the main purpose of performing laser-plasma acceleration experiments, and even more are being built or commissioned in present days. Commercial, operating TW-class systems, for instance, are the 500 TW laser system at ALLS (INRS, Canada) [7], Draco at FZD (Dresden, Germany) [8] or the 250 TW laser FLAME at INFN-LNF (Frascati, Italy) [9]. PW-class facilities being operational are e.g. at the BELLA laser facility at BNL (Berkeley, USA) and others are being developed, such as the laser facilities of the Extreme Light Infrastructure (ELI) in Europe [10] [11].

1.2.1 Evolution of laser driven electron acceleration

The acceleration of electrons through laser-driven plasma wakefields has been studied since the 70s/80s and the pioneer theoretical work proposing the use of a plasma to accelerate electron bunches has been published by Tajima and Dawson in 1979 [12]. In this work, the authors presented schemes for accelerating electrons using both a laser beat wave and a laser wakefield. In the 90s, several experiments have been performed, following the idea proposed by Tajima and Dawson, achieving the acceleration of electron bunches, externally injected into the plasma, up to tens of MeV. The experiment held at LULI (France), using a Nd:glass laser with a wavelength of ~1 μm, demonstrated the acceleration of a 3 MeV electron beam up to an energy of 3.7 MeV with an accelerating gradient of 0.6 GV/m [13].
Moreover, in 1994 an accelerating electric field in the range of hundreds of GV/m has been measured: the amplitude of the plasma wave was high enough to allow an electron bunch to be trapped and accelerated in the plasma, along the direction of propagation of the laser pulse [14].

In the early 2000s, 35 fs long pulses from a 10 TW power laser-system have been used at the LOA laboratories to accelerate electrons from an exploded foil plasma, obtaining electron beams with a maximum energy of ∼35 MeV [15]. These results led to the initiation of the PLASMONX project, at the LNF laboratories (Frascati, Italy), with the aim of accelerating electron bunches injected externally in the plasma and implementing X- and γ-Ray sources via Thompson scattering [16] [17].
In these experiments, the energetic distribution of the obtained electron beam has a Maxwellian-like shape, i.e. a wide energy spread caused by the random injection process in the relativistic plasma waves. The profile of the plasma wakefield driven by the laser pulse has been observed with the use of a chirped laser probe pulse, as reported in Ref. [18] and shown in Fig. 4.

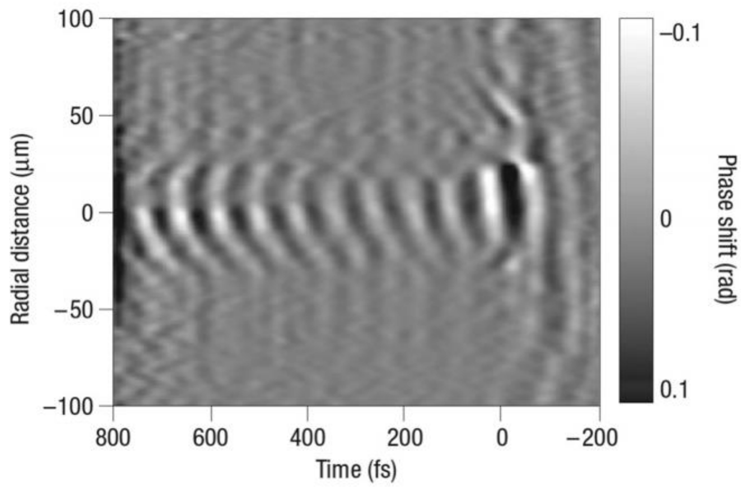

Fig. 4 – Relativistic wakefield, driven by a laser pulse propagating to the right. Reprinted from Ref. [18]

In 2004, a breakthrough has been achieved by reaching electron energies in the range of 80-150 MeV [19] [20] [21]. Moreover, in 2006, the GeV energy limit has been reached with quasi-monoenergetic bunches [22]. The injection of the electron bunch has been produced within a volume smaller than the plasma wavelength (typically 10-100 µm), leading to an improved beam quality and a temporal duration of the bunch in the range of a few fs, making laser-based electron accelerator a complementary solution to conventional RF-technology based machines.
The currently highest maximum energy has been achieved by Leemans et al. in 2014, with the BELLA PW-power class laser at the LBNL laboratories (USA). An electron bunch of ∼ 20 pC has been accelerated up to an energy of 4.2 GeV with an energy spread of a few percent [23].

1.2.2 Evolution of laser driven proton acceleration

First evidence of proton production by laser-target interaction was observed at the Los Alamos National Laboratory (USA) in experiments between 1978-1983 [24], when targets were illuminated by a 10.6 μm CO_2 laser with pulse length of <1 ns and peak intensity of $10^{17} - 10^{18}\ W \cdot cm^{-2}$ per μm^2.

The characteristics of the proton beam were not exceptionally interesting: maximum proton energy of ~0.56 MeV, electron temperature ~11.7 keV with the ion beam emitted in 2π steradians. However, the maximum proton energy was found to be proportional to the temperature of the supra-thermal electrons produced during the laser-plasma interaction [25].

Later evidence of laser-accelerated protons beams with significantly improved beam characteristics was reported by experiments in the late 90s using the Lawrence Livermore National Laboratory (USA) NOVA Petawatt (PW) laser using picosecond, relativistic laser-plasma interactions. Targets were irradiated with an intensity of $= 3 \times 10^{20}\ W \cdot cm^{-2}$.

The use of a magnetic spectrometer and radio-chromic films (see Fig. 5) showed energetic protons with a Bolzmann-like energy spectrum and a sharp cut-off energy at ~58 MeV [26].

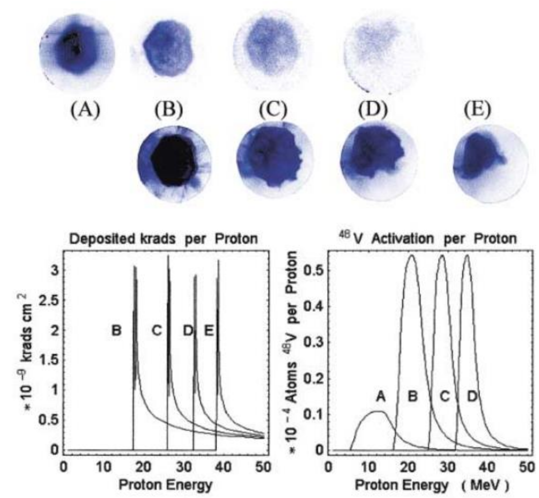

Fig. 5 – Proton beam detected by Snavely et al. using radio-chromic films stacks. The bottom plots show Monte Carlo simulations of the detectors' response. Reprinted from Ref. [26].

Further evidence of collimated proton beams with multi-MeV energies, obtained when an ultra-intense laser pulse hits a solid target, were found in various other experiments. Proton bunches having energies of up to 18 MeV with 10^{12} protons at energies greater than 2 MeV, were obtained from a 125 μm thick aluminum target. These results were obtained with the VULCAN laser at Rutherford Appleton Laboratory (USA), at an intensity of $5 \times 10^{19}\ W \cdot cm^{-2}$. [27] Maksimchuk et al. used a 10 TW laser with lower intensities of $3 \times 10^{18}\ W \cdot cm^{-2}$ obtaining collimated proton beams of about 1.5 MeV with aluminum metal targets of 3-25 μm. [28] Murakami et al. did experiments on the 50 TW GEKKO MII laser, using peak intensities of $5 \times 10^{18}\ W \cdot cm^{-2}$ focused on a 5-10 μm aluminum target, obtaining maximum proton energies of about 8-10 MeV. [29]

Further experiments have been performed in the last two decades, investigating the scaling laws that relate the maximum energy and the charge of the proton beam to the laser pulse parameters [30] [31] [32].
For state-of-the-art commercial laser systems with a power in the range of hundreds of TW (up to a few PW), the dominating acceleration mechanism is the Target Normal Sheath Acceleration (TNSA) [33]. It is widely recognized as the best known mechanism, allowing to obtain proton beams with energies of tens of MeV, routinely [8] [34] [7]. Nevertheless, novel acceleration mechanisms are being studied at present times, leading to even higher energies and better beam quality.
As an example, the Collision-less Shock Acceleration (CSA) uses the long pre-pulse of the laser (typical duration of ns and intensity usually 6 orders of magnitude lower than the main pulse) to generate a decompression of the irradiated target, which leads to a shock-wave of ions inside the target when the main pulse arrives. The resulting proton beam has energies exceeding 40 MeV and is better collimated, if compared to the TNSA mechanism [35]. Promising experimental results have been obtained using 60 J pulses from a CO_2 laser [36] and ~300 J pulses from a Nd:glass laser [37].
In terms of maximum energy, the Break Out Afterburner mechanism showed promising results, yielding energies in excess of 65 MeV [38].
Experiments have been performed, where specially engineered targets have been used, with the aim of improving the energy and quality of the laser-accelerated proton beam. In 2013 Fourmaux et al. investigated the efficiency of the acceleration process with respect to the thickness of nm-scale solid targets [7]. Moreover, Diamond-like-carbon, nm-thick targets have been used, in order to exploit the Radiation Pressure Acceleration (RPA). The experimental results show a maximum energy of 20 MeV (obtained with an on-target intensity of $\sim 10^{20}\ W \cdot cm^{-2}$) with a spectrum that shows pronounced peaks at certain energies [39].
Flat-top cone targets have been used in combination with a TW-power class laser system, in order to improve the efficiency of the laser-acceleration of protons, yielding maximum energies in the multi-tens of MeV range [40] [41].

The interesting features of proton beams generated by short, ultra-intense lasers represent a challenging new research topic of worldwide interest for numerous fascinating potential applications.

1.3 Objectives of the thesis: study of laser-driven beam lines

The main objective of the work reported in this thesis, is to study the implementation of laser-driven particle beam lines.
Even if laser-plasma generated particle beams, both electrons and protons, represent a breakthrough in accelerator science, several of their parameters still need to be improved. For instance, the large energy spread (a few percent for electrons and up to 100 % for protons) and strong divergence at the source (a few mrad for electrons and fractions of radiant for protons) [23] [42] [43] [44] represent an obstacle for numerous applications. The applications where laser-

driven particle beam do not meet the required parameters obtained with conventional machines, are, for example, Free Electron Laser (FEL) sources in the case of electrons [45] [46]. Laser-generated protons still lack of beam quality for being implemented in several material science applications, medical applications and novel, ultra-short neutron sources [47] [48] [49].

On conventional accelerators, the final beam parameters that are required for the given application, are commonly achieved with devices such as RF accelerating cavities, focusing devices such as solenoids and quadrupoles, beam energy-selection systems etc., that constitute a so called "beam line" which transports and manipulates the particle beam from the initial source to the experimental end station.
Since laser-driven particle sources produce particle beams with characteristics that are different from what is obtained on conventional accelerators and are not always well suited for several applications, the tailoring and the manipulation of the particle bunch is necessary. The conventional devices mentioned before allow tailoring the parameters of the laser-driven beams that need to be improved, if their implementation is optimized for the case of laser-plasma sources. Moreover, the methodologies that are typical for conventional accelerators, which use beam quality indicators, simulation codes etc., can be applied for optimizing laser-driven beam lines [50] [51] [52] [53] [54] [55].

As represented in Fig. 6, a hybrid laser-driven beam line is a system that reckons on a particle source that is based on laser-plasma interaction. For both electrons and protons, these types of sources provide beams that need to be transported to the application and tailored in order to meet the needed requirements. The devices that are used on conventional facilities to build up a beam line can be adapted for the characteristics of a laser-plasma particle source. For example, laser-driven proton beams have a very large intrinsic divergence at the source that is uncommon for conventional accelerators. Therefore, the focusing devices of the beam line (e.g. quadrupoles) must have particularly high field gradients in order to capture the particles and keep the dimensions of the bunch under control.

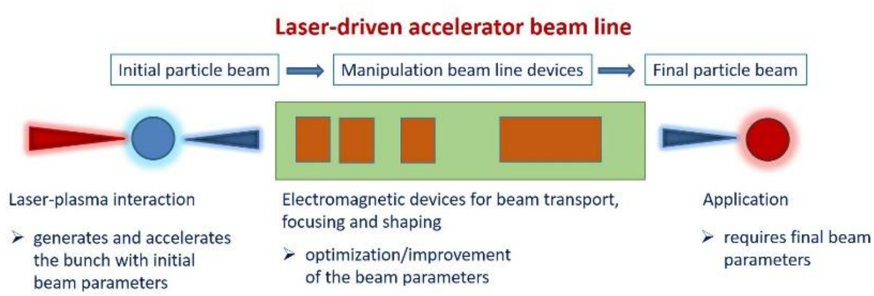

Fig. 6 – Qualitative schematic of a hybrid laser-driven particle beam line. The particle source generates and accelerates the beam via a laser-plasma interaction. Downstream, the beam is manipulated with conventional devices that shape the beam parameters, according to what is required for the applications.

The handling of laser-accelerated particles using non-conventional techniques has been studied, as well. Using a laser-triggered plasma micro-lens allowed successfully focusing and energy select a TNSA proton beam via a strong electrostatic field [56], as described in Fig. 7. Similar results have been obtained using the intense magnetic fields generated with the laser-plasma interaction of a secondary target, where a TNSA proton beam travels through and is focused [57].
These beam handling experiments have shown promising results. However, the use of such focusing devices involves additional challenges to the experimental setup (e.g. the use of a second laser pulse that needs to be synchronized or delayed with respect to the main pulse) if compared to the scenario where conventional, passive electromagnetic devices are used. Therefore, within the studies reported in this thesis, we have focused on the analysis of hybrid beam lines involving conventional elements downstream the laser-plasma source.

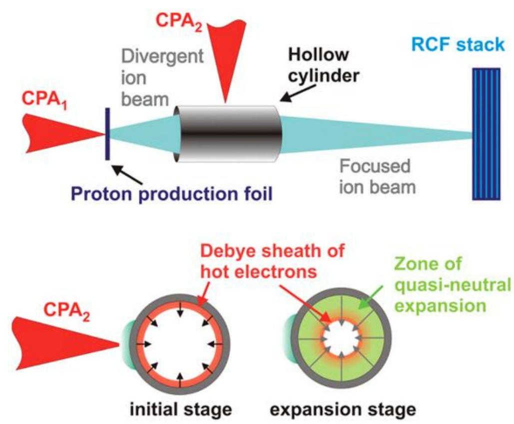

Fig. 7 – A focusing microlens for TNSA proton beams. The protons travel through a hollow cylinder that is irradiated by a secondary laser pulse (top scheme). The cylinder is ionized and a hot electron sheath generates an electrostatic field that focuses the passing protons.

The goal of my research is to obtain final beam parameters that make laser-plasma sources a viable alternative to RF-technology based accelerators for novel applications. For achieving this, I studied the typical features of the laser-plasma source, in order to improve the parameters that need to be improved using beam line devices downstream the laser-plasma interaction point.
Therefore, the research within my Ph.D. is focused on three aspects:
I) the study of the laser-plasma interaction processes that lead to the particle acceleration and the assessment of typical characteristics of laser-driven particle beams (routinely available), in terms of energy and beam dynamics parameters;
II) the study of conventional accelerator techniques applied to laser-plasma sources, with a focus on beam dynamics (transverse and longitudinal) and on devices that are used for controlling conventional beam lines;
III) the implementation of conventional accelerator devices for the transport and manipulation of laser-accelerated particle beams.
The combination of these aspects enables to study innovative solutions for improving the quality of laser-driven particle acceleration. It is possible to adapt laser-driven proton and electron beams to applications that require very specific beam parameters, which are not currently

obtained at the laser-plasma source, with the use of beam lines that manipulate the particle bunch downstream the laser-plasma interaction point. Throughout the Ph.D., both the cases of proton and electron beams have been investigated.

1.4 Hybrid beam lines for laser-accelerated particle beams: state-of-the-art

Investigating on the implementation of beam lines based on conventional devices for the optimization of laser-driven particle sources is a field of research that has gained popularity only since the last decade.
In this paragraph we give a brief insight to what has been achieved recently, concerning the study and development of hybrid beam lines.

1.4.1 Hybrid beam lines for laser-accelerated electrons

In the field of laser-accelerated electrons, the focus has been put on tackling the challenge to compete with conventional accelerators, mainly for two applications: achieving the similar performances of electron colliders, using laser-accelerated beams and replacing the conventional accelerators that drive Free Electron Lasers with plasma-wakefield electron sources.
We focus on the FEL applications, as they require less challenging parameters, compared to the case of colliders, and represent a topic (which we tackle in the analysis of Chapter 3) widely studied within the scientific community.

Studies about the possibility of designing compact electron beam lines using conventional transport elements have been performed using focusing quadrupoles. In 2007, analyzing the implementation of laser-driven electron beams for FEL applications, Grüener et al. have studied the possibility of using electron bunches with an energy of hundreds of MeV (up to a few GeV) and a short duration (tens of fs) for generating X-rays from a magnetic undulator [58]. For FEL applications, in 2009, an experimental set-up involving a focusing stage based on magnetic quadrupoles, has been proposed [59]. In this work, Fuchs et al. study a beam line where a 210 MeV, laser generated electron beam is captured with a quadrupole doublet and transported to a 30 cm long undulator, for the generation of soft X-rays.

In 2011, Weingartner et al. have reported on the use of a quadrupole array in order to obtain a point-to-point imaging of the electron beam at the source, as shown in the scheme of Fig. 8 [60]. The use of focusing quadrupole triplet for laser-driven electrons has been analyzed by Antici et al. in 2012 [55], pointing out the issue of normalized emittance growth, which has been taken over by Migliorati et al. in 2013 [61]. This effect, typical of laser-accelerated electron beams is discussed more in detail in Appendix I and is taken into account in the analysis of Chapter 3.

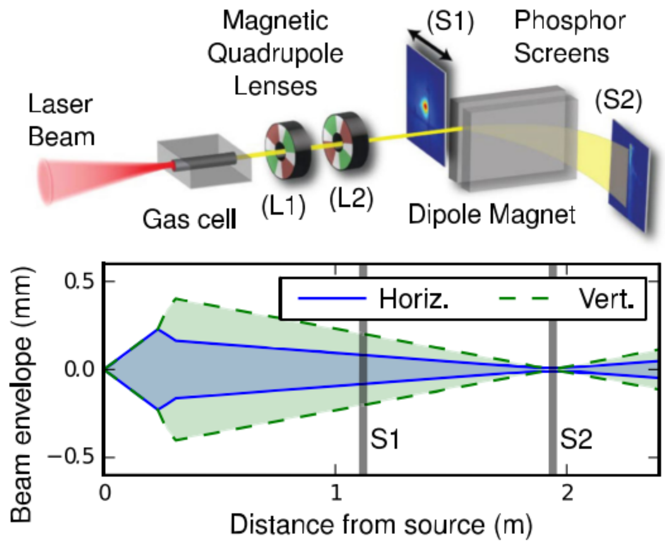

Fig. 8 – Top scheme: experimental setup used by Weingartner et al. for capturing a 200 MeV electron beam from the laser-plasma source. Bottom plot: the envelope of the electron beam, as transported by the doublet of magnetic quadrupoles (L1 and L2). Extracted from Ref. [60].

Recently, studies concerning more complex transport lines, optimized for laser-driven electron beams have been performed (including the work reported in this thesis in Chapter 3). Chancé et al. report on the implementation of an achromatic beam line, in order to overcome the issue represented by the energy spread of laser-accelerated electron bunches (typically between 5 and 10%). This beam line is optimized for a 50 MeV electron beam and is meant to be implemented in a multi-staged system, i.e. a system where the electron bunch is transported and accelerated throughout multiple laser-plasma acceleration stages [54]. M. E. Couprie et al. propose the use of a beam line involving the use of a magnetic chicane to guide a laser-accelerated electron beam into an undulator, in order to reduce the “slice energy spread” (i.e. the energy spread of a longitudinal slice/fraction of the bunch). Moreover, the design of a transport line for 180 MeV laser-plasma electrons is reported in Ref. [62].

Studies concerning hybrid beam lines have been supported by the optimization of conventional beam transport devices, according to the parameters of laser-plasma electron bunches. As an example, in 2007, Eichner et al. [63] have designed miniature quadrupole magnets, optimized for the compactness of a laser-driven electron beam line (see paragraph 1.4.3 for further details).

1.4.2 Hybrid beam lines for laser-accelerated protons

The studies of proton beam lines based on a laser-plasma source coupled with conventional elements, mostly aim to adapt the beam characteristics according to the specific application. Laser-driven proton acceleration most commonly yields beams with an extremely wide energy spectrum (100% for the TNSA, the most studied and exploited acceleration mechanism) and therefore the beam line downstream the source is usually optimized for a central energy that will be selected out of the whole beam. Furthermore, attempts have been made to increase the energy of the laser-accelerated proton beams with post-acceleration schemes, aiming to reach energies in the multi-hundred MeV range which would allow a breakthrough in medical applications (e.g. 230 MeV are required in order to perform hadron-therapy to in depth located organs).

The first experimental evidence of the feasibility of a beam line that involves RF cavities, coupled with a laser-plasma proton source, has been provided by Nakamura et al., who used a 40 kV/20 mm RF resonator to post-accelerate a proton beam with energies in the multi-hundred keV range, obtaining a final energy spread of about 7% [64].
A more complex beam line, involving the post-acceleration by a RF cavity, has been implemented by Nishiuichi et al., in 2010. The central energy of the obtained proton beam is of 1.9 MeV, obtained with a laser-plasma source driven by a 630 mJ, 45 fs long laser pulse [65].
The use of accelerating cavities for the post-acceleration of TNSA beams with higher energy, has been proposed by Antici et al. between 2008 and 2011. The implementation of accelerating cavities that are commonly used in conventional proton accelerator facilities, i.e. drift-tube-linac (DTL) cells, has been studied. The proton beam that has been considered had an initial energy of 7 MeV and numerical calculations showed how it could be accelerated up to $\sim$15 MeV with the use of 48 DTL cells, over a distance of 8 m [53] [52].

There have been also studies about the collimation (i.e. the capture and transport) of laser-generated proton beams, using conventional focusing devices such as quadrupoles and solenoids. Quadrupoles for the focusing and monochromatization of a laser-accelerated proton beam, have been used by Ter-Avetisyan et al. and Schollmeier et al., in 2008 [66] [67]. The first group managed to select and focus $\sim 10^8$ protons, with a central energy of 3.7 MeV, out of a TNSA beam generated by a TW-class laser. The latter group used permanent magnet quadrupoles, such as those of Ref. [63], to focus a 14 MeV proton beam accelerated with a PW-power class laser.

The implementation of high-power solenoids, downstream a laser-plasma proton source, has been tested by Burris-Mog et al. (2011) and Busold et al. (2013), performing experiments that involved magnetic solenoid fields in the multi-Tesla range [68] [69]. The experimental setup of Burris-Mog et al. is reported in Fig. 9.
Moreover, the combination of a solenoid and a RF cavity, is being studied by the latter group, as well [70].

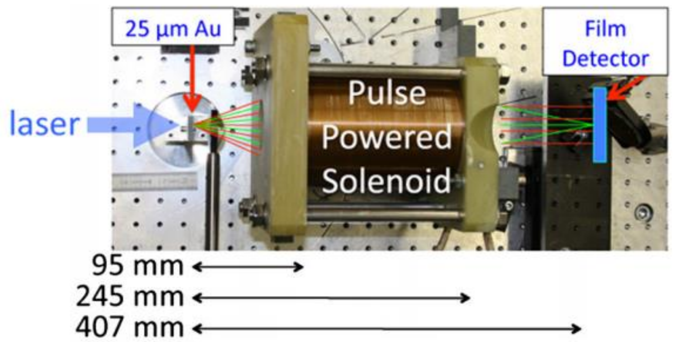

Fig. 9 – Experimental setup used by Burris-Mog et al.. The solenoid, reaching up to 16 T axial field, is placed downstream the laser-plasma interaction point and captures the TNSA protons. Extracted from Ref. [68].

In order to lower the energy spread of TNSA proton beams, magnetic energy selectors have been proposed. The experiments performed in 2014 by Chen et al. and Scuderi et al. [71] [72], implement a magnetic chicane, based on permanent magnet dipoles, that disperses the proton beam which can be spatially selected with a movable slit. This kind of scheme allows tuning easily the beam line for different energies of the proton beam and has been studied in detail in Chapter 4 of this thesis. In particular, the aim of the study reported in Chapter 4 is to combine the use of a device such as studied in Ref. [71] and [72] with an optimized focusing beam line for laser-accelerated protons, based on permanent magnet devices similar to those designed by Eichner et al. [63] for the case of an electron beam line.
Such kind of beam line represents the most novel technique for selecting a proton beam in energy, keeping the fluency of particles high. In our study, we analyze in detail the parameters that have to be optimized for improving the performance of the beam line as much as possible, in terms of obtained energy spread of the proton beam and number of available particles at the end of the beam line.

1.4.3 Compact transport and focusing quadrupoles for laser-accelerated particle beams

Some of the studies concerning the focusing of laser-generated particles, mentioned in Paragraphs 1.4.1 and 1.4.2, use high magnetic field, permanent magnet quadrupoles.
With these devices, the beam dimensions (both transversely and longitudinally) can be kept under control and/or be manipulated.
The focusing strength of these devices is high enough for dealing the high values of energy spread (up to 10% for electron beams and 100 % for proton beams) and transverse divergence (multiple mrad for the electron beams and fractions of radiant for the proton beams) of the laser-plasma beams.

In Fig. 10 we report the design of a Permanent-Magnet-Quadrupole, designed by Eichner et al., [63] that has been optimized for focusing a laser-accelerated electron beam with the aim of exploiting FEL applications.
Such a device is capable of providing magnetic gradients of up to 500 T/m, with dimensions of a few cm. The high focusing strength, achieved by using NeFeB permanent magnets, is required in order to compensate the high beam divergence that is typical of laser-generated electrons, i.e. from a few up to tens of mrad. The size of these devices allows having a transport beam line that is compact enough to keep the advantage of using a laser-based electron accelerator.
The study of this kind of components and even more complex beam focusing elements (e.g. sexupoles) in combination with laser-driven particle sources is a topic of research that has been gaining popularity in recent years. An efficient transport line for laser-accelerated particles would lead to the possibility of shaping the beam parameters accordingly to the requirements of a given application.

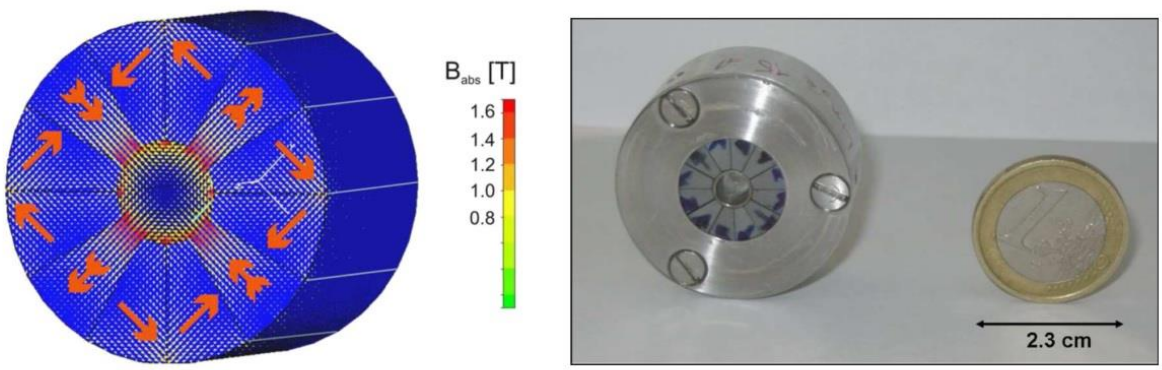

Fig. 10 – Schematic view and photograph of the 12 segment design of the PMQ developed by Eichner et al. The bore radius of the quadrupole has a radius of about 3 mm and the field strength at the tip is about 1.5 T. Extracted from Ref. [63].

The analysis that we have performed in Chapter 3 relies on the possibility to use specific devices, optimized for the characteristics of laser-accelerated electron beams.

For laser-accelerated proton beams, the focusing stage of the beam line needs to compensate the high divergence of the bunch at the source. This is necessary in order to transport the beam efficiently and select the protons within a narrow energy spread, keeping the particle flux as high as possible (e.g. applications in the domain of material science often require a bunch charge as high as 1 nC (see Paragraph 4.4.1 for further details)).
The analysis of the proton beam line’s focusing stage in Chapter 4 is based on magnetic quadrupoles with parameters similar to those obtained by Eichner et al. in Ref. [63].

1.5 Outline of the thesis' contents

We report a brief outline of the contents that we address within this work. This study concerns topics from both the physics of conventional accelerators and the laser-plasma based particle acceleration techniques of electrons and protons.

In Chapter 2, we present the methodologies that we have used for our studies. We describe the numerical tools, i.e. the software, that have been used for the simulations of the electron and proton beam lines that we have analyzed.
Furthermore, we present the iterative method that has been used for the analysis of both electron and proton beam lines.

In Chapters 3 and 4 we report the results of our studies, where the author's contribution has been major.

The analysis of electron beam lines is reported in Chapter 3. We have performed a parametric study of several beam line configurations, optimizing the transport elements of the beam line and varying the parameters of the laser-driven electron beam.
Two different scenarios have been considered: a high energy electron beam of 8 GeV, generated with the use of a PW-power class laser, and a low energy electron beam of 350 MeV, obtained with a commercial TW-power class laser.
With the goal of indicating the required beam parameters at the laser-plasma source that allow an efficient beam transport, we compare the performances of laser-driven beam lines with what is obtainable on conventional facilities.

In Chapter 4 we report on a study, based on beam dynamics and particle tracking simulations, about a beam line for laser-driven proton beams, including devices for energy selection and beam focusing. We analyze a focusing beam line that transports the proton bunch from the laser-plasma source to a magnetic energy selector.
The range of energy we investigate goes from 2 to 20 MeV, i.e. the typical energies that can be obtained for ion acceleration using a commercial 250 TW-power laser system.
The key technical features of the energy-selector have been studied in a parametric way, in order to allow an optimization of the device in the energy range of interest. Furthermore, we adapt the beam line upstream the selection device, according to the beam parameters that are necessary for allowing an efficient energy selection process.

References

[1] J. D. Cockroft and E. T. S. Walton, *Proc. R. Soc.,* vol. A136, p. 619, 1932.

[2] R. J. V. d. Graaff, *Phys. Rev.,* vol. 38, p. 1919, 1931.

[3] R. Wideroe, *Archiv fuer Elektrotechnik,* vol. 21, pp. 387-406, 1928.

[4] E. O. Lawrence and M. S. Livingston, *Phys. Rev.,* vol. 40, 1932.

[5] O. S. Bruening, C. Paul, P. Lebrun, S. Myers, R. Ostojic, J. Poole and P. Proudlock, *LHC Design Report, CERN 2004-003,* 2004.

[6] D. Strickland and G. Mourou, *Opt. Comm.,* vol. 56, p. 219, 1985.

[7] S. Fourmaux, S. Buffechoux, B. Albertazzi, D. Capelli, A. Levy, S. Gnedyuk, L. Lecherbourg, P. Lassonde, S. Payeur, P. Antici, H. Pepin, S. Marjoribanks, J. Fuchs and J. C. Kieffer, *Phys. Plasmas,* vol. 20, p. 013110, 2013.

[8] K. Zeil, S. D. Kraft, S. Bock, M. Bussmann, T. E. Cowan, T. Kluge, J. Metzkes, T. Richter, R. Sauerbrey and U. Schramm, *New J. Phys.,* vol. 12, p. 045015, 2010.

[9] G. Grittani, M. P. Anania, G. Gatti, D. Giulietti, L. A. Gizzi, M. Kando, M. Krus, L. Labate, T. Levato, P. Londrillo and F. Rossi, *Nucl. Instrum. Meth. A,* vol. 740, pp. 257-265, 2014.

[10] E. Gerstner, *Nature,* vol. 446, pp. 16-18, 2006.

[11] G. Morou and T. Tajima, *Optics and Photonics News,* vol. 22, pp. 47-51, 2011.

[12] T. Tajima and J. M. Dawson, *Phys. Rev. Lett.,* vol. 43, p. 267, 1979.

[13] F. Amiranoff, D. Bernard, B. Cros, F. Jacquet, G. Matthieussent, P. Miné, P. Mora, J. Morillo, F. Moulin, A. E. Specka and C. Stenz, *Phys. Rev. Lett.,* vol. 74, p. 5220, 1995.

[14] A. Modena, A. Dangor, Z. Najmudin, C. Clayton, K. Marsh, C. Joshi, V. Malka, C. Darrow, D. Neely and F. Walsh, *Nature,* vol. 377, p. 606, 1995.

[15] D. Giulietti, D. Galimberti, M. Giulietti, L. A. Gizzi, R. Numico, P. Tommasini, M. Borghesi, V. Malka, S. Fritzler, M. Pittman, K. T. Phuoc and A. Pukhov, *Phys. Plasmas,* vol. 9, p. 3655, 2002.

[16] D. Giulietti, A. Giulietti, L. A. Gizzi, P. Tommasini, L. Serafini, V. Petrillo, C. Vaccarezza, M. Ferrario, P. Oliva, S. Stumbo, P. Delogu, U. Bottigli, S. Bertolucci and M. Calvetti, in *Proc. SPIE 6634, International Conference on Charged and Neutral Particles Channeling Phenomena II, 66341F*, 2007.

[17] D. Giulietti, E. Breschi, M. Galimberti, A. Giulietti, L. A. Gizzi, P. Koester, L. Labate and P. Tommasini, *Int. J. Mod. Phys. A,* vol. 22, pp. 3810-3825, 2007.

[18] N. H. Matlis, S. Reed, S. S. Bulanov, V. Chvykov, G. Kalintchenko, T. Matsuoka, P. Rousseau, V. Yanovsky, A. Maksimchuk, S. Kalmykov, G. Shvets and M. Downer, *Nat. Phys.,* vol. 2, p. 749, 2006.

[19] C. G. R. Geddes, C. Toth, J. v. Tilborg, E. Esarey, C. B. Schroeder, D. Bruhwiler, C. Nieter, J. Cary and W. P. Leemans, *Nature,* no. 431, pp. 538-541, 2004.

[20] J. Faure, Y. Glinec, A. Pukhov, S. Kiselev, S. Gordienko, E. Lefebvre, J.-. P. Rousseau, F. Burgy and V. Malka, *Nature,* no. 431, pp. 737-739, 2004.

[21] S. P. D. Mangles, C. D. Hooker, Z. Najmudin, A. G. R. Thomas, J. L. Collier, A. E. Dangor, E. J. Divall, P. S. Foster, J. G. Gallacher, C. J. Hooker, D. A. Jaroszynski, A. J. Langley, W. B. Mori, P. A. Norreys, F. S. Tsung, R. Viskup, B. R. Walton and K. Krushelnick, *Nature,* no. 431, pp. 535-538, 2004.

[22] W. P. Leemans, B. Nagler, A. J. Gonsalves, C. Toth, K. Nakamura, C. G. R. Geddes, E. Esarey, C. B. Schroeder and S. M. Hooker, *Nat. Phys.,* vol. 2, pp. 696-699, 2006.

[23] W. P. Leemans, A. J. Gonsalves, H. S. Mao, K. Nakamura, C. Benedetti, C. B. Schroeder, C. Tóth, J. Daniels, D. E. Mittelberger, S. S. Bulanov, L. Vay, C. G. R. Geddes and E. Esarey, *Phys. Rev. Lett. 113,* p. 245002, 2014.

[24] F. Begay and W. Forslund, *Phys. Fluids,* vol. 25, p. 1675, 1982.

[25] S. J. Gitomer, R. D. Jones, F. Begay, A. W. Ehler, J. F. Kephart and R. Kristal, *Phys. Fluids,* vol. 29, p. 2679, 1986.

[26] R. A. Snavely, M. H. Key, S. P. Hatchett, T. E. Cowan, M. Roth, T. W. Phillips, M. A. Stoyer, E. A. Henry, T. C. Sangster, M. S. Singh, S. C. Wilks, A. MacKinnon, A. Offenberger, D. M. Pennington, K. Yasuike, A. B. Langdon, B. F. Lasinski, J. Johnson, M. D. Perry and E. M. Campbell, *Phys. Rev. Lett.,* vol. 85, p. 2945, 2000.

[27] E. L. Clark, K. Krushelnick, J. R. Davies, M. Zepf, M. Tatarakis, F. N. Beg, A. Machacek, P. A. Norreys, M. I. K. Santala, I. Watt and A. E. Dangor, *Phys. Rev. Lett.,* vol. 84, p. 670, 2000.

[28] A. Maksimchuk, S. Gu, K. Flippo, D. Umstadter and V. Y. Bychenkov, *Phys. Rev. Lett.,* vol. 84, p. 4108, 2000.

[29] Y. Murakami, Y. Kitagawa, Y. Sentoku, M. Mori, R. Kodama, K. A. Tanaka, K. Mima and T. Yamanaka, *Phys. Plasmas,* vol. 8, p. 4138, 2001.

[30] J. Fuchs, P. Antici, E. d'Humières, E. Lefebvre, M. Borghesi, E. Brambrink, C. A. Cecchetti, M. Kaluza, V. Malka, M. Manclossi, S. Meyroneinc, P. Mora, J. Schreiber, T. Toncian, H. Pépin and P. Audebert, *Nature Phys.,* vol. 2, pp. 48-54, 2006.

[31] M. Passoni, L. Bertagna and A. Zani, *New J. Phys.,* vol. 12, p. 045012, 2010.

[32] L. Robson, P. T. Simpson, R. J. Clarke, K. W. D. Ledingham, F. Lindau, O. Lundh, T. McCanny, P. Mora, D. Neely, C. -G. Wahlstroem, M. Zepf and P. McKenna, *Nature Phys.,* vol. 3, pp. 58-62, 2007.

[33] S. C. Wilks, A. B. Langdon, T. E. Cowan, M. Roth, M. Singh, S. Hatchett, M. H. Key, D. Pennington, A. MacKinnon and R. A. Snavely, *Phys. Plasmas,* vol. 8, p. 542, 2001.

[34] A. Flacco, F. Sylla, M. Veltcheva, M. Carrie, R. Nuter, E. Lefebvre, D. Batani and V. Malka, *Phys. Rev. E,* vol. 81, p. 036405, 2010.

[35] E. d'Humières, P. Antici, M. Glesser, J. Boeker, F. Cardelli, S. Chen, J. L. Feugeas, F. Filippi, M. Gauthier, A. Levy, P. Nicolai, H. Pépin, L. Romagnani, M. Scisciò, V. T. Tikhonchuk, O. Willi, J. C. Kieffer and J. Fuchs, *Plasma Phys. Control. Fusion,* vol. 55, p. 124025, 2013.

[36] D. Haberberger, S. Tochitsky, F. Fiuza, C. Gong, R. A. Fonseca, L. O. Silva, W. B. Mori and C. Joshi, *Nat. Phys.,* vol. 8, pp. 95-99, 2012.

[37] C. A. J. Palmer, J. Schreiber, S. R. Nagel, N. P. Dover, C. Bellei, F. N. Beg, S. Bott, R. J. Clarke, A. E. Dangor, S. M. Hassan, P. Hilz, D. Jung, S. Kneip, S. P. D. Mangles, K. L. Lancaster, A. Rehman, A. P. L. Robinson, C. Spindloe, J. Szerypo, M. Tatarakis, M. Yeung, M. Zepf and Z. Najmudin, *Phys. Rev. Lett.,* vol. 108, p. 225002, 2012.

[38] L. Yin, B. J. Albright, B. M. Hegelich and J. C. Fernandez, *Laser and Particle Beams,* vol. 24, pp. 291-298, 2006.

[39] A. Henig, S. Steinke, M. Schnuerer, T. Sokollik, R. Hoerlein, D. Kiefer, D. Jung, J. Schreiber, B. M. Hegelich, X. Q. Yan, J. Meyer-ter-Vehn, T. Tajima, P. V. Nickles, W. Sandner and D. Habs, *Phys. Rev. Lett.,* vol. 103, p. 045002, 2009.

[40] K. A. Flippo, E. d'Humières, S. A. Gaillard, J. Rassuchin, D. C. Gautier, M. Schollmeier, F. Nuernberg, J. L. Kline, J. Adams, B. Albright, M. Bakeman, K. Harres, R. P. Johnson, G. Korgan, S. Letzring, S. Malekos, N. R.-L. Galloudec, Y. Sentoku, T. Shimada, M. Roth, T. E. Cowan, J. C. Fernandez and B. M. Hegelich, *Phys. Plasmas,* vol. 15, p. 056709, 2008.

[41] S. A. G. T. Kluge, K. A. Flippo, M. Bussmann, B. Gall, T. Lockard, M. Geissel, D. T. Offermann, M. Schollmeier, Y. Sentoku and T. E. Cowan, *Phys. Plasmas,* vol. 18, p. 056710, 2011.

[42] F. Nuernberg, M. Schollmeier, E. Brambrink, A. Blazevic and D. C. Carroll, *Rev. Sci. Instrum.,* vol. 80, p. 033301, 2009.

[43] A. Mancic, J. Robiche, P. Antici, P. Audebert, C. Blancard, P. Combis, F. Dorchies, G. Faussurier, S. Fourmaux, M. Harmand, R. Kodama, L. Lancia, S. Mazevet, M. Nakatsutsumi, O. Peyrusse, V. Recoules, P. Renaudin, R. Shepherd and J. Fuchs, *High Energy Density Physics,* vol. 6, pp. 21-28, 2010.

[44] S. Fourmaux, K. T. Phuoc, P. Lassonde, S. Corde, G. Lebrun, V. Malka, A. Rousse and J. C. Kieffer, *Appl. Phys. Lett.,* vol. 101, p. 111106, 2012.

[45] F. Grüner, S. Becker, U. Schramm, T. Eichner, M. Fuchs, R. Weingartner and S. Reiche, *App. Phys. B: Laser and Optics,* vol. 86, pp. 431-435, 2007.

[46] A. H. Zewail, *Science,* vol. 328, pp. 187-193, 2010.

[47] M. Roth, D. Jung, K. Falk, N. Guler, O. Deppert, M. Devlin, A. Favalli, J. Fernandez, D. Gautier, M. Geissel, R. Haight, C. E. Hamilton, B. M. Hegelich, R. P. Johnson, F. Merrill, G. Schaumann, K. Schoenberg, M. Schollmeier, T. Shimada, T. Taddeucci, J. L. Tybo, F. Wagner, S. A. Wender, C. H. Wilde and G. A. Wurden, *Phys. Rev. Lett.,* vol. 110, p. 044802, 2013.

[48] H. Daido, M. Nishiuki and S. Pirozhkov, *Rep. Prog. Phys.,* vol. 75, p. 056401, 2012.

[49] C. G. Ryan, D. N. Jamieson, C. L. Churms and J. V. Pilcher, *Nucl. Instr. Methods Phys. Res. B,* vol. 104, pp. 157-165, 1995.

[50] T. Burris-Mog, K. Harres, F. Nürnberg, S. Busold, M. Bussmann, O. Deppert, G. Hoffmeister, M. Joost, M. Sobiella, A. Tauschwitz, B. Zielbauer, V. Bagnoud, T. Herrmannsdoerfer, M. Roth and T. E. Cowan, *Phys. Rev. ST Accel. Beams,* vol. 14, p. 121301, 2011.

[51] F. Nurnberg, I. Alber, K. Harres, M. Schollmeier, M. Roth, W. Barth, H. Eickhoff, I. Hofmann, A. Friedman, D. Grote and B. G. Logan, *LLNL-PROC-414726,* 2009.

[52] P. Antici, M. Migliorati, A. Mostacci, L. Picardi, L. Palumbo and C. Ronsivalle, *Phys. Plasmas,* vol. 18, p. 073103, 2011.

[53] P. Antici, M. Fazi, A. Lombardi, M. Migliorati, L. Palumbo, P. Audebert and J. Fuchs, *J. Appl. Phys.,* vol. 104, p. 124901, 2008.

[54] A. Chancé, O. Delferrière, J. Schwindling, C. Bruni, N. Delerue, A. Specka and P., *Nucl. Instrum. Methods Phys. Res. A,* vol. 740, pp. 158-164, 2014.

[55] P. Antici, A. Bacci, C. Benedetti, E. Chiadroni, M. Ferrario, A. R. Rossi, L. Lancia, M. Migliorati, A. Mostacci, L. Palumbo and L. Serafini, *J. Appl. Phys.,* vol. 112, p. 044902, 2012.

[56] T. Toncian, M. Borghesi, J. Fuchs, E. d' Humières, P. Antici, P. Audebert, E. Brambrink, C. A. Cecchetti, A. Pipahl, L. Romagnani and O. Will, *Science,* vol. 312, pp. 410-413, 2006.

[57] B. Albertazzi, e. d' Humières, L. Lancia, V. Dervieux, P. Antici, J. Boecker, J. Bonlie, J. Breil, B. Cauble, S. N. Chen, J. L. Feugeas, M. Nakatsutsumi, P. Nicolai, L. Romagnani, R. Shpeperd, Y. Sentoku, M. Swantusch, V. T. Tinkhonchuk, M. Borghesi, O. Willi, H. Pépin and J. Fuchs, *Rev. Sci. Intrum.,* vol. 86, p. 043502, 2015.

[58] F. Gruener, S. Becker, U. Schramm, T. Eichner, M. Fuchs, R. Weingartner, D. Habs, J. Meyer-Ter-Vehn, M. Geissler, M. Ferrario, L. Serafini, B. Van der Geer, H. Backe, W. Lauth and S. Reiche, *Appl. Phys. B,* vol. 86, pp. 431-435, 2007.

[59] M. Fuchs, R. Weingartner, A. Popp, Z. Major, S. Becker, J. Osterhoff, I. Cortrie, B. Zeitler, R. Hoerlein, G. D. Tsakiris, U. Schramm, T. P. Rwolands-Rees, S. M. Hooker, D. Habs, F. Krausz, S. Karsch and F. Gruener, *Nat. Phys.,* vol. 5, pp. 826-829, 2009.

[60] R. Weingartner, M. Fuchs, A. Popp, S. Raith, S. Becker, S. Chou, M. Heigoldt, K. Khrennikov, J. Wenz, T. Seggebrock, B. Zeitler, Z. Major, J. Osterhoff, F. Krausz, S. Karsch and F. Gruener, *Phys. Rev. ST - Accel. Beams,* vol. 14, p. 052801, 2011.

[61] M. Migliorati, A. Bacci, C. Benedetti, E. Chiadroni, M. Ferrario, A. Mostacci, L. Palumbo, A. R. Rossi, L. Serafini and P. Antici, *Phys. Rev. Spec. Top. - Accel. Beams,* vol. 16, p. 011302, 2013.

[62] M. E. Couprie, M. Labat, C. Evain, F. Marteau, F. Briquez, M. Khojoyan, C. Benabderrahmane, L. Chapuis, N. Hubert, C. Bourassin-Bouchet, M. El Ajjouri, F. Bouvet, Y. Dietrich, M. Valleau, G. Sharma, W. Yang, O. Marcouille, J. Veteran, P. Berteaud, T. El Ajjouri, L. Cassinari, C. Thaury, G. Lambert, I. Andryash, V. Malka, X. Davoine, M. A. Trodeux, C. Miron, D. Zerbib, K. Tavakoli, J. L. Marlats, M. Tilmont, P. Rommeluere, J. P. Duval, M. H. N'Guyen, A. Rouqier, M. Vanderbergue, C. Herbeaux, M. Sebdouai, A. Lestrade, N. Leclercq, D. Dennettiere, M. Thommasset, F. Polack, S. Bielawski, C. Szwaj and A. Loulergue, *Plasma Phys. Control. Fusion,* vol. 58, p. 034020, 2016.

[63] T. Eichner, F. Gruener, S. Becker, M. Fuchs, D. Habs, R. Weingartner, U. Schramm, H. Backe, P. Kunz and W. Lauth, *Phys. Rev. Spec. Top. - Accel. Beams,* vol. 10, p. 082401, 2007.

[64] S. Nakamura, M. Ikegami, Y. Iwashita, T. Shirai, H. Tongu, H. Souda, H. Daido, M. Mori, M. Kado, A. Sagisaka, K. Ogura, M. Nishiuchi, S. Orimo, Y. Hayashi, A. Yogo, A. S. Pirozhkov, S. V. Bulanov, T. Esirkepov, A. Nagashima, T. Kimura, T. Tajima, T. Takeuchi, A. Fukumi, Z. Li and A. Noda, *Jap. J. Appl. Phys.,* vol. 46, pp. 717-720, 2007.

[65] M. Nishiuichi, H. Sakaki, T. Hori, P. R. Bolton, K. Ogura, A. Sagisaka, A. Yogo, M. Mori, S. Orimo, A. S. Pirozhkov, I. Daito, H. Kiriyama, H. Okada, S. Kanazawa, S. Kondo, T. Shimomura, M. Tanoue, Y. Nakai, H. Sasao, D. Wakai, H. Daido, K. Kondo, H. Souda, H. Tongu, A. Noda, Y. Iseki, T. Nagafuchi, K. Maeda, K. Hanawa, T. Yoshiyuki and T. Shirai, *Phys. Rev. ST- Accel. Beams,* vol. 13, p. 071304, 2010.

[66] S. Ter-Avetisyan, M. Schnuerer, R. Polster, P. V. Nickles and W. Sandner, *Laser and Particle Beams,* vol. 26, pp. 637-642, 2008.

[67] M. Schollmeier, S. Becker, M. Geißel, K. A. Flippo, A. Blazevic, S. A. Gaillard, D. C. Gautier, F. Gruener, K. Harres, M. Kimmel, F. Nuernberg, P. Rambo, U. Schramm, J. Schreiber, J. Schuetrumpf, J. Schwarz, N. A. Tahir, B. Atherton, D. Habs, B. M. Hegelich and M. Roth, *Phys. Rev. Lett.,* vol. 101, p. 055004, 2008.

[68] T. Burris-Mog, K. Harres, F. Nuernberg, S. Busold, M. Bussmann, O. Deppert, G. Hoffmeister, M. Joost, M. Sobiella, A. Tauschwitz, B. Zielbauer, V. Bagnoud, T. Herrmannsdoerfer, M. Roth and T. E. Cowan, *Phys.Rev. ST - Accel. Beams,* vol. 14, p. 121301, 2011.

[69] S. Busold, D. Schumacher, O. Deppert, C. Brabetz, S. Frydrych, F. Kroll, M. Joost, H. Al-Omari, A. Blazevic, B. Zielbauer, I. Hofmann, V. Bagnoud, T. E. Cowan and M. Roth, *Phys. Rev. ST - Accel. Beams,* vol. 16, p. 101302, 2013.

[70] S. Busold, D. Schumacher, O. Deppert, C. Brabetz, F. Kroll, A. Blažević, V. Bagnoud and M. Roth, *Phys. Rev. ST - Accel. Beams,* vol. 17, p. 031302, 2014.

[71] S. N. Chen, M. Gauthier, D. P. Higginson, S. Dorard, F. Mangia, R. Riquier, S. Atzeni, J. R. Marques and J. Fuchs, *Rev. Sci. Instr.,* vol. 85, p. 043504, 2014.

[72] V. Scuderi, S. B. Jia, M. Carpinelli, G. A. P. Cirrone, G. Cuttone, G. Korn, T. Licciardello, M. Maggiore, D. Margarone, P. Pisciotta, F. Romano, F. Schillaci, C. Stancampiano and A. Tramontana, *Nucl. Instr. Methods Pys. Res. A,* vol. 740, pp. 87-93, 2014.

2. Methodology and tools for the analysis of conventional and laser-generated particle beams

As discussed in the introduction of this thesis, the conducted research activity has addressed the analysis of both electron and proton beam lines.
The methodology that we have used, for optimizing the beam line schemes of electrons and protons, is very similar to what is done in the case of conventional particle beams. When dealing with beam dynamics issues related to conventional accelerators, the beam line that manipulates the particle bunch parameters, is previously analyzed with particle optics and particle tracking codes. These codes calculate the envelope of the bunch (beam optics code) or the trajectory of single particles, in the case of particle tracking codes, along its path in the beam line, after the initial source. It is possible to evaluate the final beam parameters, obtained with a given lattice of a beam line, starting from a specific set of initial parameters. Customizing the typical initial parameters of laser-plasma beams, allows simulating these types of sources and investigating the performance of a beam line based on conventional elements.

We have studied the possibility to obtain particle beam parameters that are comparable to what is obtained on conventional accelerators, with the use of laser-based particle sources coupled with conventional beam line devices.
We have studied various configurations of electron beam lines (see Chapter 3) and a proton beam line (see Chapter 4), basing our calculations on initial beam parameters that are routinely achievable by laser-plasma sources. The laser-accelerated particles are manipulated by the transport devices of the beam line, leading to the final beam parameters, as represented in Fig. 1, which we report once more from Chapter 1. We have performed an extensive research concerning the optimization of the beam line devices, in order to obtain a final particle beam that can compete with the performances of a conventional accelerator.

In this chapter, we discuss the main tools that we have used for simulating the dynamics of the laser-accelerated particle beams. The physical quantities, the physical effects and the particle accelerator devices that we study, are commonly used in the field of conventional particle accelerators, but they can be adapted for the analysis of laser-accelerated particle sources.
Moreover, we briefly introduce the normalized emittance growth effect, which is typical of laser-generated electron beams and which we address more in detail with the study of Chapter 3.

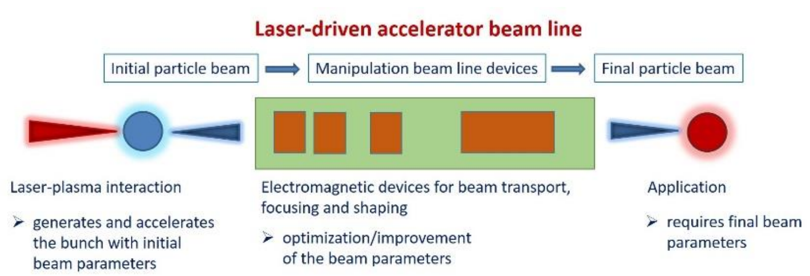

Figure 1 – Qualitative scheme of a hybrid laser-driven beam line. Differently from conventional accelerators, the particle source is based on laser-plasma interaction. The devices of the transport/manipulation line are those commonly used on conventional facilities, as well.

2.1. Numerical codes for beam dynamics calculations

We used the numerical codes TRACE3D [1] and TSTEP [2] for analyzing both electron and proton beam lines. The first is an optical code that accounts for the envelope equations of the particle bunch throughout the beam line. It is very well suited for optimizing the scheme of the beam line, under the assumption that the particle bunch has a uniform, ideal particle distribution. It allows obtaining the best parameters of the elements of the beam line, and their spacing, for a set of goal parameters that the beam has to match at the end of the beam line. The strength of the focusing devices (i.e. quadrupoles, sextupoles, solenoids etc.), the intensity of the beam bending fields (i.e. magnetic dipoles), the length of the drift regions etc. are all parameters that can be optimized with such a code.

However, TRACE3D cannot simulate realistic customized particle distributions, thus, in order to simulate laser-accelerated beams more accurately, a particle tracking code named TSTEP, has been used additionally. The initial bunch parameters that are typical of laser-plasma sources, involve effects that can be studied only if the trajectory of each particle is calculated. For example, the high value of energy spread of laser-accelerated electrons leads to significant chromatic effects within the focusing elements of the beam line, which can be correctly evaluated only if the beam has a realistic initial distribution in space and in energy. For this reason, the initial simulations run with TRACE3D have been simulated again, for both the cases of a proton and electron beam line, with TSTEP. By doing so, it is possible to test if the beam line is optimized for the initial parameters of a laser-driven particle beam, considering a realistic scenario.

The particle optics code TRACE3D has been replaced by a similar code, MAD-X [3], in the case of the calculations of Paragraphs 3.5.4 and 3.5.5. The two code rely on the same principles but MAD-X has a more sophisticated optimization algorithm, which is better suited for treating complex configurations of transport beam line.

The beam optics code TRACE3D

TRACE 3-D is a numerical code that calculates the envelopes of a bunched beam through a transport system, i.e. a transport line, made of elements defined by the user. It is possible to simulate beam transport devices such as drift spaces, quadrupoles, dipoles etc.

The particle beam can be represented by a 6-coordinate vector as $(x, x', y, y', s = z - \beta ct, \delta)$ and it is possible to analyze it's projection on the longitudinal $(s - \delta)$ or transverse $(x - x'\ , y - y')$ plane. The vector's elements represent the transverse dimensions x and y, the transverse divergence x' and y', the longitudinal dimension s and the momentum spread δ of the beam.

The most useful projection planes, for the purpose of our studies, are the transverse phase planes in which the beam can be represented with the parametric function of an ellipse, as shown in Fig. 2 . The ellipse is characterized by the Twiss parameters and emittance, as it follows. Considering the case of the beam projection on the transverse x plane, the beam can be represented by the matrix

$$\sigma_{xx} = \begin{bmatrix} x_m^2 & x_e {x'}_m \\ {x'}_e x_m & ({x'}_m)^2 \end{bmatrix},$$

or in terms of the Twiss parameters matrix

$$\sigma_{xx} = \begin{bmatrix} \beta_x \varepsilon_x & -\alpha_x x_i {x'}_m \\ -\alpha_x x_i' x_m & \gamma_x \varepsilon_x \end{bmatrix}.$$

The area occupied by the beam (i.e. the area where the $x - x'$ (or $y - y'$) couples of all the particles are) , as shown in Fig. 2, is the geometric emittance $\gamma x^2 + 2\alpha x x' + \beta x'^2 = \varepsilon$ with $\beta\gamma - \alpha^2 = 1$ and $\alpha = \frac{-\beta'}{2}$ (see Appendix I for further details about the beam emittance). The function ε is the parametric representation of an ellipse. x and x' are the beam's transverse dimension and divergence respectively. The quantities α, β and γ define the geometric shape of the beam in the transverse phase-space.
The elements of the matrix σ_{xx} on the transverse plane are shown in Fig. 2 and it is that $x_i = \sqrt{\varepsilon/\gamma}$, $x_i' = \sqrt{\varepsilon/\beta}$, $x_m = \sqrt{\beta\varepsilon}$ and $x_m' = \sqrt{\gamma\varepsilon}$. For $x = x_m$ (and for $x' = x_m'$) it is that $x_e = -\alpha\sqrt{\varepsilon/\gamma}$ (and $x_e' = -\alpha\sqrt{\varepsilon/\beta}$), following $\alpha = -\frac{x_e}{x_i} = -\frac{x_e'}{x_i'}$.

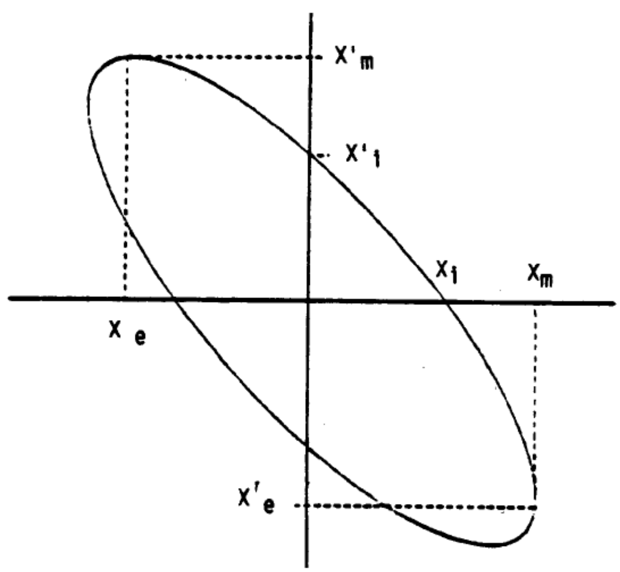

Fig. 2 – Representation of the particle beam on the transverse phase-space (here the x-x' plane is considered). The phase-space occupied by the beam is can be represented by an ellipse. Extracted from Ref. [1].

For calculating the beam parameters along the transport line, TRACE3D uses a transport matrix formalism. Given a set of beam parameters at the position s_1 of the beam line, represented by the 6 coordinates of the beam vector or the transverse plane matrix, TRACE3D calculates the transport to the position s_2 with

$$\sigma(s_2) = R \cdot \sigma(s_1) \cdot R^T .$$

The matrix R represents the transport elements between s_1 and s_2. The different elements of the beam line are represented by different matrixes.
With this formalism, the code is able to calculate the elements of sigma at any given point in the transport line, i.e. before and after any of the elements that compose the line. The relationship between the elements of sigma and the geometric parameters of the beam allows the user to obtain information about the evolution of the particle bunch along any kind of user-defined transport line.

The user can define the physical parameters of the elements that compose the beam line and analyze the evolution of the particle bunch traveling through them, in terms of beam envelope.
In the name-list of TRACE3D the user needs to define the initial Twiss parameters, α and β, the emittance ε, the energy of the beam, the longitudinal dimension of the bunch. Once the beam parameters are fixed, the elements of the transport line can be defined with their physical parameters. For example, in the case of a magnetic quadrupole, the magnetic length and the strength of the focusing (or defocusing) gradient need to be defined. The empty drift spaces with their length (defined by the user) fix the distances between the elements of the beam line.

Several element-fitting and beam-matching options are available: it is possible to optimize the physical parameters of the elements of the transport line with the aim of obtaining the desired particle beam characteristics at the end of the line, starting with a given set of initial beam parameters. For instance, as also reported in Chapter 3 and 4, the beam line can be matched for obtaining a desired final value of the Twiss parameters α and β, i.e. for obtaining specific features of the beam's transverse spot-size and divergence. The user can choose which parameters of the transport line's elements are variable and can be optimized by the code (e.g. the code optimizes the spacing between the quadrupoles of triplet lattice structure or their focusing strength).

The final beam parameters and the optimized beam line can be visualized with an interface, as shown in Fig. 3. In the top plots, the transverse phase space of the initial and final beam with the values of α and β; in the bottom scheme, the structure of the beam line with all the elements and the envelope of the particle beam as a function of the distance from the source is pictured. At the center, the numerical values of the physical parameters of the beam line are reported. If a matching algorithm has been activated by the user, these data will show the optimized value for the beam line's elements.

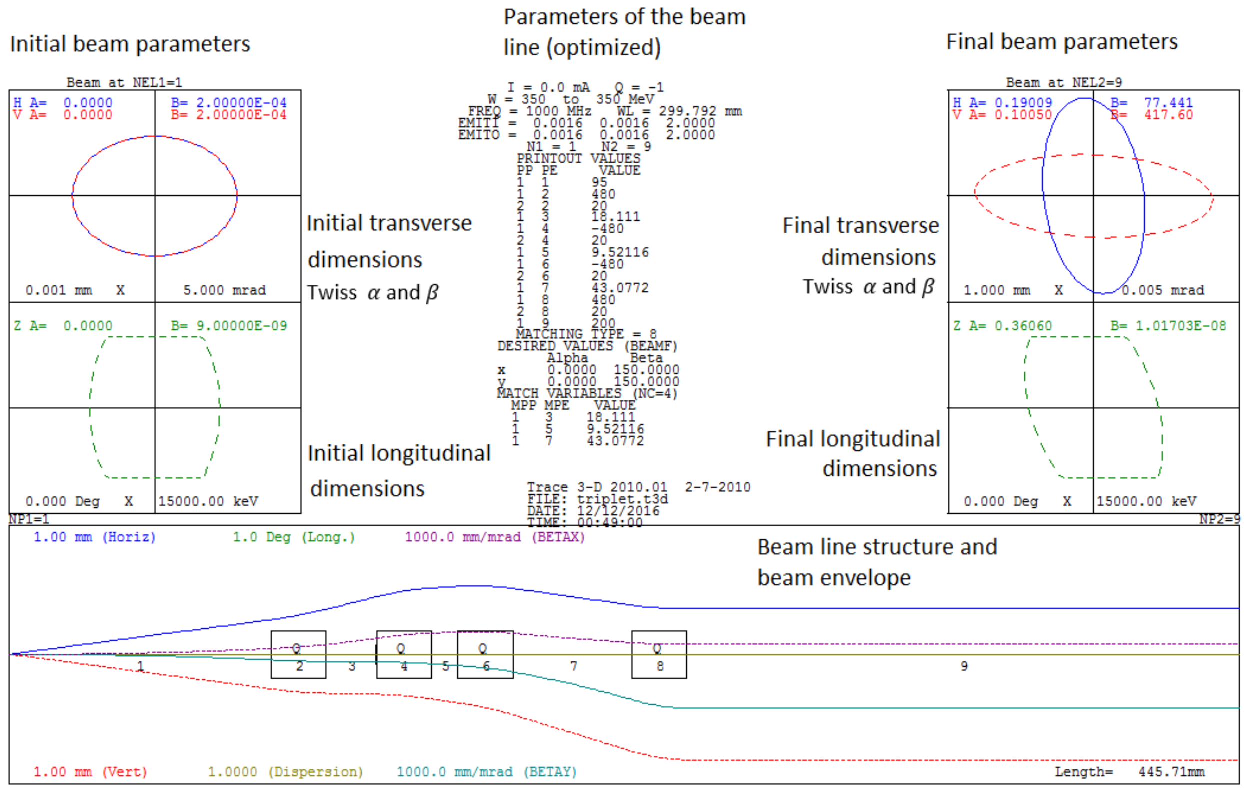

Fig. 3 – The output interface of TRACE3D. The initial and final beam parameters are shown in the top squares (blue and red phase spaces for the transverse dimensions and green phase space for the longitudinal). The code also shows optimized values for the beam line elements (numerical values in the center). The beam line configuration is shown in the bottom plot where the beam envelope, as a function of the distance from the source, is reported with the colored curves. The blue and red curves indicate the transverse dimension of the particle beam, the light-blue curve and the purple curve indicate the β-function in x and y direction.

Particle tracking code TSTEP

TSTEP is a particle tracking code that treats real particle distributions for simulating the accelerated bunch.
Each particle, similarly to TRACE3D, is characterized by a set of coordinates: spatial coordinates x, y, and z, its dimensionless momentum components $(\beta\gamma)_x$, $(\beta\gamma)_y$ and $(\beta\gamma)_z$ (being $\beta = v/c$ the velocity and γ the relativistic factor of the particles), its dimensionless energy $\beta\gamma$, and its mass and charge. In addition, we know the particle phase Φ and $\Delta\Phi$, its remaining phase step to the end of the current master-clock step. Indeed, TSTEP discretizes the longitudinal dimension of the simulation domain with a master clock having a user defined frequency f_0. The phase of each particle is calculated with reference to the phase of the master-clock Φ_0, defining the longitudinal position.

The particles, at each iteration of the beam dynamics calculation of TSTEP, are shifted by a phase advance $\Delta\Phi$ with respect to the elements of the transport line of the simulation. It is possible to

increase the frequency of the master clock in order to obtain smaller phase steps $\Delta\Phi$, leading to a finer longitudinal resolution.
At each step, the code calculates and applies the impulse resulting from all the fields in the element, including the fields from distributed elements. Using the new longitudinal velocity TSTEP finds the distance Δz that the drifting particle would travel in the phase interval $\Delta\Phi$.
At the beginning of each integration step, the code checks to see if it should apply space-charge effects, i.e. modify the trajectory of the particles according to the electric interactions with the surrounding space charge field.

The main difference with other beam optics codes, such as TRACE3D or MAD-X, is that TSTEP computes the motion of single particles along the transport line. The user can define a particle distribution and customize the phase space of the particle bunch at the beginning of the transport line. The beam envelope is not calculated ideally with a uniform particle distribution and the parameters of each particle, i.e. the information concerning position, divergence and energy, are taken into account when computing, for instance, the RMS emittance of the beam. This leads to more accurate results, compared to what is obtainable with other beam optics codes.
Moreover, the code allows retrieving the information concerning each particle, in terms of spatial position, divergence of the trajectory, energy and longitudinal phase, at any given position of the beam line. The particle bunch is represented with a table, where each line refers to one particle of the simulation, indicating all the parameters mentioned before. The output data of TSTEP are shown in Fig. 4.
In principle, it is as if TSTEP performed one TRACE3D simulation for each particle of the beam.

The number of particles that are simulated by TSTEP can be chosen by the user and is limited only by the computing capabilities of the computer one is using.
The user can define the input distribution of the bunch in the name list by choosing one of the standard distribution of the TSTEP library (e.g. a Gaussian distribution): in this case, the parameters of the single particles will be randomly generated by the code, according to the chosen distribution. Otherwise, it is possible to run the simulation using a customized distribution where all the parameters of each particle are defined by the user, i.e. the distribution is computed previously with an ad-hoc routine. The latter option is a particularly powerful tool, especially when there is the need of simulating complex and non-standard particle distribution as it can be the case for TNSA proton beams (see Chapter 4).
Other parameters of the simulated beam need to be defined by the user, as well (beam energy, particle rest mass, particle charge, bunch charge etc.).
The elements of the beam line are defined in the name list after the beam parameters.
The elements are ideal, unless differently defined by the user. TSTEP allows involving complex calculations for the non-idealities of the beam line's elements. For example, it is possible to compute higher order approximations for the calculation of the dipoles' magnetic field taking fringe fields in account. Moreover, differently from TRACE3D, with TSTEP it is possible to import field profiles (electric and magnetic) from electromagnetic solvers (e.g. SUPERFISH, see paragraph 2.2), which allows an even more accurate representation of the beam line's devices.

The processing of the simulation's data can be performed with numerical tools, such as MATLAB, allowing a statistical analysis of the particle beam distribution.

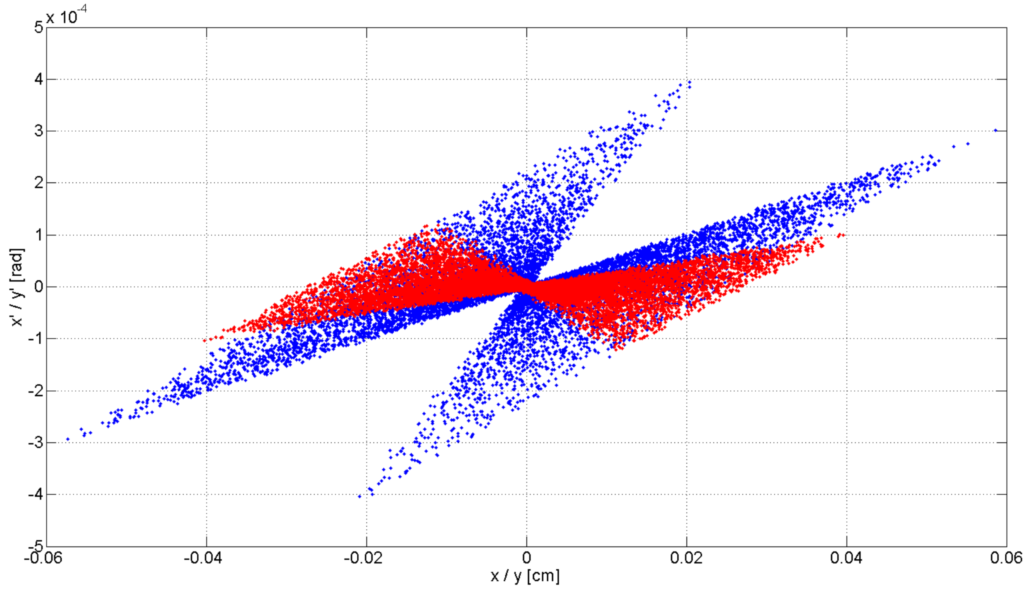

number good, elemenet #, Ref. Phase (deg.), Ref. Energy (Mev)
10001 8 0.1693179403448E+04 0.5000000150725E+03

X cord.	beta-gam X/beta-gam,	Y cord.	beta-gam Y/beta-gam,	phase-ref(phase)	Ref. energy (MeV.)	Particle #,	Particle type
0.0000000000000E+00	0.0000000000000E+00	0.0000000000000E+00	0.0000000000000E+00	0.0000000000000E+00	0.5000000150725E+03	0.1000000000000E+01	-1
-0.8760028752872E-02	0.1694421014063E-05	0.1067206986989E-01	-0.3590642614809E-05	0.9683984721732E-02	0.5000000000000E+03	0.2000000000000E+01	-1
0.2328529172119E-02	0.9925727333642E-06	-0.2707063579281E-01	0.4139494877677E-05	0.9765488523499E-02	0.5003522696431E+03	0.3000000000000E+01	-1
-0.9218840620678E-02	-0.1503165382974E-04	-0.7197075751975E-02	-0.8640464987607E-05	0.9537870380655E-02	0.5072714456748E+03	0.4000000000000E+01	-1
0.1208094369896E-01	0.5653995923325E-05	-0.8652036422937E-02	0.4877368914077E-05	0.9609543900524E-02	0.5015119042685E+03	0.5000000000000E+01	-1
0.1358848341620E-01	0.1829139782637E-04	-0.1085841911657E-01	-0.1646361936538E-05	0.9606345021894E-02	0.5022391496070E+03	0.6000000000000E+01	-1
0.2490332552811E-01	0.2616977740943E-04	-0.6106611683259E-02	-0.9869637068964E-06	0.9832521632461E-02	0.5021460506277E+03	0.7000000000000E+01	-1
0.1221367660493E-01	0.2306896807500E-04	0.2242692601912E-01	0.1090035889755E-04	0.9612011752097E-02	0.5072666147034E+03	0.8000000000000E+01	-1
-0.1376420110197E-01	0.3264763238212E-04	-0.4601776372788E-02	0.1018402549256E-04	0.9733530339417E-02	0.4901772411022E+03	0.9000000000000E+01	-1
0.1724094149050E-01	0.4111552242166E-04	-0.8691006187219E-02	-0.8514801385846E-05	0.9547073417252E-02	0.5101936888777E+03	0.1000000000000E+02	-1
-0.1880312234624E-01	-0.2542435763717E-05	-0.1808329319442E-01	0.5359171446130E-05	0.9776429694966E-02	0.4985582166399E+03	0.1100000000000E+02	-1
0.9660056692218E-03	-0.8685186256236E-05	-0.1653649778343E-01	0.1316377846451E-04	0.9538977374859E-02	0.4920439442183E+03	0.1200000000000E+02	-1
-0.1404018695411E-01	-0.3503568341929E-04	0.1772170182666E-01	0.1377609778911E-04	0.9521711763227E-02	0.5110807745946E+03	0.1300000000000E+02	-1
0.4033312210379E-02	0.1326674288491E-04	0.7520578678470E-02	0.2175037541636E-05	0.9412078657761E-02	0.5072706259976E+03	0.1400000000000E+02	-1
0.4834086462921E-02	0.2780299676248E-05	-0.8342829207127E-03	-0.6847646239268E-05	0.9419629370541E-02	0.5022602332622E+03	0.1500000000000E+02	-1
0.1192362814096E-02	0.1744366781524E-05	-0.1526476759699E-02	0.7619095105179E-05	0.9409740248884E-02	0.4992510130993E+03	0.1600000000000E+02	-1

Fig. 4 – TSTEP output data, as represented with MATLAB. The top plot shows the transverse phase space of a particle beam, calculated with TSTEP for both x-x' and y-y' planes (blue and red, respectively). The columns below show the parameters of each particle simulated by the particle tracking code.

2.2. Optimization of particle beam lines (electrons and protons): iterative method

The numerical codes presented in the previous paragraph, allow implementing an iterative method for optimizing the physical parameters of the devices of a particle beam line. Such a methodology can be applied to both the cases of electron and proton beam line.

With TRACE3D, as already mentioned, it is possible to simulate an ideal particle bunch, traveling through a transport beam line. Even if the code calculates the beam Twiss parameters only for the envelope of the particle beam, i.e. it is not possible to define a realistic particle distribution (e.g. a Gaussian distribution), it is useful in order to obtain approximately optimized values for the beam line devices' parameters.

The particle tracking code TSTEP, on the contrary, allows customizing the input particle beam distribution, which enables to have a more realistic feedback for the beam line's behavior. Moreover, it is possible to retrieve information about the beam characteristics that are linked to the particle distribution and therefore require the tracking of the single particles along the beam line, e.g. the normalized emittance (important for the study of the electron beam line, Chapter 3) or the beam dispersion (important for the proton beam line, Chapter 4). Nevertheless, TSTEP is not suited for optimizing the physical parameters of the beam line's devices, if no approximated optimization has been done, since the code does not provide the user with matching or optimization algorithms.
For these reasons, the combined use of both beam optics code and particle tracking code is necessary in order to optimize the performance of a particle beam line and have the most possible accurate response concerning the beam parameters.
For the studies of both the electron and proton beam line, we have used an iterative method that involves both codes (and an electromagnetic field solver, called PANDIRA (a tool from the SUPERFISH package [4]), whenever necessary) for the analysis of the beam line, which is shown in Fig. 5.

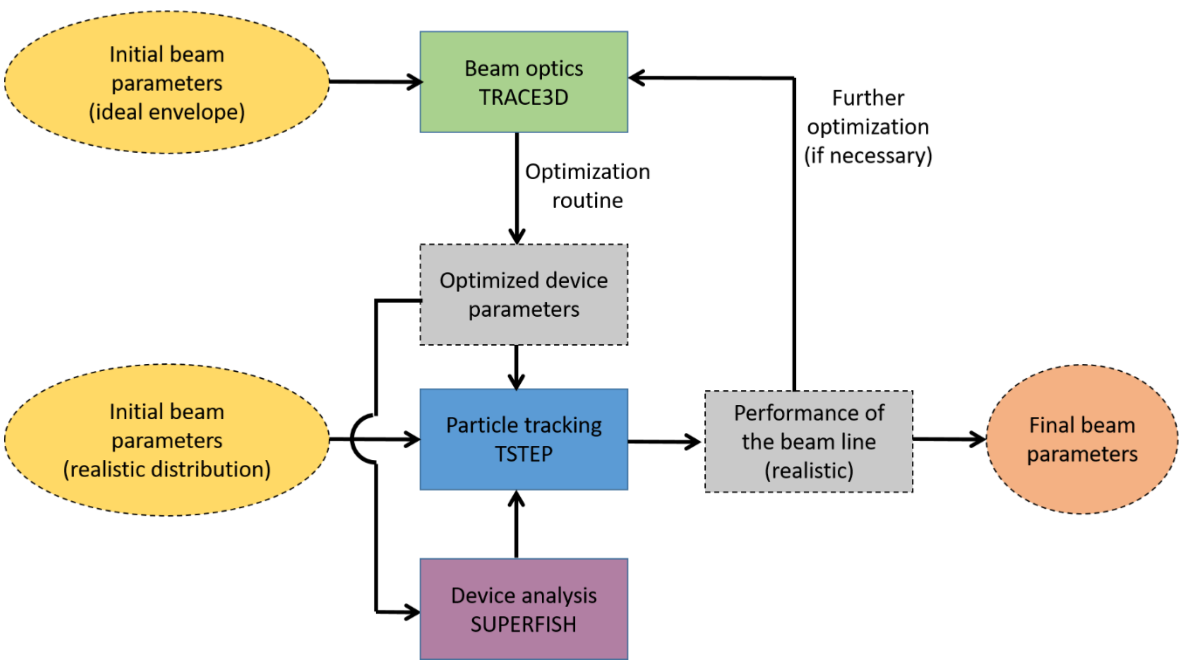

Fig. 5 – Iterative method for the analysis of a particle beam line. The workflow can be applied to both the cases of proton and electron beam line (obviously with some adjustments according to the needs of the specific cases).

The first step of the above mentioned methodology is to define the initial beam parameters that are representative for the laser-plasma particle source (electrons or protons). At first, these parameters are expressed in terms of the Twiss parameters, β and ε (i.e. the beam transverse dimensions and divergence; see Appendix I for further details) and can be processed by the beam optics code TRACE3D. As it is not possible to define a particle distribution of the bunch, the

scenario treated by TRACE3D is ideal. Furthermore, the elements of the beam line (e.g. dipoles, quadrupoles etc.) are ideal, i.e. we do not use a realistic magnetic field profile with TRACE3D.
The matching algorithm of TRACE3D allows optimizing the parameters of the beam line's devices by setting goal Twiss parameters for the desired final particle beam (e.g. as it will be discussed in Chapters 3 and 4, for optimizing the spacing of a quadrupole array). Hence, the user needs to define the element types that are present in the beam line and fix some of their physical parameters. Free parameters can be chosen that will be optimized by the code.
This step of the iterative procedure can be performed using codes other than TRACE3D. In Chapter 3, we discuss the optimization of an achromatic beam line for a laser-accelerated electron beam that has been done with MAD-X, an optical code similar to TRACE3D, which provides a more powerful matching algorithm, better suited for simulating complex beam lines.

Once the parameters of the devices have been optimized, the beam line needs to be tested with a particle tracking code. For our studies we used TSTEP, a derivative of PARMELA. The reason for this, is that realistic initial beam configurations need to be taken into account and information about the normalized beam emittance require the tracking of the single particles and cannot be done with the optical codes.
At this step, we defined realistic input beam distributions of the particles, according to the typical features of laser-plasma beams. The simulations of electron beams in Chapter 3, for example, have been performed using Kapchinsky-Vladimirsky distributions [5] with an uncorrelated $x - x'$ phase space and the typical transverse dimension and divergence of laser-generated electron beams. For the case of the proton beams of Chapter 4, it was possible to reproduce the typical energy spectrum of TNSA beams, as well as the beam divergence as a function of the particles' energy.
Once the initial beam parameters have been defined, the beam line devices with optimized parameters can be simulated and the performance of the beam line is tested for a realistic scenario.
In most cases, the analysis of the beam line simulated with the particle tracking code, gives different results from what is expected according to the previous beam optics simulations. The optimized parameters behave well for an ideal particle beam but they perform less efficiently with a realistic beam distribution. For this reason, as reported in the chart of Fig. 5, a feedback to the beam optics code is necessary: we slightly change the physical parameters of the beam line and run the optimization algorithm again. For instance, if at the first iteration the focusing strength of a quadrupoles' array has been optimized, the second optimization with TRACE3D can be done by fixing the focusing strength at the optimal value and optimize the spacing between the quadrupoles.
The iterations between particle optics code and particle tracking code are concluded when the simulations with realistic beam parameters deliver satisfying results and the performance of the beam line cannot be improved any further. The last analysis delivering the final beam parameters is always done with the particle tracking code.

In order to make the particle tracking simulations even more accurate, it is possible to define realistic field profiles for the beam line's devices.

The components' parameters that are simulated with TSTEP are ideal, unless differently imposed by the user: the magnetic field of dipoles, for instance, does not take into account fringe fields, unless complex geometries of the component are defined.
By using an electromagnetic field solver, such as SUPERFISH (and its extension PANDIRA, for magnetostatic analysis), it is possible to simulate the accurate geometry of the devices of the beam line. The user can simulate elements with customized dimensions, geometry and materials, obtaining accurate information about the resulting field configuration. Such analysis have two main goals:

1) Obtaining realistic field profiles of the beam line's elements that can be imported into the particle tracking code for even more accurate simulations. The analysis of the energy selector of paragraph 4.5.5 involves the realistic field profile of a sequence of rare-earth-magnet dipoles, for example.
2) Testing the feasibility of the devices that are simulated and optimized with the beam dynamics codes. The permanent-magnet quadrupoles of paragraph 4.5.6 have been simulated with SUPERFISH, in order to make sure that the magnetic gradients used for the simulations, are compatible with the available commercial rare-earth materials and the physical dimensions of the quadrupoles (i.e. inner and outer radius).

Concluding, the iterative method of Fig. 5, which is commonly used for tackling beam dynamics studies of conventional accelerators, can be adapted to the case of laser-accelerated beams. Especially the particle tracking simulations allow studying particle beams with customized initial parameters that are representative for typical laser-plasma generated particle bunches.
Obviously, other numerical tools that are not reported in the scheme above can be used as a support. We have performed the data analysis, e.g. of the results from the TSTEP and SUPERFISH codes, with MATLAB. The input particle distributions can be easily generated using the TSTEP name-list or with the use of simple computing routines (e.g. with FORTRAN). Moreover, using the output of Particle-In-Cell (PIC) codes allows obtaining even more realistic initial conditions of the particle tracking simulations. The calculations of paragraphs 3.5.2, 4.5.5 and 4.5.6 have been performed using such input data (specifically, for the latter two cases, using the PIC code PICLS-2D [6]).

The numerical results that are discussed in Chapters 3 and 4 of this thesis represent a basis, i.e. a starting point, for experimental campaigns.

References

[1] K. R. Crandall and D. P. Rusthoi, "LANL Report LA-UR-97-886," 1997.

[2] L. M. Young, "LANL Report LA-UR-96-1835," 1996.

[3] H. Grote and F. Schmidt, *Proceedings of PAC 03 (Portland),* pp. 3497-3499, 2003.

[4] K. Halbach and R. F. Holsinger, *Particle Accelerators,* vol. 7, pp. 213-222, 1976.

[5] I. M. Kapchinsky, Theory of resonance linear accelerators, New York: Harford Academic Press, 1985.

[6] Y. Sentoku and A. J. Kemp, *J. Comput. Phys.,* vol. 227, pp. 6846-6861, 2008.

3. Analysis of a laser-driven electron beam line

3.1 Introduction

This study aims to determine the acceptance parameters of laser-driven electron sources that make them exploitable as a viable alternative to conventional accelerators for FEL applications. We propose an analysis of the performance of laser-driven electron beam lines and give a comparison of the obtained results with what can be obtained on conventional accelerator facilities. We report on different techniques in order to capture and transport electron beams generated by a laser-plasma interaction. Our study is based on methodologies, as used on conventional accelerator facilities.
We point out the key parameters which still need to be improved—or can be acceptable—in order to make these new electron sources compatible with FEL applications where currently only conventional accelerators are used. To do so, we have performed a parametric study focusing on the relevant beam features at the source, i.e., beam divergence and energy spread. These are the electron beam parameters that have the most significant effect on the quality of the beam for the capture and transport.

As discussed in Chapter 1, compared to conventional, RF technology based accelerators, a plasma can provide an accelerating field of up to TV/m, thus giving the possibility of accelerating an electron bunch to energies in the GeV range in a distance of a few cm.
Even if laser-driven electron acceleration schemes nowadays still do not reach the highest range of energy achieved by conventional accelerators used for particle colliders (i.e. tens of GeV, for example at the SLAC linear collider), the state-of-the-art electron beams that have been obtained experimentally allow exploiting several applications, from the point of view of the required energy.
The most popular and interesting application for high-energy, laser-accelerated electron beams is to drive Free Electron Lasers (FEL). Today many conventional facilities are using electrons in the range of few GeV, such as the FERMI at Elettra FEL (Fig. 1) in Italy which is driven by a 1.5 GeV electron beam, the SwissFEL at PSI in Switzerland which has a maximum electron beam energy of 5.8 GeV, and the SESAME FEL, in construction in Jordan, which will have a 2.5 GeV electron bunch [1] [2] [3].

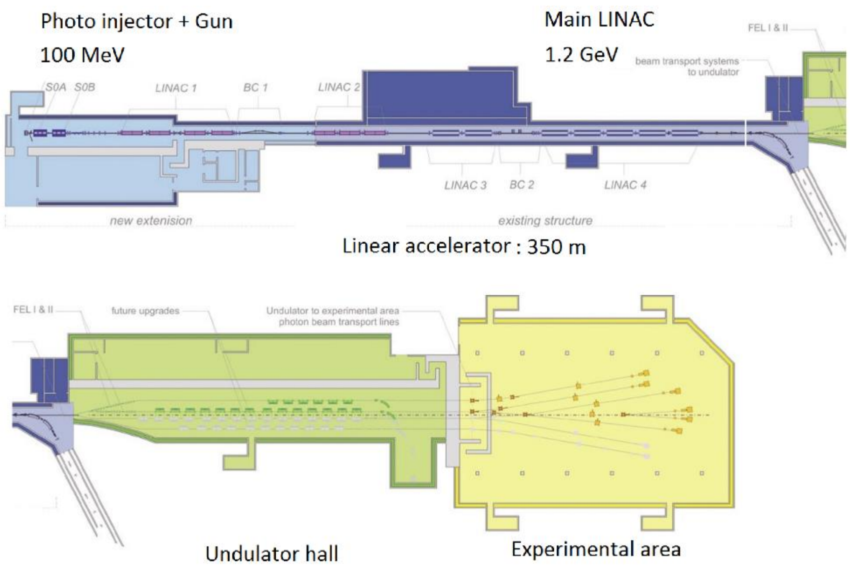

Fig. 2 - Schematics of the Fermi @ Elettra Free Electron Laser facility. The linear accelerator produces an electron beam with energy up to 1.5 GeV (blue) that is injected into undulators (green). The generated FEL radiation is directed into an experimental area (yellow). Extracted from the FERMI @ Elettra design report [31].

As shown in Fig. 1, FEL sources that use conventional accelerators to drive the radiation emission, require large scale facilities, since achieving high electron beam energies with conventional devices requires long accelerating sections (see the blue part on the left of the scheme) that reach tens, up to hundreds of meters. The electron beam is then transported to magnetic undulators in the application halls (green and yellow areas of Fig. 1).

There have been several studies that aim at implementing a laser-driven electron accelerator for FEL applications [4] [5] [6]. Compared to a conventional facility where a conventional accelerator is used, a laser-driven FEL source has the advantage of being more compact and less expensive. Moreover, laser-accelerated electrons provide a high charge and a short bunch duration that is not achievable with conventional acceleration schemes, which represents an innovation in FEL sources, allowing to obtain high quality and high brilliance[1] FEL beams.

The brilliance of the generated FEL radiation is linked to the brightness of the driving electron beam, i.e. to its charge and geometric features. The brightness B is defined by Dimitri et al. as

$$B = \frac{I}{\varepsilon_x \varepsilon_y}, \tag{3.1}$$

[1] The brilliance of an X-ray source, such as a FEL, is an important parameter of quality. It is commonly defined as

$$brilliance = \frac{photons}{second \cdot mrad^2 \cdot mm^2 \cdot 0.1\% \, BW},$$

Where BW is the bandwidth around the central wavelength of the emitted radiation [30].

where I is the beam current and ε_x and ε_y , respectively, are the x- and y- emittance of the beam; in some cases, the brightness is also defined as the beam current divided by the product of x- and y-emittance and by the energy spread [7]. On conventional accelerators driving FEL sources, the normalized emittance is of the order of $\sim$1 mm mrad, and the peak current is in the multi-hundreds Ampere regime: the linac at SPARC-LAB (at INFN-LNF) produces a bunch charge of $\sim$10 pC with a normalized emittance of <1 mm mrad (energy spread $\sim$0.1 %), the SwissFEL at PSI accelerates bunches with charge of 10–200 pC and a normalized emittance of 0.2–0.7 mm mrad (energy spread <0.02 %), and the FERMI linac at Elettra Sincrotrone Trieste drives a FEL with a charge of 800 pC and a normalized emittance of 1.5 mm mrad (energy spread <0.1 %) [1] [2] [8].

A possible layout of a FEL, driven by a laser-plasma accelerator is reported in Fig. 2, where the linear accelerator, that provides the electron beam, is replaced by a laser-plasma interaction point that generates and accelerates the electron bunch. Studies such as Ref. [5] demonstrate that the electron beam parameters at the laser-plasma source are well suited for driving a FEL. However, the transport of the beam from the source to the magnetic undulator is a crucial aspect of this scheme and is still a topic of research: laser-generated electrons still lack of control, stability, and repeatability in order to be considered a replacement for conventional accelerator beam lines [9] [10]. For any application and at whatever given energy, the beam has to be captured from the source and transported to its final application, preserving as much as possible the good properties of the source. The transport and manipulation of laser-generated electron beams is a topic of high interest for both communities of conventional and laser-plasma accelerator science.

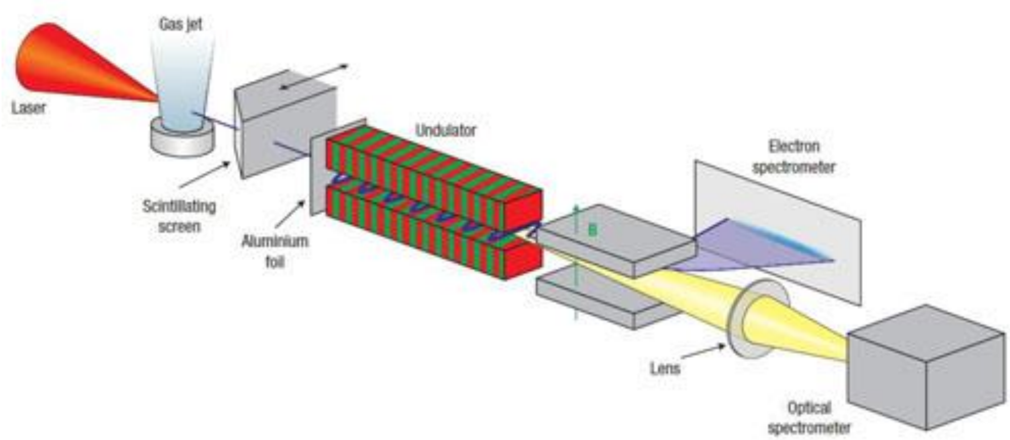

Fig. 3 – Possible scheme of a FEL driven by a laser-driven accelerator. The conventional accelerator is replaced by a laser-plasma electron source providing the beam that is injected into the undulator. Extracted from Ref. [6].

3.2 Methodology and content of the study

The analyzed transport lines for laser-generated electron beams rely entirely on conventional magnetic devices such as solenoids, dipoles, quadrupoles and sextupoles. Various beam line configurations (of different levels of complexity) have been studied and evaluated from the point of view of their ability to transport the electron beam efficiently, i.e. keeping the initial beam quality that is featured at the laser-plasma source. The beam parameters have been calculated at the electron source and after the transport beam line, with numerical tools for beam dynamics analysis. The beam optics codes TRACE3D and MAD-X have been used for optimizing the beam line devices and the particle tracking code TSTEP has been used for an accurate, final test of the beam line (see Chapter 2 for further details). Moreover, we used a parametric approach to determine acceptable initial values of the main initial beam parameters that allow an efficient beam transport. Different initial sets of parameters of the electron beam have been considered, varying both geometrical features such as beam divergence and energy characteristics of the electrons, i.e. the mean energy of the bunch and the energy spread of the accelerated electrons.

The energy and the beam parameters of electron bunches accelerated by laser-plasma interaction vary according to the set-up of the laser-driven source. In particular, the energy of the electron beam is strongly dependent from the power of the laser pulse that interacts with the under-dense plasma (i.e. a plasma with a density in the order of magnitude of $< 10^{21}\ cm^{-3}$) and drives the acceleration process.
In order to characterize the most significant conditions at the plasma source, our study is focused on two different regimes of laser-plasma interaction: (1) optimizing laser-generated electron beams at high energy (GeV), as obtained on PW-level lasers [11] or as foreseen on high-power laser facilities currently under construction [12]; (2) optimizing laser-generated electrons in the multi-hundreds of MeV range, as measured on different state-of-the-art facilities using a commercially available hundred-terawatt (TW)-class laser [13] [14] [15] [16]. By investigating both, higher- and lower-energy electron beams, we are able to cover a wide range of scenarios. We have analyzed several beam line configurations, varying the beam divergence and energy spread at the entrance of the beam line and studying the efficiency of the transport process.

In particular, for low energy beams, we consider the application of laser-accelerated electron bunches for driving FEL sources, where the beam quality at the experimental station is of crucial importance: the normalized emittance (i.e. the laminarity) of the electron beam is required to be within a certain range of values (see Paragraph 3.6 for further details) [7]. Hence, the electron beam stemming out of the laser-plasma source needs to be adapted to the FEL source by keeping its normalized emittance as low as possible. Laser generated electrons can be fully exploited as driver for FEL radiation only if the emittance and the geometric features of the beam meet high quality requirements. In Ref. [4] an energy spread of 1 % (even 0.1 % for GeV electron beams), a beam spot size of 30 μm and a transverse emittance ranging from 0.1 to 1 mm mrad are considered.
For laser-accelerated electron beams, as discussed within Appendix I, the evolution of the normalized emittance throughout a transport line, is an important aspect that is worth to investigate in detail. The beam parameters of a laser-plasma electron source are unusual, if

compared to conventional accelerators, in terms of divergence and energy spread, as will be reported in the following paragraph. This generates a particle bunch configuration that leads to the emittance growth effects that we discussed in Paragraph 2.3 [10] [17].
For these reasons, in our research, we determine the acceptance parameters of the laser-driven source that make them exploitable as electron source in terms of the final value of normalized emittance and give a comparison of the obtained results.

The methodology we have used for this study is explained in Paragraph 2.2, where the iteration between the beam optics and particle tracking codes is discussed in detail. For the study of the beam lines reported in this chapter, we have used such a method.

We used the numerical codes TRACE3D [18] (or MAD-X [19]) and TSTEP (a derivative of PARMELA) [20] for analyzing the electron beam lines (see Chapter 2 for further details). As discussed in Paragraph 2.1, the first is an optical code that accounts for the envelope equations of the particle bunch throughout the beam line. It is very well suited for optimizing the scheme of the beam line, under the assumption that the particle bunch has a uniform, ideal particle distribution. TRACE3D allowed obtaining the best parameters of the elements of the beam line, and their spacing, for a set of goal parameters that the beam has to match at the end of the beam line.
As TRACE3D cannot simulate realistic customized particle distributions, in order to simulate laser-accelerated beams more accurately, the particle tracking code TSTEP has been used additionally. The initial bunch parameters that are typical of laser-plasma sources involve effects that can be studied only if the trajectory of each particle is calculated. For example, the high value of energy spread of laser-accelerated electrons leads to significant chromatic effects within the focusing elements of the beam line, which can be correctly evaluated only if the beam has a realistic initial distribution in space and in energy. For this reason, the initial simulations run with TRACE3D have been simulated again, for both the cases of a proton and electron beam line, with TSTEP.
For the cases of symmetric beam lines (Paragraphs 3.6.4 and 3.6.5), the code MAD-X has been used instead of TRACE3D. MAD-X is an optical code, as well, with a more efficient optimization algorithm that is well suited for the simulation of more complex beam lines.

3.3 Laser-acceleration of quasi-monoenergetic electron bunches, exploiting the bubble regime

In this paragraph we briefly introduce the non-linear bubble regime [21] that represents the state-of-the-art acceleration regime for high energy, quasi-monoenergetic electron beams. The typical beam parameters that we have used for our studies, reported in Paragraphs 3.5 and 3.6, are obtainable with this particular acceleration regime.
Moreover, we present two techniques to improve the laser-plasma interaction process that generates and accelerates the electron bunch. These techniques that aim to obtain low divergence and low energy spread electron bunches at the laser-plasma source, have been used in the experiments that provided the electron beam that we investigate in this study.

3.3.1 The bubble regime mechanism

In a plasma, which is non-collisional and uniform, the electrons that are displaced from their initial equilibrium position, will experience a restoring force that pulls them back to their initial position. This is the case when an intense laser pulse irradiates the plasma region: the oscillating electric field generates a ponderomotive force that displaces the electrons of the plasma normally, with respect to the propagation path of the laser itself. The ponderomotive force experienced by a charged particle in an oscillating electric field is

$$F_p = -\frac{e^2}{4m_e\omega^2}\nabla(\mathrm{E}^2)\,, \tag{3.2}$$

where ω is the frequency of the oscillating electric field, e the electron charge, m_e the electron rest mass and E the electric field of the laser pulse.

On a short time scale, such as the one we consider for electron acceleration phenomena (from fs up to ps), the ions of the plasma are too heavy to be moved by the field of the laser pulse and can be considered as static. Indeed, only the electrons are displaced by the traveling laser pulse and due to the restoring force exerted by the plasma, they oscillate with a plasma frequency that is

$$\omega_{pe} = \sqrt{\frac{n_e e^2}{m_e \varepsilon_0}}\ \ , \tag{3.3}$$

where n_e is the unperturbed electron density of the plasma and ε_0 the vacuum permettivity.
The bubble regime is triggered by the non-linear interaction between the laser pulse and the plasma. The bubble region is generated when the dimension of the focused laser pulse is smaller than the plasma wavelength λ_{pe} (defined by the plasma frequency of Eq. 2) in both transverse and longitudinal direction and the intensity of the pulse is high enough. In this case the laser pulse appears like a traveling sphere of light, the electrons are expelled radially from the path of the pulse and a trailing region, almost empty of electrons, is created. Typically, the plasma density that is used most efficiently for the bubble acceleration is between 10^{17} and $10^{19}\ cm^{-3}$, leading to a plasma wavelength of a few µm. The laser pulse duration that is required for generating the bubble is in the order of magnitude of a few fs (up to a few tens of fs, depending on the plasma density). The laser intensity that is necessary to generate the non-linear plasma oscillations of the bubble regime, requires a laser vector potential $a_0 \geq 2$, where
$a_0 \simeq 0.8\ (\lambda_0 \backslash 1[\mu m])[I\ /\ 10^{18}\ W \cdot cm^{-2})]^{\frac{1}{2}}$ (being λ_0 the central wavelength of the driving laser pulse). Typically, laser pulses from Ti:Saphire systems are used, having a duration of a few tens of fs. As the laser pulse if focalized at the laser-plasma interaction point, the intensity is routinely $\geq 10^{18}\ W \cdot cm^{-2}$.
On the border of this cavity, the electrons' trajectories intersect with each other and create a high density electron layer that surrounds the void region. Due to the electric interaction with the plasma's stationary ions, some of the background electrons of the plasma are injected into

the cavity and accelerated along the propagation axis of the laser. An electron bunch is injected at a distance of about λ_{pe} from the trailing laser pulse. At the border region of the bubble, due to the charge separation, a strong electric field is generated that can reach values in the order of GV/cm. The mechanism of the bubble acceleration regime is shown qualitatively in Fig. 3.

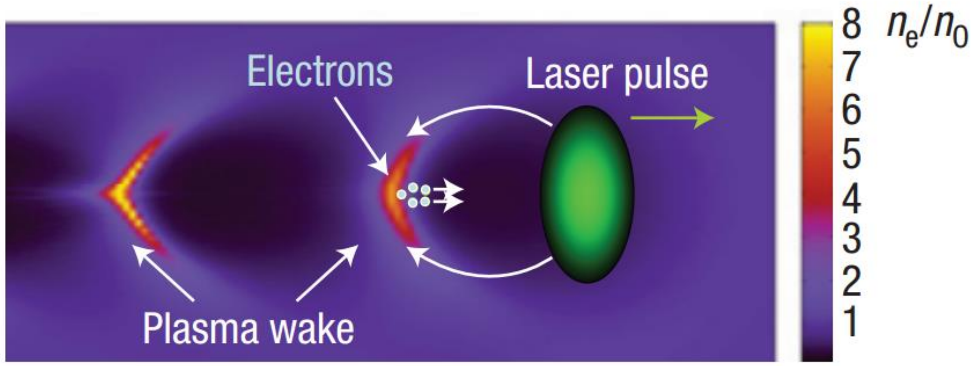

Fig. 4 – The bubble regime as represented with a PIC simulation code. The trailing laser pulse generates a spherical region, empty of electrons. An electron bunch is injected at the tail of the bubble region and is accelerated along the path of the laser. Extracted from Ref. [32]

With this regime, high quality, high-energy electron beams have been obtained. Typically, acceleration regimes involving linear wake field effects provide electron beams with a Maxwellian energy distribution, i.e. with an energy spread of up to 100 %. Differently, the electron beams obtained with the non linear bubble regime have a significant peak in terms of number of particles, at the maximum energy. An energy spectrum obtained with this regime is shown in Fig. 4. The transition from the linear to the non-linear bubble acceleration regime has been studied experimentally at the LOA laboratory (France), where the density of the used gas-jet has been changed gradually, finally obtaining energies of >100 MeV with a charge of >100 pC [22]. The longitudinal dimension of the electron beam is linked to the laser pulse shape and can be obtained as small as a few µm, i.e. a temporal duration of the bunch of <10 fs.
This acceleration regime allows obtaining electron beams with a mean energy of hundreds of MeV, with an energy spread of a few percent, using a commercial laser system with a power of tens/hundreds of TW. With upcoming PW-power-class lasers, even energies in the GeV range have been obtained as reported by Leemans et al. in Ref. [11] where an electron beam energy of 4.2 GeV has been obtained.

As can be seen from the spectrum in Fig. 4, the laser-plasma electron bunch accelerated with the bubble regime, has an energetic distribution that is more similar to what is obtainable with conventional accelerators, if compared to the case of a Maxwellian spectrum, obtainable with lower intensity regimes. For this reason, this kind of electron beams are well suited for the study of a transport line after the laser-plasma source.

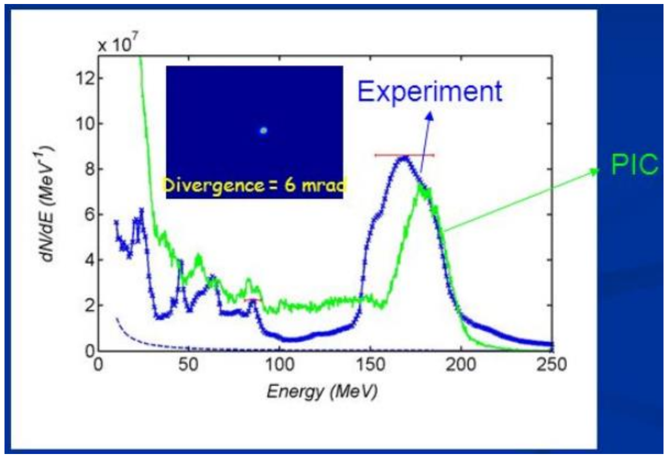

Fig. 5 – A typical spectrum of a laser-accelerated electron beam obtained with the bubble-regime during an experiment held at the LOA laboratory [22].

3.3.2 Techniques for improved laser-plasma electron sources: state of the art of electron beams from TW and PW laser systems

Even if the features of the electron beams accelerated with the bubble regime represent a significant improvement, if compared to other less recent acceleration regimes, the study of techniques for improving the quality of the electron source is a popular topic of research. Attempts have been made, successfully, to lower the electron beam divergence and to achieve a lower energy spread of the accelerated electron bunch, by improving the laser-plasma interaction process.

For instance, the plasma that generates and accelerates the electron beam can be injected into a capillary. This leads to a more controlled and uniform density of the gas pressure and allows obtaining an electron beam that is better collimated at the exit of the plasma region. Fig. 5 shows the capillary used by Leemans et al. for an electron acceleration experiment at the Lawrence Berkeley National Laboratory (BNL) using the PW-power laser system BELLA [11]. During this experiment a 0.3 PW power laser pulse has been focused into a 9 cm long capillary containing a $\sim 7 \times 10^{17}\ cm^{-3}$ dense plasma. The obtained electron bunch reached 4.2 GeV maximum energy with a charge of 20 pC. The transverse divergence of the electrons was only 0.5 mrad wide, significantly less than typical values for such energetic laser-accelerated electron beams. These experimental results are reported in Fig. 6.

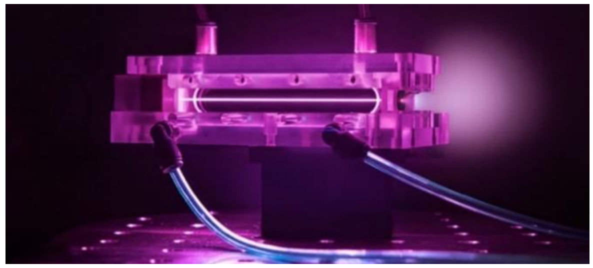

Fig. 5 – The capillary used by Leemans et al. at the BELLA laser facility. The underdense plasma is confined into a 9 cm long gas cell where the electrons are generated and accelerated.

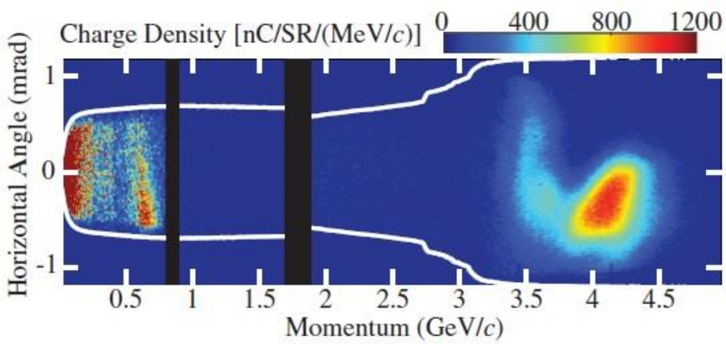

Fig. 6 – Accelerarted electron bunch at the BELLA laser facility. The electrons have been accelerated by a 16 J energy laser pulse, achieving a maximum energy of 4.2 GeV with an energy spread of 6% (FWMH). Extracted from Ref. [11].

Another way to improve the quality of the laser accelerated electron beam, is based on the use of more than one laser pulse to generate the plasma and to accelerate the electron bunch. The purpose of using two different laser pulses is to shape the density of the plasma in which the acceleration process takes place. Experimental evidence provided by Faure et al. [23] and, later on, by Fourmaux et al. [13] reports that a plasma with a sharp density gradient allows obtaining a quasi-monoenergetic electron beam with a high probability. The results shown in Fig. 7 and 8 have been obtained by using two laser pulses crossing each other into the plasma with an angle of 90 degrees. The experiment has been performed at the ALLS laser facility at INRS (Canada).

The first pulse is used to ionize and heat a He gas locally creating a plasma channel, leading to an enhanced electron injection into the accelerating structure. The second pulse drives the wake-field that accelerates the electron bunch. As shown in Fig. 8, by optimizing the temporal and spatial delay (indicated in the paper with the z direction) between the two laser pulses, it is possible to increase the probability of obtaining a quasi-monoenergetic electron beam, i.e. with an energy spread of ≤10 %, and increase its mean energy. From the graph of Fig. 8, we can see that for an optimized spatial delay between the two laser pulses (of about 3.5 mm) the probability of obtaining a quasi-monoenergetic electron bunch is <60 %, compared to almost 0 % for mismatched crossing laser pulses.

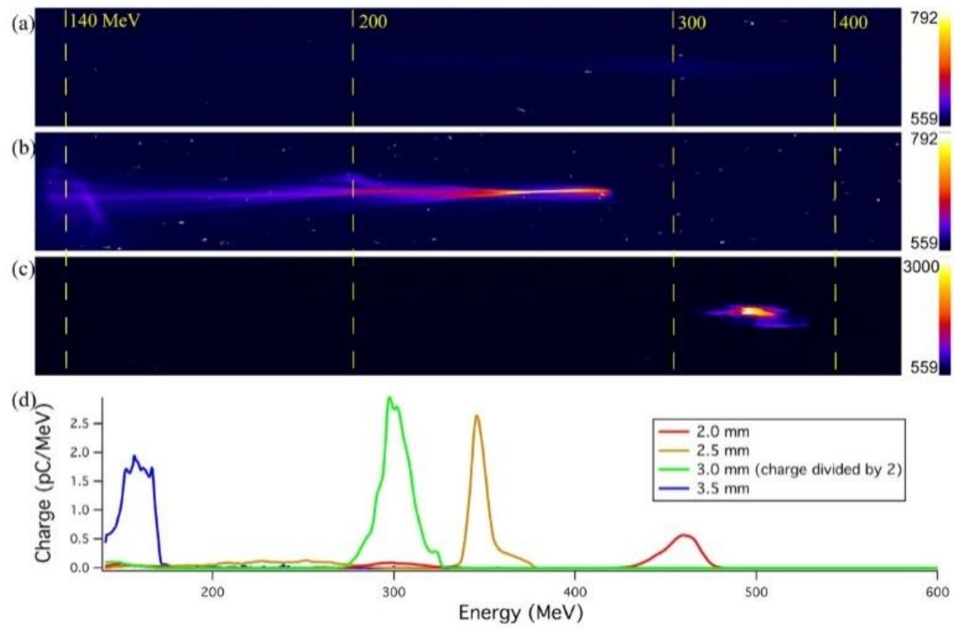

Fig. 7 - Electron spectra obtained by Fourmaux et al. (a) and (b) Raw spectrum without laser crossing pre-pulse. (c) Raw spectrum with laser crossing pre-pulse focused at z = 3 mm. (d) Calibrated spectra with laser crossing pre-pulse focused at z = 3.5, 3, 2.5, and 2 mm (respectively blue, green, brown, and red). Note that the charge has been divided by 2 for position z = 3 mm to keep the charge scale. The intensity scale in counts is indicated on the left for pictures (a), (b), and (c). Note that the intensity scale is different on picture (c) from pictures (a) and (b). Extracted from Ref. [13].

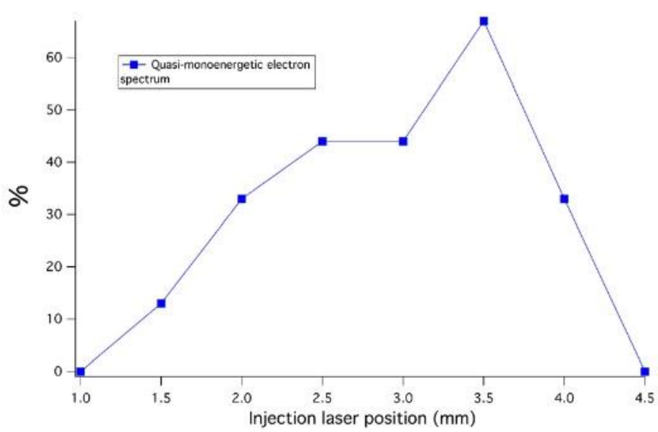

Fig. 8 - Probability to get quasi-monoenergetic spectra as a function of the crossing pre-pulse z position. Extracted from Ref. [13].

3.4 Capture and transport line of high energy (8 GeV), laser-accelerated electron beams

We report in this paragraph the main results that we have obtained concerning the analysis of the beam line optimized for a high energy electron beam.
The methodology and the tools we have used are the ones discussed in Chapter 2.
For the focusing quadrupoles of the beam lines we have analyzed, we took as reference the devices shown in Paragraph 1.4.3.

The high-energy electron beam that we have considered for the first optimization study has characteristics similar to those obtained in Ref. [11] when using a PW-class laser (laser pulse with wavelength 800 nm, energy 16 J, pulse duration 40 fs, beam waist 50 μm, hitting a 9 cm long capillary discharge waveguide with a plasma density of about $\sim 7 \times 10^{17}\ cm^{-3}$). The parameters we used for generating the particle distribution (given as input for the simulations) are shown in Table I. We have studied the behavior of the electron beams using different mean electron energies, taking into account less energetic (but more stable) working points and future laser developments generating higher energies. The parameters used for the simulations and listed below are to be considered at the laser-plasma source.
The aim of this part of the study is to analyze the behavior of a capture/transport line, based on a solenoid or quadrupole triplets, with respect to different electron beam energies.
In our methodology, we have adopted a similar approach to what is done with conventional accelerator beams (and beam lines), i.e., simulating the behavior of the beam with particle tracking codes and optimizing beforehand the beam transport and capture section with beam optic solvers. For the beam optic devices, we considered typical conventional beam handling devices such as quadrupoles and solenoids.

Mean electron energy	8–1–0.5 GeV
Relative energy spread (rms)	6%
Bunch length (rms)	4 μm
Transverse spot-size (rms)	1 μm
Transverse divergence (rms)	0.5 mrad
Normalized emittance	10–1–0.5 mm mrad

TABLE I. Characteristics of the electron beam at the laser-plasma interaction point for the high energy case (8 GeV) as obtainable from a PW laser system.

3.4.1 Optimization of a capture quadrupole triplet for an 8 GeV electron beam with TRACE3D

At first, we considered the most difficult scenario for the beam line, i.e., using an electron beam with a mean energy of 8 GeV (see Table I). Such beams are particularly difficult to handle due to the steep growth of the normalized emittance that is caused by the relatively high energy spread and large divergence (as discussed in Paragraph 3.3) [10]. Moreover, at such high energies, the beam is "frozen" due to relativistic effects and therefore hard to handle, requiring the use of extremely high magnetic fields within the focusing devices. We started with the easiest configuration for capturing the beam, which is the one using a quadrupole triplet (a sequence of three quadrupoles, the first and third focusing on one axis, the second on the other).

We optimized the capturing beam line with the code TRACE3D with the constraint to have an almost uncorrelated transverse phase space distribution at the end of the beam line and respecting minimum technical requirements (e.g., distance of a few cm from the laser-interaction point).
The code allows optimizing the main physical parameters of the magnetic quadrupoles and the spacing between them. As the matching routine is more efficient with only one (maximum two) free variable, we chose to fix the magnetic field of the quadrupoles and the distances between them, allowing the matching algorithm to adjust the length of the magnetic elements.
The initial beam parameters are those of Table I and the geometric features of the electron bunch can be defined by setting initial values of the Twiss parameters α and β. The value of Twiss β is given by the transverse dimension and geometric emittance of the electron beam (as discussed in the previous paragraph). Recalling the definitions of beam transverse dimension and divergence (see Appendix I), we have that

$$\sigma_x = \sqrt{\langle x^2 \rangle} = \sqrt{\beta \varepsilon_{rms}}$$

$$\sigma'_x = \sqrt{\langle x'^2 \rangle} = \sqrt{\gamma \varepsilon_{rms}}$$

Where σ_x is the transverse RMS spot-size of the beam and σ'_x the RMS divergence of the particles. Moreover it holds that $\gamma\beta - \alpha^2 = 1$, with $\alpha = -\frac{\beta'}{2}$.
For a particle beam with no significant correlation between transverse position of the particles and their transverse momentum, we have that $\alpha = 0$.
In our case, for simulating an electron transversely non-correlated beam with a transverse RMS dimension of 1 µm and a RMS divergence of 0.5 mrad we obtain the following initial Twiss parameters:

$\alpha = 0$
$\beta = 2.0 \times 10^{-3}\, m$
$\varepsilon = 0.5 \times 10^{-9}\, m\, rad$

The optimization, which considers both the transverse dimensions and the beam divergence, was done by choosing acceptable goal values for the Twiss parameters α and β at the end of the transport line. In order to obtain a collimated beam at the end of the capture line, we chose $\alpha = 0$ and β between 100 and 200 m as final beam parameters (for lower β values, the algorithm fails to find matched values of the quadrupoles' length).
Moreover, we fixed the magnetic field gradient of the three quadrupoles at 500 T/m (-500 T/m for the central quadrupole), allowing the matching routine of TRACE3D to optimize their length. The spatial configuration, as reported in Fig. 9, foresees a distance of 10 cm of the first quadrupole from the particle source and a spacing of 1 cm between the quadrupoles.
In Fig. 9 we show the simulation results obtained with TRACE3D. The matching algorithm managed to optimize the beam line for the 8 GeV beam, when fixing a final value of beta down to 200 m. The optimized lengths of the three quadrupoles, according to the simulation, are:

L1= 30.57 cm
L2= 30.57 cm
L3= 15.64 cm

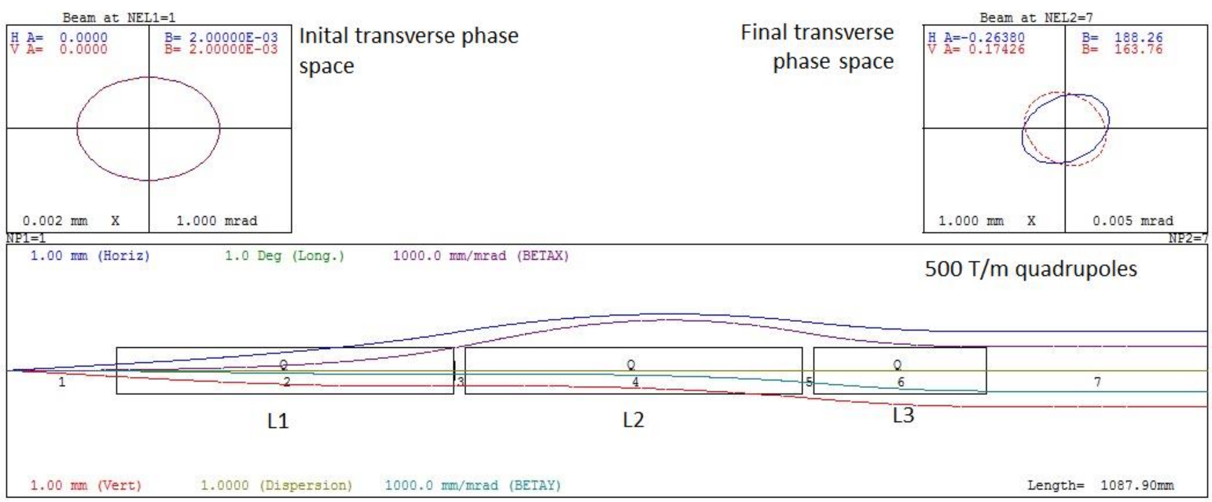

Fig. 9 - Electron beam transverse dimensions and divergence as obtained by the code TRACE3D for a 8 GeV electron beam.. Top-left plot: phase space of the initial electron beam. Top-right plot: phase space of the final electron beam. Bottom plots: Transverse dimensions of the electron beam (blue and purple curve: x-dimension; red and green curve: y-dimension), as a function of the distance from the laser-plasma source (z=0).

The beam is well collimated at the exit of the quadrupole triplet (blue and red curves, indicating the envelope of the bunch traveling through the quadrupole triplet) with a transverse dimension of about 0.3 mm, as can be observed in the top-right plot of Fig. 9, which indicates the transverse phase space of the final electron beam.

The strengths of the beam line quadrupoles (∼500 T/m) are unusual and can only be obtained with permanent magnets. However, they are still feasible with state-of-the-art technology involving rare-earth materials [24], but their length (∼30 cm) represents a technical challenge, since magnets made out of these materials are usually manufactured as blocks with quite small dimensions (5–10 cm). The distance between the electron source and the transport line, which we set between 8 and 10 cm in our simulations, is determined by limitations of the magnetic field gradient of the first quadrupole. The optimization of the distance with TRACE3D simulations showed that decreasing the distance between the source and the beginning of the transport line requires an increase in the field strength of the first quadrupole. When reducing the drift length before the beginning of the transport line, the electron bunch enters the first quadrupole with a smaller transverse dimension; in a quadrupole, the magnetic field drops to zero in proximity of the central axis, thus, a greater gradient is needed in order to focus a beam with a smaller transverse spot size.

3.4.2 TSTEP simulations of high energy electron beams: triplet capture line and multiple triplet transport line

TRACE3D optimizes the beam line by using particle optics and uses an ideal single particle transport matrix formalism: it calculates the beam emittance based only on the Twiss parameters without taking into account a realistic particle distribution. For this reason it is not possible to evaluate the efficiency of the beam transport line from the point of view of the normalized RMS emittance.
The evaluation of the RMS emittance of an accelerated particle beam requires information about the spatial distribution of the particles of the bunch. For this kind of analysis, particle tracking codes are commonly used for the study of conventional accelerators.
We verified the lattice structure by performing additional simulations using the code TSTEP that tracks the trajectory of each single particle of the input beam distribution.

For the 8 GeV electron beam we used a realistic Gaussian-like distribution for the transverse beam dimensions and divergence. The initial characteristics of the beam, as obtained in a previous study [25], are those of Table I. The configuration of the quadrupole triplet is the one obtained with the optimization routine of TRACE3D, as discussed in the previous paragraph.
In Fig. 10 we report the most important results that we were able to obtain with the particle tracking simulations. As we can see from the plotted curves at the end of the beam line, about 90 cm after the laser-plasma interaction point, the transverse beam size (plot a) and the normalized emittance (plot b) remain constant, which means that the beam has an almost stable transverse dimension. Indeed, the quadrupole triplet allows keeping the dimension of the electron beam under control along the whole path through the magnetic lenses.
However, it is important to highlight that while the transverse beam size is acceptable (0.35 mm), the normalized emittance is of the order of few hundred mm mrad at the end of the transport line (526.6 mm mrad and 173.3 mm mrad for x- and y-emittance, respectively). This value is very high with respect to what is obtained on conventional RF accelerators (typically below 10 mm mrad) and grows rapidly already in the first drift space between the plasma source and the first quadrupole.
The emittance growth in the first centimeters after the electron source is due to the emittance growth effect studied by Migliorati et al. [10] which is discussed in Appendix I. Furthermore, the magnetic quadrupoles are not capable of compensating this growing trend with their focusing

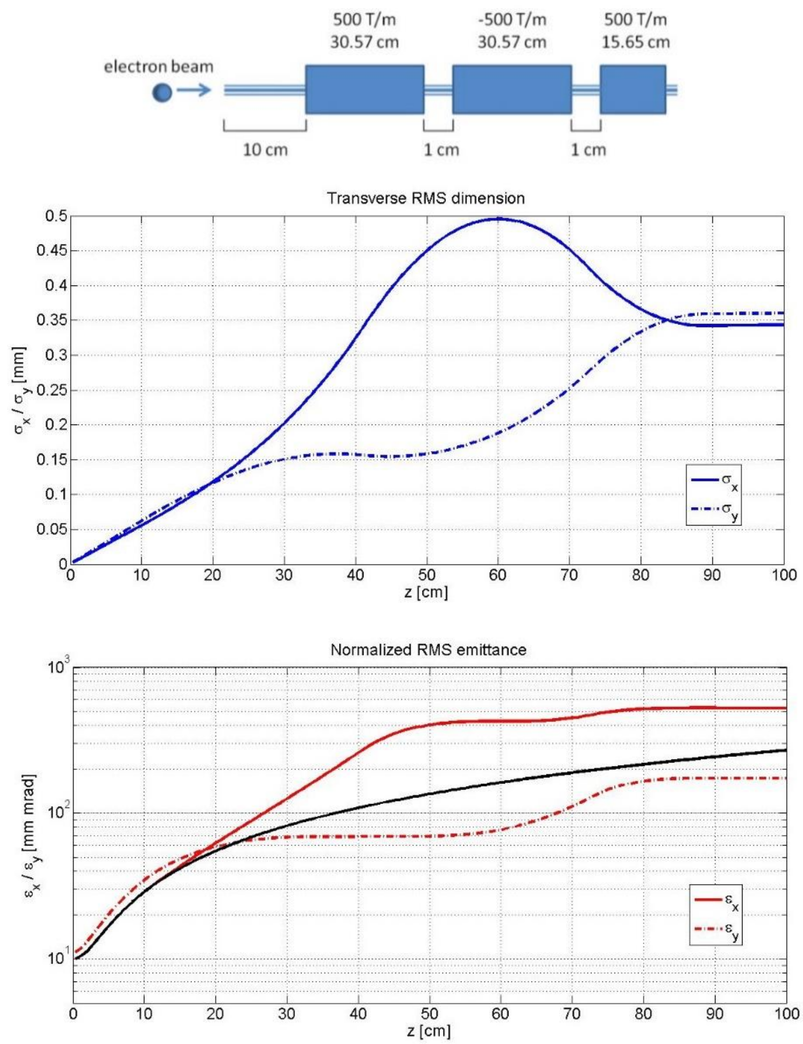

Fig. 10 – Results as obtained by the TSTEP simulations for a triplet capture line. Above the schematic of the triplet line. Top plot: Transverse beam size (RMS) of the electron beam traveling through the triplet. Bottom plot: Normalized RMS emittance of the electron beam traveling through the triplet. The black curve represents the emittance (x-plane) evolution of the beam in a free drift.

effect. When dealing with particle beams with high energy spread (as it is in this case) magnetic quadrupoles (or magnetic focusing devices, in general) present strong chromatic effects that lead to a worsening of the beam quality in terms of normalized rms emittance. Nevertheless, their use is necessary to transport and capture the beam after the source and, as it is visible form the black curve of Fig. 10, replacing the quadrupole triplet with an empty drift space does not lead to a significant improvement of the final value of the emittance (271.6 mm mrad for the x-emittance).

The parameters of the quadrupoles optimized with TRACE3D do not change significantly for a fluctuation of the mean energy of the beam up to 10%. A slight variation of the central energy only requires some fine tuning with TSTEP for the magnetic field gradient values of the quadrupoles.

Starting from the triplet capture design, we studied the possibility of improving the beam line performance, trying to reduce the normalized emittance and lowering the beam size. This has been done by optimizing the beam line with additional triplet modules, which have the further advantage of allowing to transport the beam over a longer distance.
The optimization has been done using the matching algorithm of TRACE3D with the same initial electron beam parameters as for the case of the simple triplet lattice (see Table I). For the second, third and fourth triplet, several optimization simulations have been run using different (fixed) values for the quadrupole length and for the length of the drift spaces between them. The best fitting values are reported in Fig. 11.
The beam parameters obtained at the end of the beam transport using additional triplet modules (i.e., after a length of $\sim$4.5 m) are shown in Fig. 11. We can see that it is possible to reduce the transverse dimension to $\sim$0.2 mm (top plot), but it is not possible to lower the emittance significantly with respect to the simple triplet structure (bottom plot).

As a conclusion, the additional cost and complexity of the four triplet system makes sense only if there is the need to reduce the transverse beam size or the beam has to be transported over longer distances. Unfortunately, it is not possible to obtain a normalized emittance comparable to that of the conventional RF accelerator for the case of FEL applications.

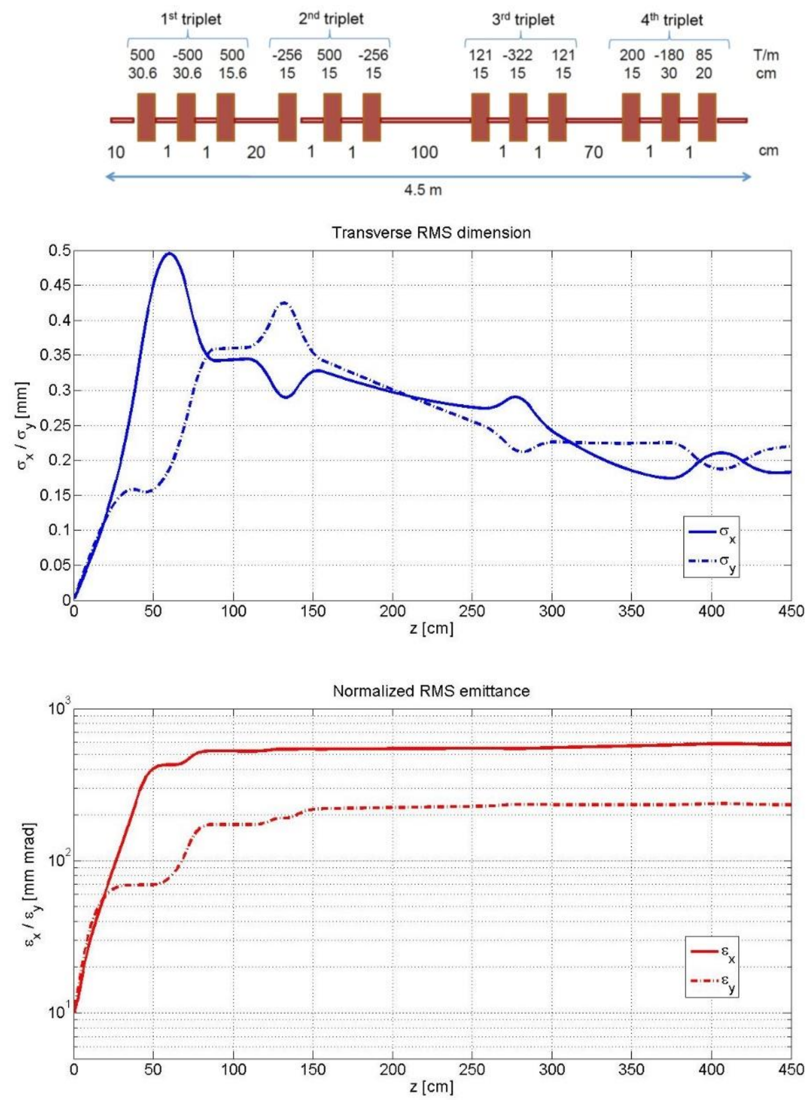

Fig. 11 – Transport line with a sequence of triplets as obtained by the TSTEP simulations. Above the schematic of the beam line. Top plot: transverse beam size (RMS) of the electron beam traveling through the beam line. Bottom plot: normalized RMS emittance of the electron beam traveling through the beam line.

3.4.3 Analysis of the triplet lattice structure, decreasing the electron beam energy (8 – 1 – 0.5 GeV)

In order to check the versatility of the capture line discussed in paragraph 3.4.2 for lower electron energies, we have optimized the triplet configuration for electron beams with maximum energy of 1GeV and 0.5 GeV.
When scaling down to the 1 and 0.5 GeV case, we did not change any other parameter than the energy indicated in Table I. Differently from the 8 GeV case, where we used a realistic Gaussian-like distribution for the transverse beam dimensions and divergence obtained in a previous study, [26] for the 1 and 0.5 GeV cases, we modeled the electron bunch with an ideal Kapchinski-Vladimirski distribution. This is the reason why the values of the normalized emittance, reported in Table I, do not change proportionally with changing beam energy. The 0.5 and 1 GeV beams represent a best case scenario, since they are modeled with an ideal particle distribution. The scaling of the energy allows establishing the trend of the emittance growth by simply decreasing the beam energy only.

The results, shown in Fig. 12, indicate once again that with a triplet we cannot avoid a strong worsening of the normalized emittance, which reaches values of $\sim$10 mm mrad for the case with mean energy of 0.5 GeV, even when considering a beam divergence of 0.5 mrad, which represents the best case scenario. However, by scaling the parameters of the 8 GeV line to lower beam energies, we see that the overall quality of the transported beam improves. Moreover, the structure of the capturing section requires quadrupoles with more relaxed values of the field gradients because the beam is less rigid (further details about the beam rigidity are given in the section concerning the calculations about the proton energy selector, Paragraph 4.5). The lower values of the magnetic field of the focusing quadrupoles induces less chromatic effects, which explains the improvement of efficiency in the transport process.

In our study we focused on laser-generated electron parameters as obtained by Ref. [11] and changed the mean energy. The beam emittance values that have been obtained for the 0.5 GeV are low if compared to those obtained in the low energy case (350 MeV), which will be discussed in the following paragraph, even if they grow by an order of magnitude. Hence, it is important to stress the fact that the low values of the normalized emittance in our beam line are only achievable because of the relatively small divergence of the electron beam at the source that we have used. The intrinsic divergence of the electron bunch at the source has a strong impact on the growth of the normalized beam emittance, as discussed in Appendix I.
The low divergence value of 0.5 mrad (as found in Ref. [11]) for a mean electron energy of 0.5 GeV (scaled from the 8GeV energy case) allows keeping a good beam quality throughout the quadrupole line in terms of both emittance and spot-size. However, this low divergence has been obtained experimentally for a quite low charge of $\sim$6 pC and might not be the same for higher beam charges. The results reported in Fig. 12 show clearly how a decrease of the energy makes the beam transport with a triplet more efficient in terms of beam transverse dimensions and emittance at the end of the quadrupole line. The scaling has only been done by lowering the electron mean energy, keeping all other beam parameters unvaried, as reported in Table I. By doing so, we were able to estimate the performance of the transport line in relation to the beam

energy only. We deduced from the energy scaling that the beam transport with conventional elements is better suited for wakefield- accelerated electrons beams driven by commercial laser systems (power range of hundreds of TW), where the maximum electron energy reaches a few hundreds of MeV. For this reason, we have investigated the beam transport lines for a different class of electron beams with a lower energy more in detail, as we report in the next paragraph.

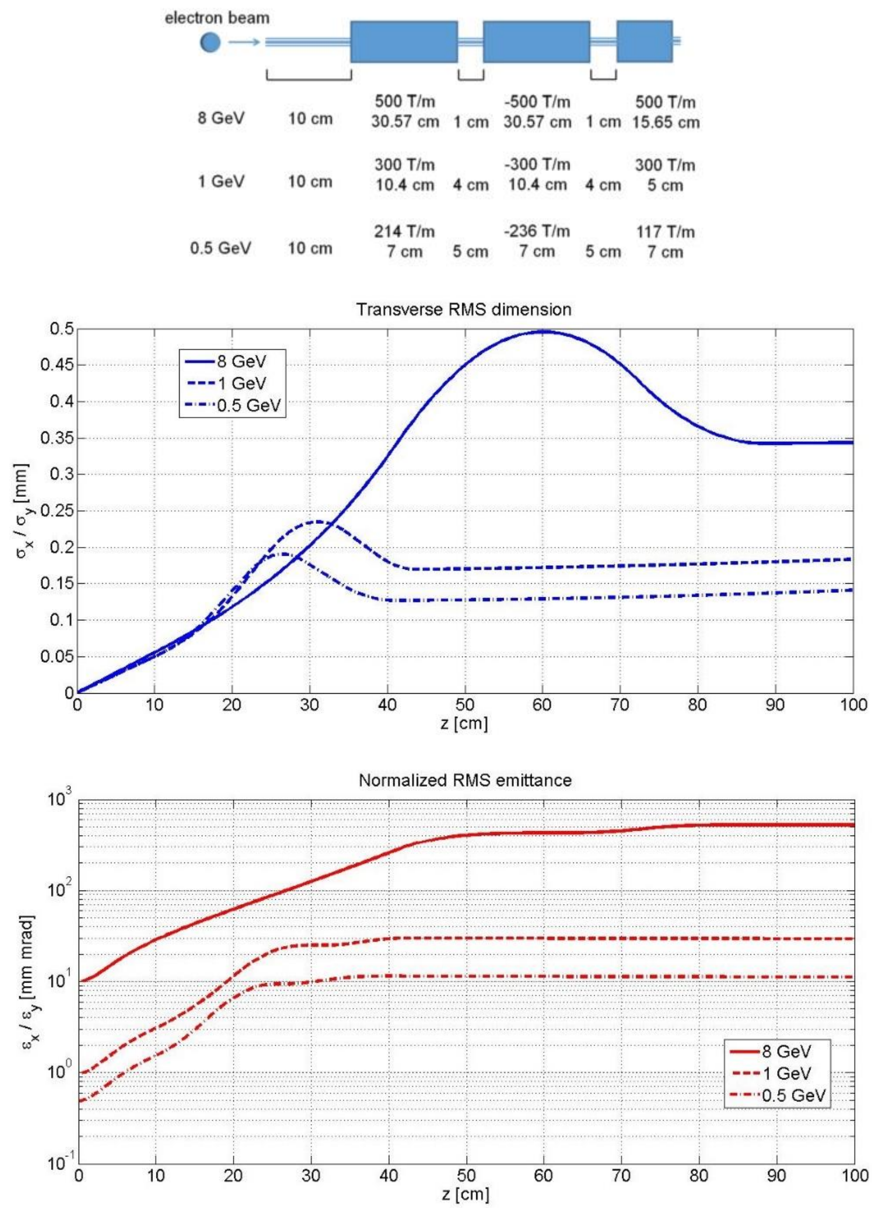

Fig. 12 – Comparison of triplet capture lines at different mean electron energies. Top plot: Transverse beam size (RMS) of the electron beam traveling through the triplet. Bottom plot: Normalized RMS emittance of the electron beam traveling through the triplet.

3.5 Capture and transport line of low energy (350 MeV), laser-accelerated electron beams

In this paragraph we analyze the possibility of capturing and transporting laser-generated electrons such as typically generated on commercially available hundred TW-range laser systems. We have used the same methodology described in the previous paragraphs dealing with high energy electron beams.
Decreasing the main energy of the electron beam leads to an easier and more efficient beam transport: the magnetic strength of the quadrupoles can be decreased and the growth of the normalized emittance along the transport line, even if still significant, is reduced. For these reasons, we were driven to investigate about the capability of a quadrupole-based beam line to capture and transport an electron beam with a reduced mean energy, with respect to the cases handled so far. Indeed, laser-accelerated electron beams can be routinely obtained with commercial laser systems with a power in the range of hundreds of TW. Such laser facilities are becoming more and more common also in medium-small research centers due to their reduced dimension and lesser costs, compared to PW-power laser systems.

For our analysis, we took as reference electrons with a mean energy of 350 MeV, generated when interacting with a supersonic gas jet. These beams are currently achieved with a very good reproducibility on state-of-the-art commercial laser systems and represent a benchmark for this laser-generated electron production. They can be obtained more routinely than what has been recently measured on higher power, more sophisticated laser systems (i.e. PW-class lasers). Typical parameters of the electron beams obtained by commercial laser systems are shown in Table II: in our case, we considered a laser with wavelength $\lambda_0 = 0.8$ µm, duration $\Delta\tau = 30$ fs (FWHM), and beam waist $\Delta\omega = 15$ µm (FWHM), delivering an intensity of $I = 1.2 \times 10^{19}\ W \cdot cm^{-2}$ onto a $n_e = 5.2 \times 10^{18}\ cm^{-3}$ dense, 4 mm long plasma channel produced by a supersonic Helium gas jet previously ionized, as described in Ref. [13]. The parameters that are not explicitly reported in Ref. [13] have been chosen based on reasonable values that could be found in other relevant, similar experiments. [14] [15] [16] [27]

Mean energy	350 MeV
Relative energy spread (rms)	8%
Bunch length (rms)	6 fs
Transverse spot-size (rms)	1 μm
Transverse divergence (rms)	5 mrad
Normalized emittance	3.4 mm mrad

TABLE II. Characteristics of the electron beam for low energy electrons as obtained on a hundred-TW laser system.

A comparison of the electron beam characteristics for the high (≥500 MeV) and low (350 MeV) electron energy distributions (Tables I and II) clearly shows that the critical parameter for such lower-energy beams, besides the large energy spread, is the divergence, which is about 10 times higher than the one shown in Table I.

3.5.1 Optimization of the triplet capture line with TRACE3D (350 MeV electron beam)

For the study concerning the low energy electron beam, generated by a TW-class laser, we used the same procedure as the previous cases of high energy, GeV-range beams. The beam line that captures the electron is made of a triplet of magnetic quadrupoles.
The physical parameters of the magnetic lenses obviously need to be adapted to the new initial conditions of the electron beam coming from the laser-plasma source. In order to obtain optimal values for the quadrupoles' length, magnetic field and spacing, we run several simulations with the beam dynamics code TRACE3D.
We managed to optimize the magnetic field gradient of the three quadrupoles by fixing their length at 5 cm and the spacing between them as reported in Fig. 13. The distance between the first quadrupole and the laser-plasma source is 9 cm. The initial electron beam parameters are those reported in Table II, in terms of the Twiss parameters they are:

$\alpha = 0$
$\beta = 2.0 \times 10^{-4}\ m$
$\varepsilon = 1.6 \times 10^{-3}\ mm\ mrad$

The matching algorithm has been run aiming to obtain a collimated beam at the exit of the capture line with $\alpha = 0$ (i.e. a collimated beam) and beta as small as possible. The simulations delivered optimal values of the quadrupole fields for a final value of $\beta = 200$ m, as reported in Fig. 13.

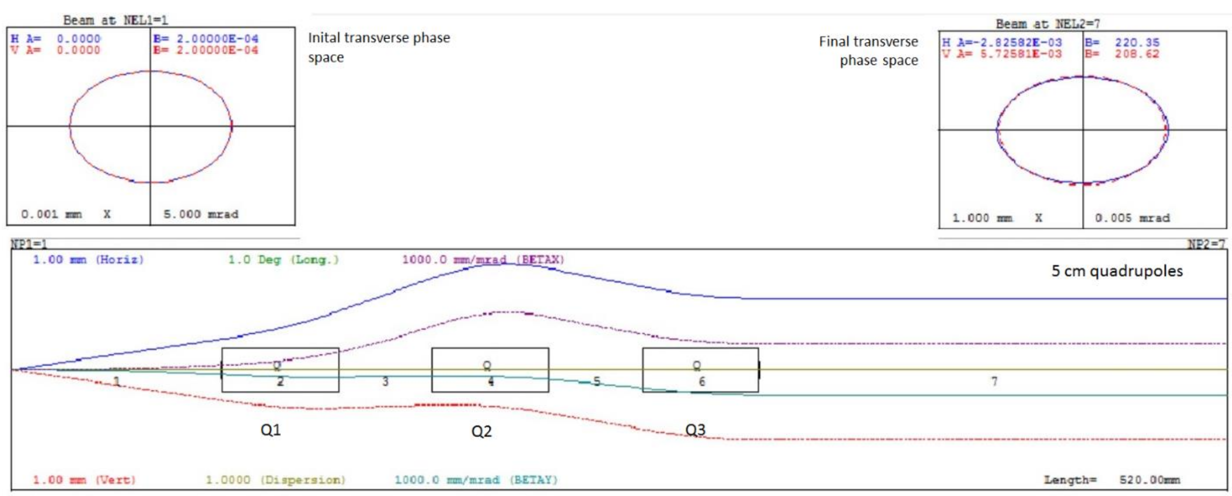

Fig. 13 – Electron beam transverse dimensions and divergence as obtained by the code TRACE3D. Top-left plot: phase space of the initial electron beam. Top-right plot: phase space of the final electron beam. Bottom plots: Transverse dimensions of the electron beam (blue and purple curve: x-dimension; red and green curve: y-dimension), as a function of the distance from the laser-plasma source (z=0).

Using three quadrupoles with a field gradient of Q1=254.9 T/m, Q2=-294.9 T/m and Q3=142.4 T/m respectively, the electron beam is collimated at the end of the triplet with a transverse dimension of less than 1 mm (top right plot of Fig. 13).

3.5.2 Analysis of the emittance growth in the triplet beam line with TSTEP

Although electrons travel at considerably lower energy (350 MeV), which makes the beam easier to control since it is possible to use less challenging magnetic fields in beam focusing devices (such as quadrupoles or solenoids), the detrimental effect of the large divergence is observed in the worsening of the normalized emittance—which scales with the fourth power of the divergence—even in a simple drift [10].
Using the same methodology as for the analysis of the high energy electron beams of the previous paragraphs, we used the particle tracking code TSTEP to investigate about the evolution of the normalized emittance along the quadrupole triplet.
This effect of emittance growth due to chromatic effects (same as the GeV range electron beam) is visible from the results obtained with TSTEP, reported in Fig. 14 (top scheme).
We simulated the beam line with the optimized parameters obtained from the optimization with TRACE3D. The electron beam has been modeled with a Kapchisky-Vladimirsky distribution, having the characteristics of Table II. In Fig. 14 we show the results of the particle tracking simulations where it is visible that the triplet lattice is able to keep the transverse beam dimensions under control along the whole path of the electrons (as foreseen by the TRACE3D simulation, as well). However, the emittance growth cannot be avoided as the value of epsilon increases, reaching 15 mm mrad at the exit of the triplet.
These results show that the quadrupole triplet is not able to transport the electron beam efficiently from the point of view of the normalized emittance, due to the strong chromatic effects of the quadrupoles on the electron bunch.
The initial parameters of the electron beam are too challenging for a simple quadrupole triplet. This first result shows that either a more complex transport line needs to be studied or the initial beam parameters have to be more relaxed.

Before going over to a different configuration of a transport line, involving additional focusing elements, we adopted a parametric approach in order to investigate acceptable initial beam parameters that can be handled by the triplet line. As discussed previously, the worsening of the normalized emittance of a laser-accelerated electron beam, traveling through a focusing beam line is due to the chromatic effects of the quadrupoles and due to the large beam divergence that contributes to the increase of the value indicated in Eq. 2.2. We ran additional simulations, keeping all the initial beam parameters unchanged (as considered so far) with the exception of the beam divergence and the beam energy spread. We simulated the same triplet beam line, i.e. with the same parameters for the quadrupole lenses and the same spacing between them, with different, decreasing values of initial beam divergence first, and energy spread afterwards.

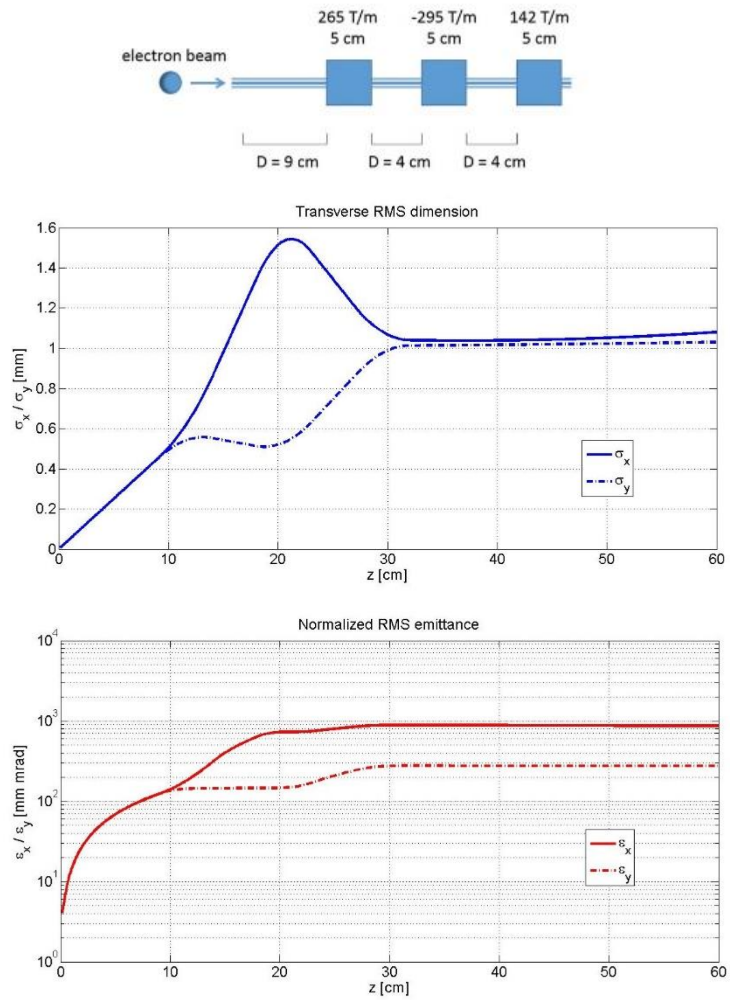

Fig. 14 - Results as obtained by the TSTEP simulations for a triplet capture line. Above the schematic of the triplet line. Top plot: transverse beam size (RMS) of the electron beam traveling through the triplet. Bottom plot: normalized RMS emittance of the electron beam traveling through the triplet.

In Fig. 15 we report the results of the parametric study performed with an electron beam of 350 MeV traveling in a triplet and having a fixed energy spread of 8 % and a variable divergence. We show the performance of the triplet lattice structure in terms of ability to keep the beam dimension under control, i.e. the beam transverse spot size as a function of the distance from the laser-plasma source, and the evolution of the normalized RMS emittance of the beam traveling through the transport line. We have obtained the data from a set of TSTEP simulations and we show the results concerning the beam transverse dimensions (blue curves) and normalized RMS emittance (red curves). Comparing the curves on the left and right side of the figure allows studying the sensitivity of the triplet to the variation of divergence and energy spread, respectively.

In the plots on the right side, we fixed the divergence at 5 mrad, corresponding to the worst case scenario among the ones we considered, and performed a parametric study as a function of the energy spread of the beam. The data show that the initial divergence of the electron beam has a significant effect on the efficiency of the beam transport, form the point of view of the normalized emittance. Lowering the initial divergence reduces the growth of the normalized emittance throughout the triplet lattice: even if the focusing fields are not different for the cases with a lower divergence, the electron beam enters the triplet line on a more collimated trajectory. Even if the focusing field of the quadrupoles has a weaker effect on the particles that are closer to the central axis, its strength is enough to transport the beam efficiently. From the curves (red) of the top plot it is evident that for an electron beam with a smaller divergence the chromatic effects of the quadrupoles have a minimized effect on the growth of the normalized emittance. For an electron beam with a divergence of 0.5 mrad the final value of the normalized emittance is <10 mm mrad, getting closer to what can be obtained on a conventional facility.

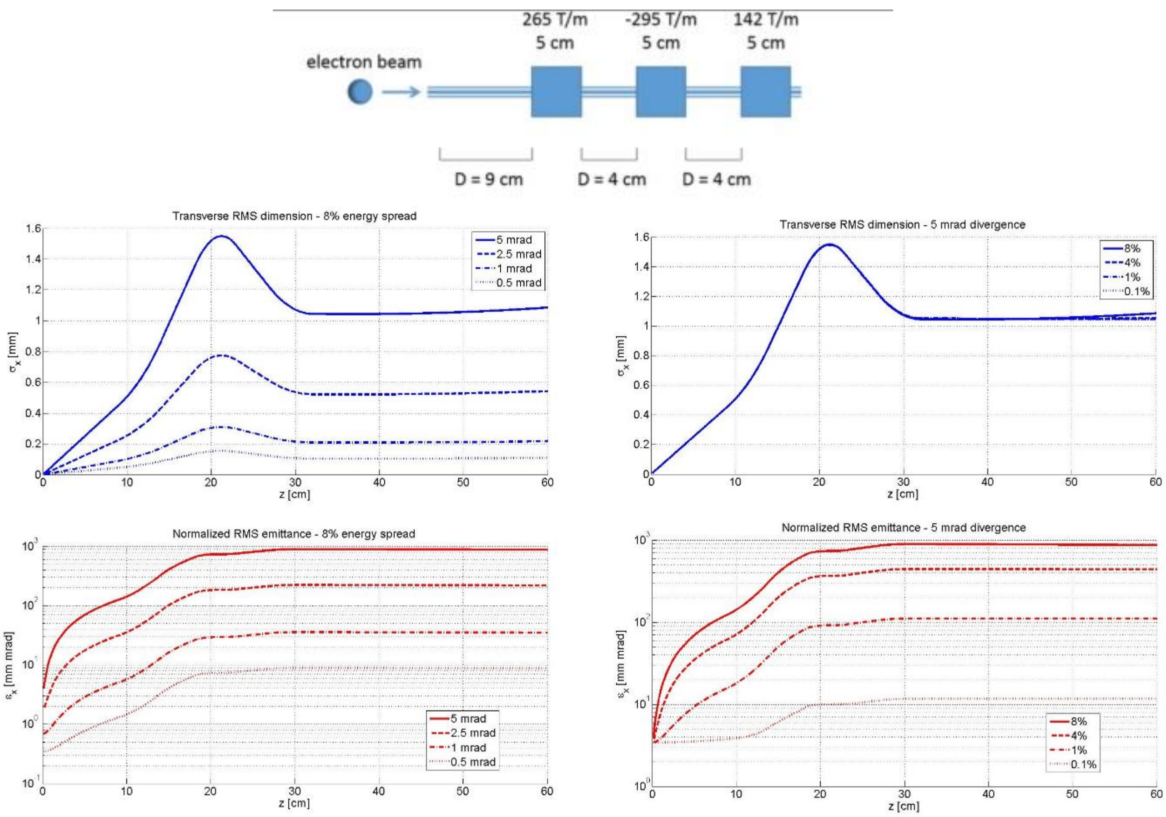

Fig. 15 – Triplet scheme with quadrupoles gradients and lengths (top). Left plots: Parametric study varying the divergence, the transverse size and the emittance, but keeping the energy spread fixed at 8 %. Right plots: Parametric study, varying the energy spread value, the size and the emittance of the beam, keeping the divergence fixed at 5 mrad.

Decreasing the energy spread of the electron beam, as reported in the right-hand side plots of Fig. 15, reduces the chromaticity caused by the focusing fields of the quadrupoles. In this case, reported by the bottom plots of Fig. 15, the improvement in terms of emittance growth is due to the fact that the quadrupoles of the triplet have been optimized for an energy of 350 MeV. If the energy spread is narrow, i.e. all the particles of the bunch have about the same energy, the focusing effect of the quadrupoles will be homogeneous on all the electrons and there won't be significant chromatic effects. In terms of the normalized emittance, this leads to a smaller final

value as the first term in the parenthesis of Eq. 15 of Appendix I, containing the energy spread of the beam, is less significant.
From Fig. 15, we see that the output parameters remain constant over a longer distance, which enables the use of a drift space after the end of the beam line without significantly worsening the beam parameters. These data show that in order to have beams with acceptable characteristics in terms of normalized emittance, the laser-plasma source should either produce beams with a small divergence and/or a low energy spread.

3.5.3 Analysis of a quadruplet lattice with TSTEP

After having analyzed the performances of the simple triplet, we investigated the possibility of adding additional focusing elements to the transport line in order to lower the final value of the normalized emittance.
Indeed, we have studied a transport line based on an array of four quadrupoles. The configuration is of the type double-FODO as shown in Fig. 16. The optimization has been done with the optics code TRACE3D. The fine tuning of the quadrupoles' parameters and the analysis of the emittance evolution have been performed with TSTEP, like in the previous studies.
The numerical results from the particle tracking simulations are reported in Fig. 16. It is visible that the quadruplet structure is able to capture the beam efficiently from the source and transport it over a length of about 60 cm, delivering a collimated beam. The transverse dimensions are kept under control, regardless of the initial beam conditions in terms of divergence and energy spread. However, with respect to the case of the simple triplet, the additional quadrupole does not allow avoiding the significant growth of the normalized emittance. As shown in Fig. 16, the normalized emittance at the exit of the capture line has a value of about 500 mm mrad for the real case scenario, i.e. with initial divergence and energy spread of 5 mrad and 8 % respectively. The parametric analysis shows that, similarly to the triplet, the transport process becomes more efficient only for improved parameters of the initial electron beam.

It is questionable if the additional cost of a fourth quadrupole is worth the moderate improvement of the beam line parameters. In any case, the two schemes for the low energy 350 MeV electron beam, described so far (with three and four quadrupoles) can easily be implemented in a beam line, since the quadrupole magnets' parameters are simple to manufacture, and they do not present any particular geometric constraint. Both schemes allow having a satisfactory capture line, operating at best performances for this kind of highly divergent beams with large energy spread (i.e., highly chromatic), in particular, when the goal is to keep the normalized emittance and beam size under control.

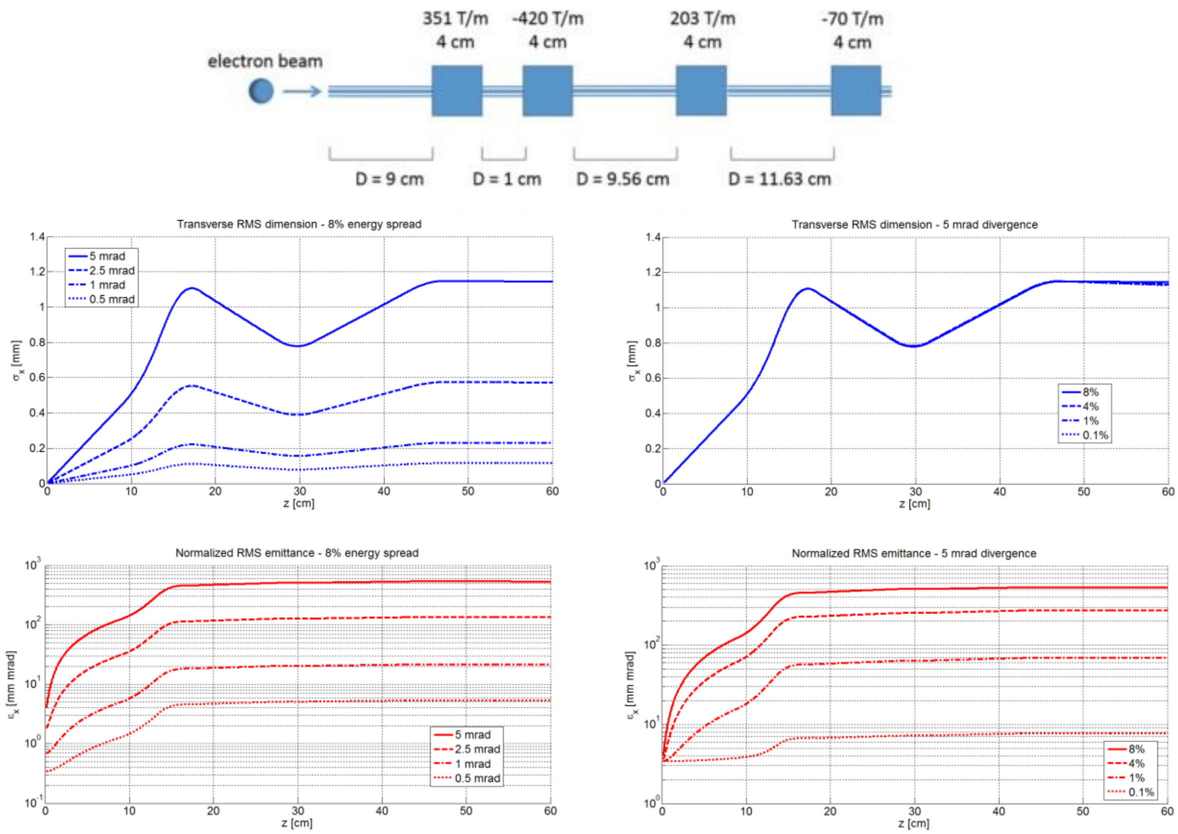

Fig. 16 - Quadruplet scheme with quadrupoles gradients and lengths (top). Left plots: Parametric study varying the divergence, the transverse size and the emittance, but keeping the energy spread fixed at 8 %. Right plots: Parametric study, varying the energy spread value, the size and the emittance of the beam, keeping the divergence fixed at 5 mrad.

3.5.4 Analysis of a symmetric double triplet lattice

The transport lines that we have analyzed so far are asymmetric, which means that they cannot reproduce at the exit of the lattice, the same initial beam parameters. In order to obtain the same beam features as at the electron source (i.e. the same transverse dimension, the same divergence etc.), it is necessary to perform the capture and the transport with a symmetric lattice.

This kind of transport lines can be used in particular for applications such as multi-staged, laser based acceleration systems [28] [29]. In a multi-staged system the electron beam travels through multiple laser-plasma accelerating structures after being generated at the laser-plasma source. When the electron beam is injected into the post-acceleration plasma channel, the transverse dimensions need to be matched to the plasma wavelength of the second stage (i.e. the stage after the laser-plasma source). Typically transverse dimensions in the order of magnitude of a few μm are required (see Ref. [29]). Therefore, the electron beam needs to transported from one laser-plasma stage to the next, having at the entrance of each stage the same initial beam parameters. Matching the electron beam from one stage to the other can be done, in principle, with a symmetric transport line.

The double triplet solution shown in Fig. 17 (scheme above the plots), typically used in conventional accelerators, provides, with a minimum number of magnetic elements, acceptable performances in terms of normalized emittance (reaching a value <10 mm mrad, although this depends on the initial conditions). In order to reproduce the initial parameters of the beam after a given distance, a symmetrical transport line is required in which a fixed sequence of conventional elements is used at the beginning of the beam line and then again repeated at its end.

A first line that we have designed for this purpose uses a symmetrical and optimized double triplet of quadrupoles, in order to have at its exit a Twiss α function equal to zero (same as in input). Being the transport line symmetric, the condition on Twiss α is sufficient to obtain a final value of Twiss β equal to the initial one (it is not required to set a constraint on Twiss β, as for the previous cases of asymmetric beam lines). We studied the required geometrical features and magnetic field intensity of the elements of the beam line with the charged particle optics solver MAD-X, [19] which has more efficient algorithms for the optimization of more complex beam line structures, compared to TRACE3D. In Fig. 17 we report the behavior of the double-triplet line optimized with MAD-X, in terms of the Twiss parameters α and β. From the black and red curves it is visible that the initial conditions are restored in terms of the β function. The algorithm calculates the optimal values of the quadrupoles' focusing field as

Q1 = -95 T/m
Q2 = 142 T/m
Q3 = -233 T/m

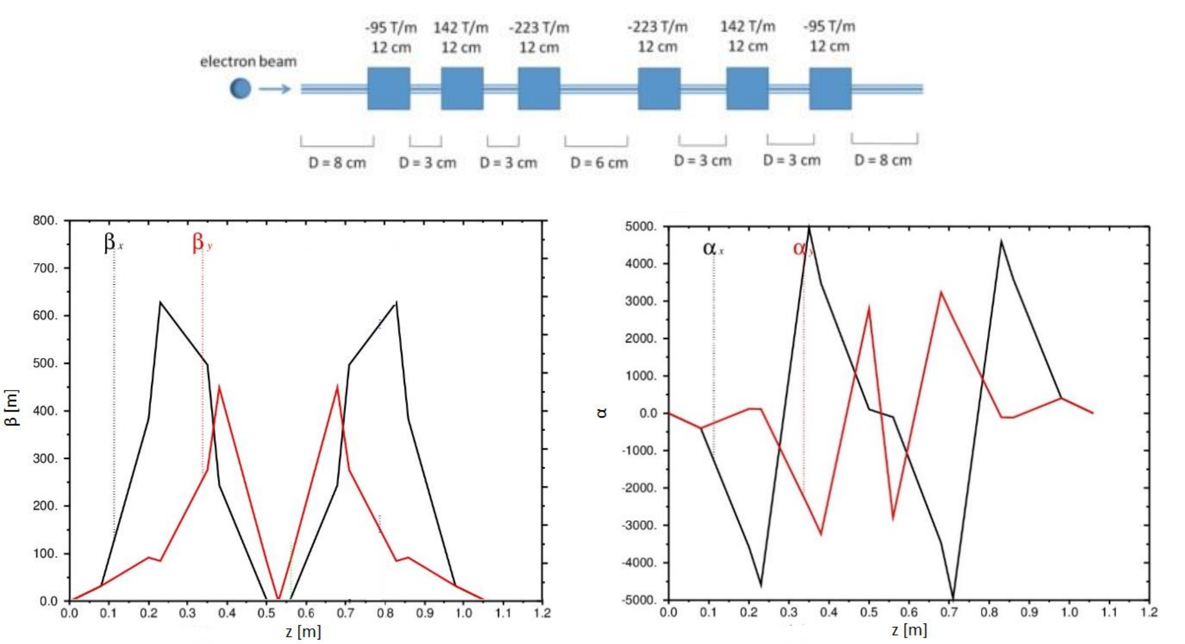

Fig. 17 - Electron beam transverse dimensions and divergence as obtained by the code MAD-X, for a beam traveling through the double-triplet line. Left plot: β-function of the electron beam (i.e. the transverse dimension) traveling through the double-triplet line. Right plot: α-function of the electron beam (i.e. the divergence) traveling through the double triplet line.

We checked the quality of the beam transport with the particle-tracking code TSTEP, using the spacing that has been simulated with MAD-X and the optimized values of the quadrupoles. By doing so, it is possible to investigate the evolution of the normalized emittance and the chromatic effects of the quadrupoles: similarly to TRACE3D, the optical code MAD-X does not take a realistic particle distribution into account but only calculates the values of the Twiss parameters with the transport matrix formalism.

Fig. 18 shows the emittance and transverse beam size for different values of energy spread and beam divergence, as calculated with TSTEP. From the plotted curves, we see that, using a double triplet configuration, it is possible to transport the electron beam from the source to the delivery point, but the initial transverse dimension remains unchanged only for low energy spread values (<1 %). As shown in Fig. 18, the symmetry of the beam parameters deteriorates with increasing energy spread. However, no beam chromaticity control is possible with such a double triplet line. The large energy spread of the beam causes chromaticity to play an important role on the beam quality. The only possibility to reproduce the incoming beam characteristics at the beam line exit and, at the same time, preserving the low normalized emittance, is using additional magnetic elements that can correct the chromatic effects. Achromatic transport lines require the use of sextupoles (which correct linear chromaticity), dipoles (which create dispersion), and higher order multipolar devices.

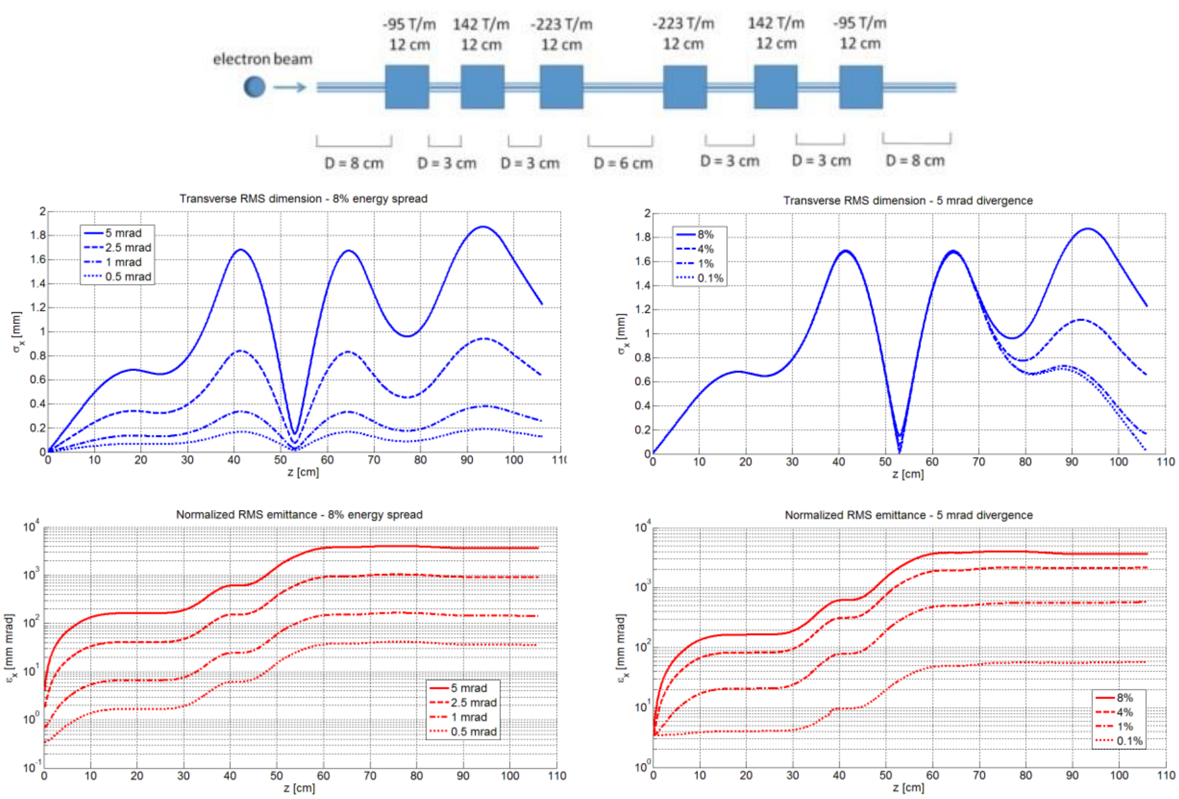

Fig. 18 – Double-triplet scheme with quadrupoles gradients and lengths (top). Left plots: Parametric study varying the divergence, the transverse size and the emittance, but keeping the energy spread fixed at 8 %. Right plots: Parametric study, varying the energy spread value, the size and the emittance of the beam, keeping the divergence fixed at 5 mrad.

3.5.5 Analysis of an achromatic lattice structure

An achromatic beam line scheme for laser accelerated electrons has already been proposed and it's capability to transport the beam demonstrated in previous studies. [29] Despite a broad energy spectrum and a large beam divergence, an achromatic line appears to be a viable solution for the capture and transport of laser-accelerated electron beams: theoretical results have demonstrated how the chromaticity and the large beam divergence can be compensated by the transport line, for a given set of initial beam parameters.
However, the mean energy that has been considered in Ref. [29] for the design of a transport line is 50 MeV and therefore not in the energy range of the laser driven electron source that we are considering here.

A possible achromatic beam line structure has been simulated with MAD-X uses two 2 T dipoles and four sextupoles. MAD-X has similar features to TRACE3D but it provides a more efficient matching algorithm for optimizing the beam line elements. We used this code for this kind of more complex lattice, as the optimization can been done in two steps (i.e. two consecutive matching routines have been run within the same simulation).
Initially, we optimized the transport line by calculating the values for the quadrupoles of the line in such a way that the initial beam parameters are restored at the end of the lattice. The central quadrupoles have been designed in order to compensate the dispersion introduced by the dipoles. Initial and final quadrupoles are used to focus the beam and to keep the Twiss β function under control. The result of the first optimization is reported in Fig. 19, where the symmetric lattice shows to be capable to transport the 350 MeV electron beam efficiently, restoring the initial transverse parameters of the beam.
Furthermore, we used MAD-X to optimize the parameters of the two magnetic dipoles and the four sextupoles. We run the optimization algorithm again, setting a value for the energy spread different from zero, aiming to obtain the optimal values for the magnetic field of the dipoles and the sextupoles. We set as constraint to obtain at the end of the achromatic line the same values for Twiss beta as the initial ones. The energy spread of the beam triggers the chromatic effects of the quadrupoles and the matching routine of MAD-X aims to correct them by calculating the optimal values of the dipoles' and sextupoles' magnetic field.
The dipoles introduce a dispersion and a correlation between position and energy of the chromatic beam. The sextupoles, acting on the dispersion introduced by the dipoles, correct the linear chromatic effect, and thus we expect the normalized emittance worsening to be partially compensated. As visible in Fig. 20, the achromatic line calculated with MAD-X has a quasi-symmetric behavior for low values of energy spread (in the figure's case, it is about 1%).
The fields of these dipoles, although quite high, could be manufactured using electromagnets enhanced with permanent magnet materials.

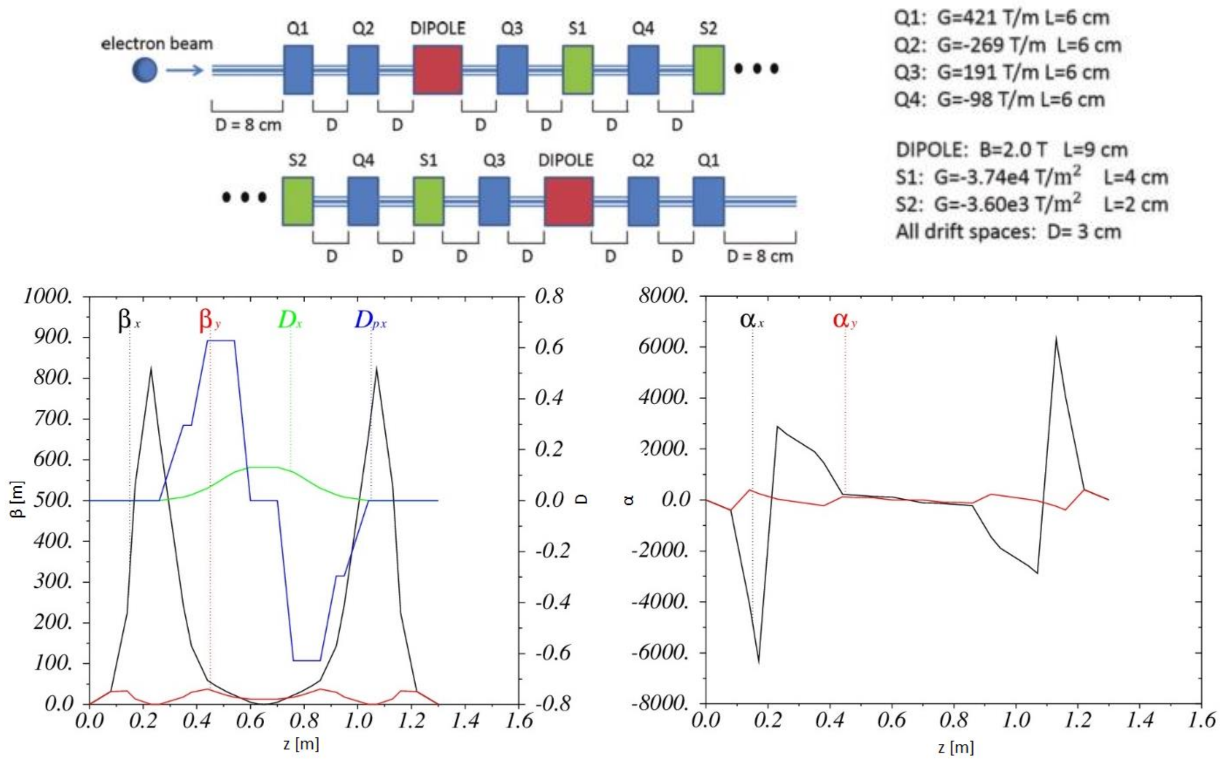

Fig. 19 - Electron beam transverse dimensions and divergence as obtained by the code MAD-X, for the case of an electron beam with energy 350 MeV and no energy spread, traveling through the achromatic line. Left plot: Dispersion function and β-function of the electron beam (i.e. the transverse dimension) traveling through the double-triplet line. Right plot: α-function of the electron beam (i.e. the divergence) traveling through the double triplet line.

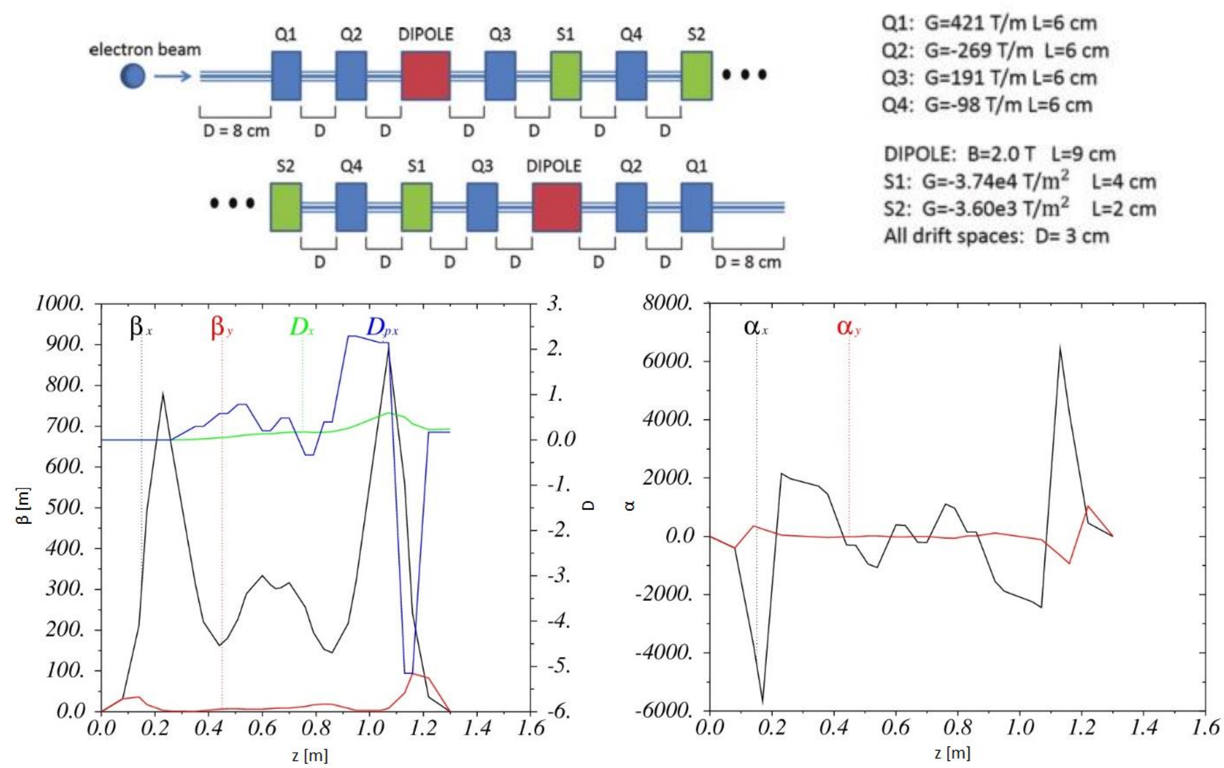

Fig. 20 - Electron beam transverse dimensions and divergence as obtained by the code MAD-X, for the case of an electron beam with energy 350 MeV and an energy spread of ~1 %, traveling through the achromatic line. Left plot: β-function of the electron beam (i.e. the transverse dimension) traveling through the double-triplet line. Right plot: α-function of the electron beam (i.e. the divergence) traveling through the double triplet line.

We simulated the studied transport line with the code TSTEP, in order to analyse the dynamics of the beam with its particle distribution. We wanted to verify that the behavior that we had obtained with MAD-X using an ideal beam distribution, is confirmed by the particle tracking code. Moreover, we were able to check the evolution of the normalized emittance along the transport line, taking into account a realistic particle distribution.

The results of the achromatic beam transport, calculated with TSTEP, are shown in Fig. 21. We considered, as before, two options: (1) we varied the beam divergence keeping a constant energy spread of 8% (left plots), and (2) we varied the energy spread keeping a constant beam divergence of 5 mrad (right plots). Even using this achromatic structure, when having at the laser-plasma source a 1 mrad divergence, an energy spread over 1 % leads to a detrimental growth in beam emittance and size. This is due to the fact that the high energy-spread generates highly non linear terms in the dispersion function of the beam: a large σ_ε (energy spread) and a small β make the system highly non linear. When increasing the energy spread, the beam line becomes less achromatic, because second and higher order terms in the chromatic function play a more significant role. Multipole elements, such as octupoles or higher order focusing and steering elements, would be necessary to correct the higher order terms in addition to the linear corrections provided by the sextupoles.

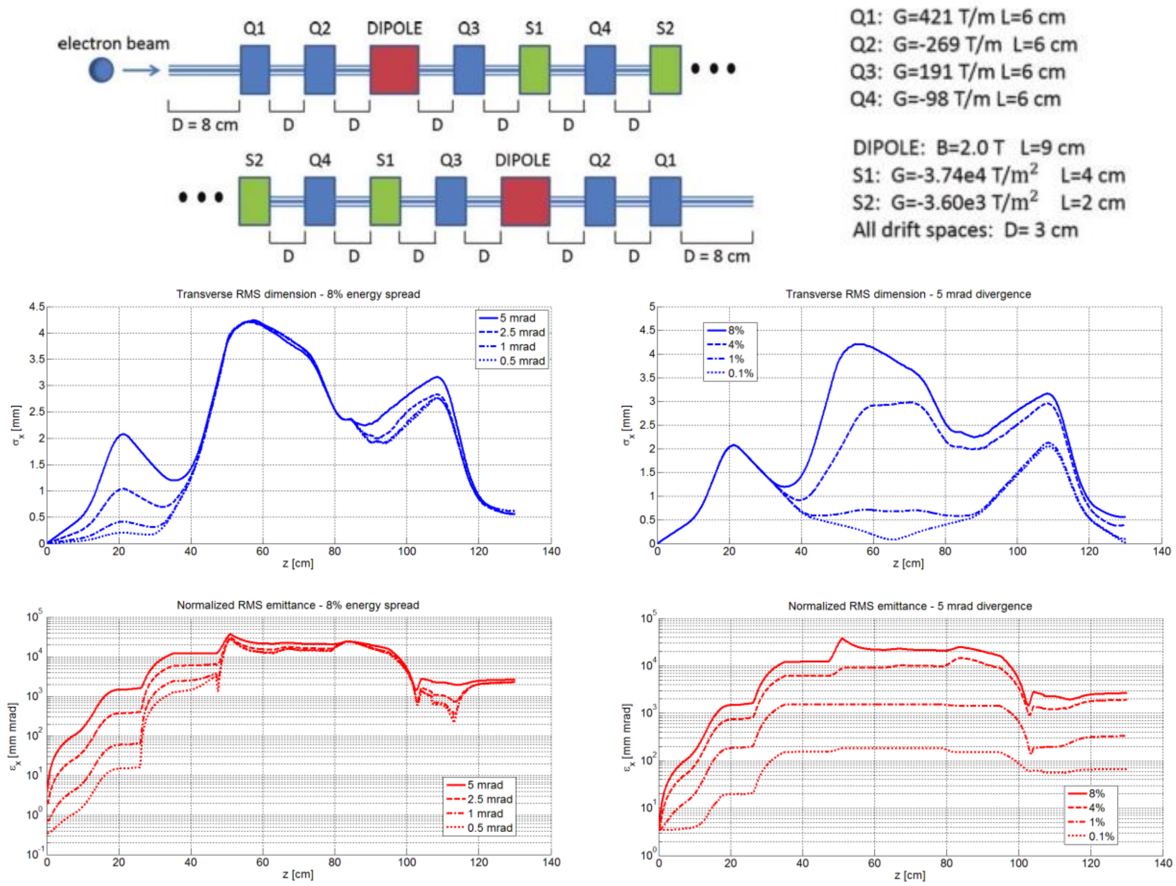

Fig. 21 – Achromatic beam line optimized for 350 MeV electrons, with a divergence of 5 mrad, transverse size 1 µm and 8 % energy spread. Left plots: parametric study of the transverse size and emittance evolution for an electron beam with an energy spread of 8 % and different beam divergences. Right plots: parametric study of the transverse size and emittance evolution of an electron beam with a divergence of 5 mrad, this for different energy spread values.

3.5.6 Parametric analysis of the best working point for the triplet lattice structure

The analysis of different transport line configurations discussed so far led us to the following conclusions: I) in terms of the evolution of the normalized emittance, only electron beams with initial values of beam divergence and energy spread below a certain threshold can be transported efficiently; II) the implementation of more complex transport lines, compared to the simple triplet structure, does not lead to a significant improvement of the final value of the normalized emittance (not even with an achromatic lattice).

The parametric studies that we have performed show clearly that a simple transport line such as a quadrupole triplet is more suited to capture and transport the 350 MeV electron beam, compared to the other possible configurations investigated so far.

For these reasons, we decided to study more into detail the performance of the triplet lattice, aiming to establish acceptable working point for the laser-based accelerator. The methodology that we adopted is to run particle tracking simulations of the triplet lattice discussed in

Paragraphs 3.5.1 and 3.5.2, using all the different possible combinations of initial beam divergence and energy spread, ranging from 0.5 to 5 mrad and 0.1 and 8%, respectively. The aim was to indicate the final value of normalized emittance that is obtainable with different combinations of initial beam parameters, in order to obtain threshold values for an efficient beam transport.

In Fig. 22, we show the normalized emittance values at the end of the triplet line for different possible combinations of beam divergence and energy spread at the source. We focused on the beam emittance, since this is a key performance parameter for many applications, in particular, when it comes to having a high peak brilliance. The normalized emittance is an important indicator of the beam quality in the case of FEL applications, where conventional RF accelerators provide high-quality driving electron beams with low transverse emittance. Moreover, compared to other possible applications of laser-accelerated electron beams that require even more challenging beam parameters at the exit of the transport line (e.g. electron colliders), for FEL applications the comparison between conventional accelerators and laser-plasma driven beam lines is at reach and of actuality.

The data reported in Fig. 22 have been obtained by interpolating the numerical results from simulations with different initial beam parameters. We calculated the final value of normalized emittance with TSTEP by varying the initial beam divergence and energy spread of the input distribution. All other parameters were kept unchanged and the particle distribution is a Kapchinsky-Vladimirsky distribution for all simulations. The final values of normalized emittance have been interpolated numerically (with the data processing code MATLAB) and we were able to obtain the surface given by the values of the emittance as a function of two variables, i.e. initial beam divergence and energy spread.

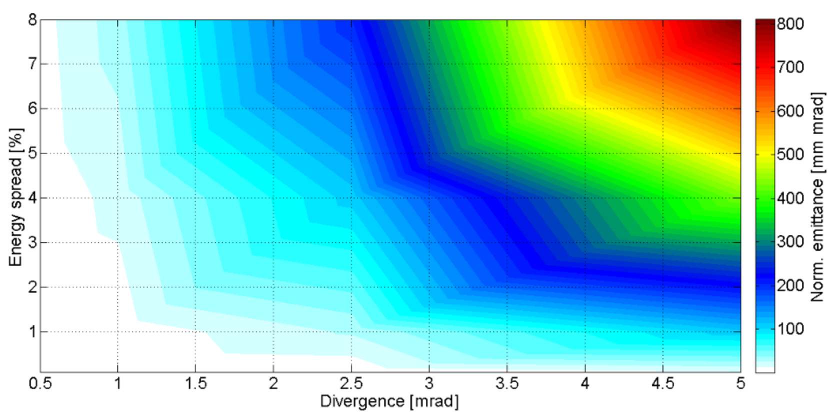

Fig. 22 – Normalized emittance values (color-scale) of the final electron beam, at the exit of the triplet lattice, as a function of initial beam divergence and energy spread.

In Fig. 23 these numerical data have been analyzed in order to show the different ranges, indicated by the colored areas, of the final normalized emittance as can be obtained from the given initial beam parameters (on the x and y axis). For instance, in order to obtain a final value

of less than 1 mm mrad after the transport throughout the triplet, the required initial beam features are indicated by the blue area.
These data indicate the set of required parameters for the laser-driven electron source (emittance and divergence) in order to be close to an emittance value of ~1 mm mrad after the transport. The only way to produce a laser-generated electron beam that is comparable with those obtained on conventional accelerators mentioned above, even when coupling it to a transport line, is to reduce the energy spread and beam divergence below a certain threshold value. For the capture of a 350 MeV electron beam, as considered here, this threshold value can be estimated to be about 1 mrad and 1 %, for, respectively, beam divergence and energy spread, in order to obtain a final value of normalized emittance that is comparable to the one of conventional accelerators.

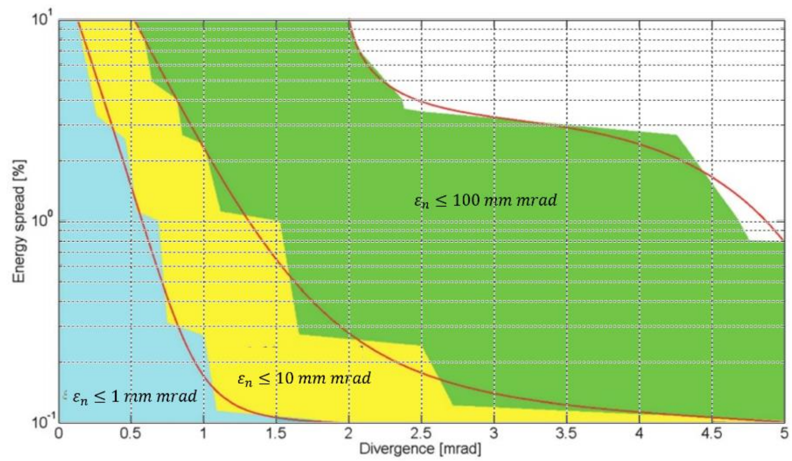

Fig. 23 – Values of transverse normalized emittance at the end of the triplet line, for different combinations of divergence and energy spread at the laser-plasma source. The blue area indicates electron beams that have a normalized emittance up to ≤1 mm mrad at the exit of the transport line (≤10 mm mrad for the yellow area and ≤100 mm mrad for the green area). The red curves are guides for the eye.

3.6 Conclusions

In this study, we have performed a parametric study of transport lines for electron beams generated by laser-plasma interaction, considering laser-generated electron energies ranging from 350MeV to 8 GeV. We have tested different beam transport systems in order to study and analyze the emittance growth issue for laser-generated electron beams. Taking into account the limits of current technology, we show that a transport line based on conventional magnetic elements is not able to transport electron beams typically generated on laser-plasma experiments, preserving its initial emittance. To overcome this issue, the laser-plasma electron source needs to have energy spread and divergence that lay within a certain parameters space (for the case of laser-generated electrons in the 350 MeV range these boundaries are about 1 mrad for the divergence and 1% for the energy spread).

We tested various transport line schemes, from a simple triplet structure to a more complex achromatic lattice structure. The achromatic line is more difficult to manufacture, in particular, for the extremely intense magnetic field of the dipoles and the high gradients of the quadrupoles, which are both at the limit of nowadays technology. However, even despite its longer dimension and higher complexity, this lattice structure is not able to handle the electron beam transport when these beams have a high energy spread and divergence (i.e., the values are outside the acceptable parameter space). The same conclusion is valid for the symmetric line (consisting in a sequence of six quadrupoles) that cannot avoid beam degradation due to emittance growth. In case of high values for energy spread and divergence at the source, i.e., $\geq$1 % and $\geq$1 mrad, respectively, a transport line with high-order, multi-polar magnetic elements (i.e., octupoles and higher) may be the only solution for correcting the chromatic effects and avoiding the uncontrolled emittance growth.

On the other hand, if at the laser-plasma source it is possible to keep energy spread and divergence below a certain threshold value, the electron beam can be transported efficiently, even using only quadrupoles. However, using a simple triplet structure (or four quadrupoles), it is not possible to keep the chromatic effects under control. In the case of lower values for energy spread and divergence at the source, the triplet line appears to deliver better performances than the more complex (and longer) achromatic and symmetric lattices, even if the structure with three quadrupoles cannot reproduce the bunch initial conditions, as needed, for example, in a multi-staged system. By increasing the quality of the beam at the electron source significantly, the triplet line, despite its simplicity, is capable of transporting the beam efficiently. The electron beam needs to have a low divergence ($\geq$1 mrad) and low energy spread ($\geq$1 %) when it exits the laser-plasma source. Such improved beam parameters can be considered as a goal to achieve in the future, in order to develop electron beam lines accelerated by laser-plasma interaction.

By considering the results of the presented study, we can conclude that there could be two distinct, but complementary paths leading to an efficient beam transport considering the growth of the normalized emittance: (1) a significant improvement of the beam parameters at the laser-plasma source, in terms of energy spread and beam divergence; (2) using a transport line with magnetic elements that allow correcting high-order chromatic effects, i.e., octupoles and higher order multipoles.

References

[1] E. Allaria, C. Callegari, D. Cocco, W. M. Fawley, M. Kiskinova, C. Masciovecchio and F. Parmigiani, *New J. Phys.,* vol. 12, p. 075002, 2010.

[2] "SwissFEL Conceptual Design Report," *PSI Bericht,* Vols. 10-04, 2010.

[3] D. Einfeld, S. S. Hasnain, Z. Sayers, H. Schopper and H. Winick, *Radiat. Phys. Chem.,* vol. 71, pp. 693-700, 2004.

[4] F. Grüner, S. Becker, U. Schramm, T. Eichner, M. Fuchs, R. Weingartner and S. Reiche, *App. Phys. B: Laser and Optics,* vol. 86, pp. 431-435, 2007.

[5] A. R. Meier, A. Meseck, S. Reiche, C. B. Schroeder, T. Seggebrock and F. Gruener, *Phys. Rev. X,* vol. 2, pp. 1-7, 2012.

[6] H. -P. Schlenvoigt, K. Haupt, A. Debus, F. Budde, O. Jaeckel, S. Pfotenhauer, H. Schwoerer, E. Rohwer, J. G. Gallacher, E. Brunett, R. P. Shanks, S. M. Wiggins and D. A. Jaroszynski, *Nature Physics,* vol. 4, pp. 130-133, 2008.

[7] S. Di Mitri and M. Cornacchia, *Phys. Rep.,* vol. 539, p. 1–48, (2014).

[8] L. Giannessi, A. Bacci, M. Bellaveglia, F. Briquez, M. Castellano, E. Chiadroni, A. Cianchi, F. Ciocci, M. E. Couprie, L. Cultrera, G. Dattoli, D. Filippetto, M. D. Franco, G. D. Pirro, M. Ferrario, L. Ficcadenti, F. Frassetto, A. Gallo, G. Gatti, M. Labat, G. Marcus, M. Moreno, A. Mostacci, E. Pace, A. Petralia, V. Petrillo, L. Poleto, M. Quattromini, J. V. Rau, C. Ronsivalle, J. Rosenzweig, A. R. Rossi, V. Rossi, E. Sabia, M. Serluca, S. Spampinati, I. Spassovsky, B. Spataro, V. Surrenti, C. Vaccarezza and C. Vicario, *Phys. Rev. Lett.,* vol. 106, p. 144801, 2011.

[9] P. Antici, A. Bacci, C. Benedetti, E. Chiadroni, M. Ferrario, A. R. Rossi, L. Lancia, M. Migliorati, A. Mostacci, L. Palumbo and L. Serafini, *J. Appl. Phys.,* vol. 112, p. 044902, 2012.

[10] M. Migliorati, A. Bacci, C. Benedetti, E. Chiadroni, M. Ferrario, A. Mostacci, L. Palumbo, A. R. Rossi, L. Serafini and P. Antici, *Phys. Rev. Spec. Top. - Accel. Beams,* vol. 16, p. 011302, 2013.

[11] W. P. Leemans, A. J. Gonsalves, H. S. Mao, K. Nakamura, C. Benedetti, C. B. Schroeder, C. Tóth, J. Daniels, D. E. Mittelberger, S. S. Bulanov, L. Vay, C. G. R. Geddes and E. Esarey, *Phys. Rev. Lett. 113,* p. 245002, 2014.

[12] N. V. Zamfir, *Eur. Phys. J.: Spec. Top.,* vol. 223, p. 1221–1227, 2014.

[13] S. Fourmaux, K. T. Phuoc, P. Lassonde, S. Corde, G. Lebrun, V. Malka, A. Rousse and J. C. Kieffer, *Appl. Phys. Lett.,* vol. 101, p. 111106, 2012.

[14] M. Z. Mo, A. Ali, S. Fourmaux, P. Lassonde and J. C. Kieffer, *Appl. Phys. Lett.,* vol. 100, p. 074101, 2012.

[15] C. E. Clayton, J. E. Ralph, F. Albert, R. A. Fonseca, S. H. Glenzer, C. Joshi, W. Lu, K. A. Marsh, S. F. Martins, W. B. Mori, A. Pak, F. S. Tsung, B. B. Pollock, J. S. Ross, L. O. Silva and D. H. Froula, *Phys. Rev. Lett.,* vol. 105, p. 105003, 2010.

[16] D. H. Froula, C. E. Clayton, T. Doeppner, K. A. Marsh, C. P. J. Barty, L. Divol, R. A. Fonseca, S. H. Glenzer, C. Joshi, W. Lu, S. F. Martins, P. Michel, W. B. Mori, J. P. Palastro, B. B. Pollock, A. Pak, J. E. Ralph, J. S. Ross, C. W. Siders, L. O. Silva and T. Wang, *Phys. Rev. Lett.,* vol. 103, p. 215006, 2009.

[17] K. Floettmann, *Phys. Rev. Spec. Top. - Accel. Beams,* vol. 6, p. 034202, 2003.

[18] K. R. Crandall and D. P. Rusthoi, *Los Alamos National Laboratory Report LA-UR-97-886,* 1997.

[19] H. Grote and F. Schmid, *Proceedings of PAC03 (Portland),* pp. 3497-3499, 2003.

[20] L. M. Young, *Los Alamos National Laboratory Report LA-UR-96-1835,* 1996.

[21] A. Pukhov and J. Meyer-ter-Vehn, *Appl. Phys. B,* vol. 74, p. 355, 2002.

[22] V. Malka, J. Faure, Y. Glinec, A. Pukhov and J.-P. Rousseau, *Phys. Plasmas,* vol. 12, p. 056702, 2005.

[23] J. Faure, C. Rechatin, A. Norlin, A. Lifschitz, Y. Glinec and V. Malka, *Nature,* no. 444, pp. 737-739, 2006.

[24] T. Eichner, F. Gruener, S. Becker, M. Fuchs, D. Habs, R. Weingartner, U. Schramm, H. Backe, P. Kunz and W. Lauth, *Phys. Rev. Spec. Top. - Accel. Beams,* vol. 10, p. 082401, 2007.

[25] *Deliverable report of the WP6-CRISP-FP7 Project, Contract No. 283745, as private communication with L. Silva and coworkers (2014).*

[26] "Deliverable report of the WP6-CRISP-FP7 Project, Contract No. 283745, as private communication with L. Silva and coworkers," 2014.

[27] S. Kneip, S. R. Nagel, S. F. Martins, S. P. D. Mangles, C. Bellei, O. Chekhlov, R. J. Clarke, N. Delerue, E. J. Divall, G. Doucas, K. Ertel, F. Fiuza, R. Fonseca, P. Foster, S. J. Hawkes, C. J. Hooker, K. Krushelnick, W. B. Mori, C. A. J. Palmer, K. Ta Phuoc, P. Rajeev, J. Schreiber, M. J. V. Streeter, D. Urner, J. Vieira, L. O. Silva and Z. Najmudin, *Phys. Rev. Lett.,* vol. 103, p. 035002, 2009.

[28] B. B. Pollock, C. E. Clayton, J. E. Ralph, F. Albert, A. Davidson, L. Divol, C. Filip, S. H. Glenzer, K. Herpoldt, W. Lu, K. A. Marsh, J. Meinecke, W. B. Mori, A. Pak, T. C. Rensink, J. S. Ross, J. Shaw, G. R. Tynan, C. Joshi and D. H. Froula, *Phys. Rev. Lett.,* vol. 107, p. 045001, 2011.

[29] A. Chancé, O. Delferrière, J. Schwindling, C. Bruni, N. Delerue, A. Specka and P., *Nucl. Instrum. Methods Phys. Res. A,* vol. 740, pp. 158-164, 2014.

[30] J. Nielsen, Elements of modern X-ray physics, John Wiley, 2011.

[31] *FERMI @ Elettra Conceptual Design Report, Trieste,* 2007.

[32] V. Malka, J. Faure, Y. A. Gaudel, E. Lefebvre, A. Rousse and K. T. Phuoc, *Nat. Phys.,* vol. 4, pp. 447-453, 2008.

4. Analysis of a laser-driven proton beam line

4.1. Introduction

Since more than a decade, intense research is being conducted on laser-driven ion acceleration mechanisms, both theoretically and experimentally. Since the first experiments of laser-driven proton acceleration, performed in the 70s-80s [1], the energy of proton beams accelerated with high-power lasers has reached the order of magnitude of tens of MeV [2] [3] [4] [5]. Their features are shown to be complimentary, in some cases even preferable, to those of conventional accelerators, such as short bunch duration (< ps) and high charge (up to 10^{13} particles) [6] [7]. Therefore, many innovative applications including ultra-fast radiography [8] and isochoric heating (Warm dense matter) [9] [10] [11] are becoming possible with the use of laser-driven proton beams.

The maximum energy and the particle flux of laser-driven ion beams are limited by the energy of the laser pulse that drives the acceleration process. [12] In order to fulfill the requirements of higher flux and higher ion energy, industry and applied science laser centers are commercializing and designing more and more laser systems going towards higher repetition rate and higher energies: today, many commercial table-top laser systems in the hundreds of TW regime and even up to PW, deliver energies of up to a few J (even a few tens of J for the PW systems) in 15-30 fs with a repetition rate of up to 10 Hz. Many facilities have been built and/or commissioned in the last decade, such as ALLS (see Fig. 1) [13] at INRS (Canada), FLAME [14] at INFN-Frascati (Italy), CLPU [15] in Salamanca (Spain), Draco [3] at FZD in Munich (Germany) and the PW power facilities of the Extreme Light Infrastructure (ELI) [16]. The energy range that they typically cover is up to 10-20 MeV for the TW-class laser systems and even up to 50 MeV in case of PW laser facilities [2] [9] [12] [17] [18].

In fact, even higher energies than a few tens of MeV have been achieved, but for those cases reproducibility and shot-to-shot fluctuations have been a serious issue.

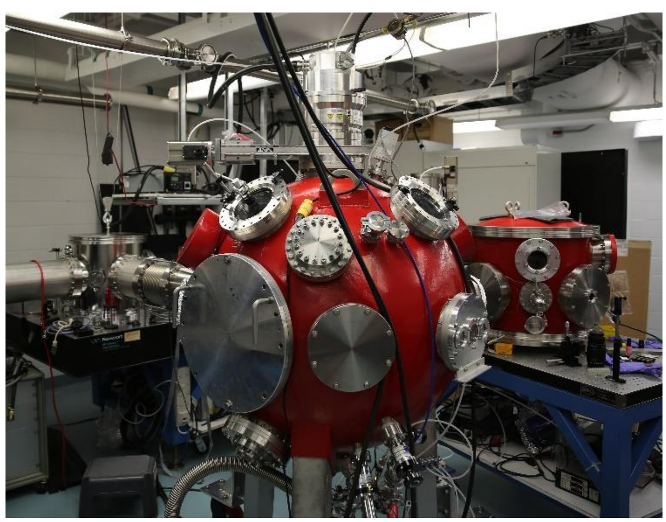

Fig. 6 – Vacuum target chamber at the ALLS facility (INRS, Canada) used for laser-acceleration of proton beams.

Differently from novel, upcoming PW-class lasers, TW-class laser work with higher repetition rate (up to tens of Hz) and provide more stable and reproducible beams.
When using laser systems with hundreds of TW power, the dominating acceleration mechanism is the Target Normal Sheath Acceleration (TNSA) where the routinely obtained proton beams achieve a maximum energy of a few tens of MeV (the details of this acceleration mechanism will be discussed in the following paragraph). [19] [20]
However, the energy spread, which can be as high as 100 %, is one of the main issues that precludes TNSA-generated proton beams from being used for various applications, such as those in the medical field.

Even though novel acceleration mechanisms are being explored, such as the shock-wave acceleration regime [21] or the Break- Out-Afterburner (BOA) [22], that can provide better beam parameters both in quality (energy spread and beam intrinsic divergence) and maximum energy, the combination with conventional beam-manipulation devices still seems to be inevitable [23] [24], as these mechanisms often require laser systems that are not comparable with commercial ones and have low repetition rates that would not allow applications where a high proton flux is necessary. Furthermore, special target engineering [4] [25], e.g. nano-structuring of the target surface (see Fig. 2) where the laser pulse is impinging, for an enhanced laser absorption process, and acceleration with additional laser pulses [26] have been investigated and even if results are promising, they usually involve additional difficulties and costs.

4.2 Methodology and content of the study

The research on beam lines for manipulating the laser-driven proton beam is gaining more and more interest within the scientific community, led by the necessity of obtaining improved proton beam parameters for exploiting the applications.
Two of the most important requirements for numerous applications are:

- being able to lower the energy spread of ion beams generated by TNSA, down to a few percent around the central energy,
- obtaining reliable and stable proton beams that can be controlled easily (e.g. having the option of tuning the energy easily),
- having a high repetition rate beam line that allows to obtain reproducible, reliable proton bunches at high frequency (multi-Hz repetition rate).

The use of commercial laser systems, coupled with beam tailoring devices for beam transport, beam focusing and energy selection, enables several applications which demand a narrow energy spectrum.
The goal of this study is to characterize a laser-driven proton beam line, as shown in Fig. 2. The beam line system is made of both a beam collimation scheme and an energy selection device.
The devices that we have used for both the energy selection device of Paragraph 4.5 and the beam focusing stage of the beam line of paragraph 4.6, are those typically used in the case of

conventional proton accelerators. The energy selection device is based on a sequence of magnetic dipoles that lead to a spatial dispersion of the laser-accelerated proton beam, allowing an energy selection of the particles of the proton bunch. The focusing stage of the beam line is made by an array of magnetic quadrupoles that capture the beam from the laser-plasma source and collimate it into the ES (see paragraph 4.5 for further details).

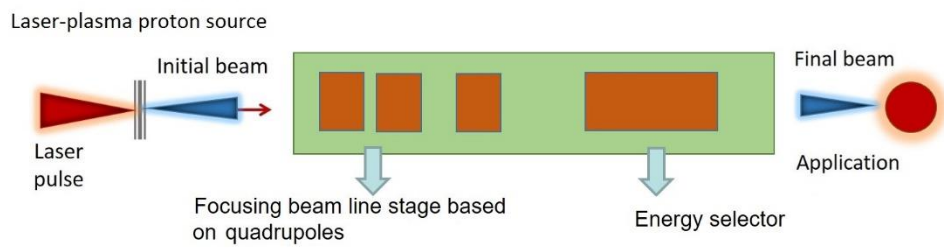

Fig. 7 – Qualitative scheme of the laser-driven proton beam line. The focusing stage accounts for the capture and collimation of the proton bunch from the laser-plasma source. The ES reduces the energy spread of the initial beam, leading to a narrower energy spread of the final beam.

The methodology that we have used for optimizing the elements of beam line, is very similar to what is done in the case of conventional particle beams. When dealing with beam dynamics issues related to conventional accelerators, the beam line that shapes the particle bunch parameters is previously analyzed with particle optics and particle tracking codes. With numerical codes we have evaluated the final beam parameters, obtained with a given scheme of a beam line, starting from a specific set of initial parameters. Customizing the initial parameters typical for laser-plasma proton beams allows simulating these types of sources and investigating the performance of a beam line based on conventional elements.
For the analysis of the ES and the capture/focusing line, we used both a beam optics code, TRACE3D [27], and a particle tracking code, TSTEP [28]. This allowed us to optimize the beam optics upstream the ES and evaluate the efficiency of the energy selection process of the beam line by simulating the particle distribution of the beam with parameters that are coherent with the typical feature of the TNSA regime.

There have been previous studies and realizations of magnetic selector devices for laser-generated proton beams. [29] [30] However, existing devices are either optimized for low-energy ranges (below 10 MeV) or they reach up to energies (up to 60 MeV) that are at the upper limit of the typical energy spectrum of TNSA. For the latter case, these devices have large dimensions and even if they cover a wide range of energy, they seem to be over-dimensioned for the typical applications of TW-laser systems, in the 2-20 MeV range and their size could represent a problem for interaction chambers of medium-small laser facilities. Furthermore, this kind of energy selection device requires a narrow divergence of the incoming proton beam, in order to work efficiently (see Paragraph 4.5.3 for further details) and requires a collimation system after the laser-plasma source. As research activity concerning the focusing of TNSA beams has been conducted (see Chapter 1), the goal of our study is to explore the feasibility of coupling focusing elements with the energy selection device.

4.3 Acceleration of proton beams with high-intensity lasers: Target Normal Sheath Acceleration

The TNSA mechanism allows obtaining proton beams with interesting features, often complimentary to what can be obtained with conventional accelerators. Several experiments showed that this kind of proton source possesses unique characteristics:

- Excellent transverse laminarity (more than 100 times better than conventional accelerators [31] [17]
- Extremely small equivalent source size (μm) [32]
- Very short duration of the source (∼ps)
- Maximum energy of the protons up to tens of MeV
- Wide energy spectrum (up to 100 %)
- Very high current at the source (∼kA)
- Intrinsic compactness of the acceleration: from 0 to a few tens MeV in a few ten microns

For practical applications, fluctuations in the ion energy spectrum, position of the virtual source, its size, angular beam profile and other properties of the source and possibly beam transport system, should be kept under control and reduced to the required level. For laser-plasma based proton injectors, Antici et al. use an energy spread of ∼3 % [24]. In the case of material science applications, such as the synthesis of nano-particles (see Paragraphs 4.4.1 and 4.4.3), an energy spread of a few tens percent is required in order to improve the quality of the generated nano-structured surface.
Nevertheless, the ongoing research concerning laser-plasma proton acceleration has made the TNSA mechanism a reliable and well understood phenomenon. The use of commercial laser facilities with a power in the range of hundreds of TW is sufficient to trigger the TNSA. Therefore, this acceleration mechanism is well suited for applications that require a high repetition rate (up to tens of Hz is obtainable with modern commercial laser systems).

4.3.1 Laser-plasma interaction in the TNSA regime

The TNSA acceleration mechanism is produced by irradiating a solid, flat target with an intense laser pulse, as pictured in Fig. 3.
The laser system parameters that are required in order to trigger the TNSA mechanism are:

- The laser intensity on target should be $I\lambda^2 > 10^{18}\ W \cdot cm^{-2} \cdot \mu m^2$
- Laser pulse energy of a few J, up to hundreds of J
- Laser pulse duration of a few tens fs, up to ps (a power of >10 TW)

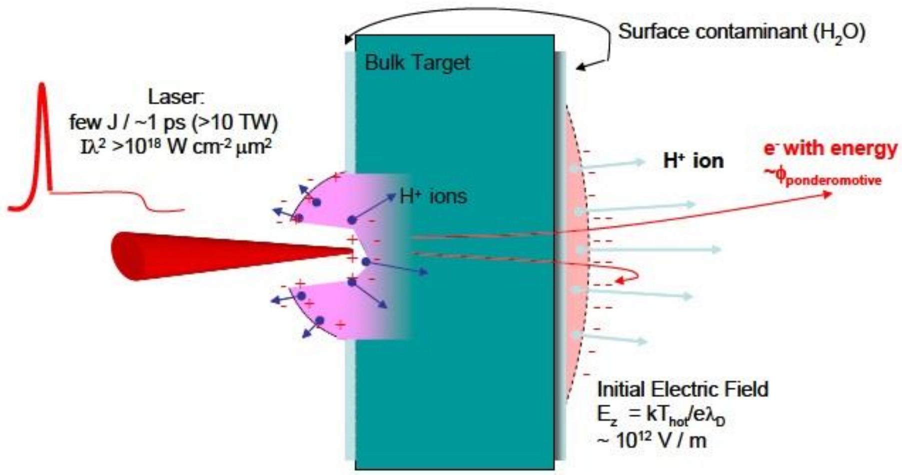

Fig. 8 – Basic scheme for the TNSA acceleration process from the rear surface of a solid target. Electrons from the bulk are accelerated and create a strong electric field on the rear surface that ionizes water contaminats and accelerates them orthogonally from the back side of the target. Extracted from the PhD thesis of P. Antici [53].

The solid target that is typically used in TNSA experiments is made of a thin metallic foil (Au, Ag or Al) with a thickness of hundreds of nm up to tens of µm [19].
Let us consider energetic electrons that are produced inside the bulk target when a high intensity laser interacts with a solid foil. The TNSA mechanism relies on the fact that electrons are accelerated in the forward direction inside of the target's bulk, mainly due to the $j \times B$ force. They reach typical mean energies of $E \sim \Phi_{pond} \sim 1$ MeV, where Φ_{pond} is the ponderomotive potential which scales with the square root of the laser intensity:

$$\Phi_{pond} = m_i c^2 \cdot \left(\sqrt{\left(1 + \frac{I_{18}\lambda^2}{1.37}\right)} - 1 \right),$$

where m_i is the ion mass, c is the velocity of light, λ is the wavelength of the laser pulse and I_{18} is the intensity of the laser pulse in terms of $10^{18}\ W \cdot cm^{-2}$.

Electrons propagate through the target as they have a mean free path that happens to be much larger (electrons with an energy of $\sim$ 1MeV have a mean free path of $\sim$ 1mm) than the thickness of the targets typically used in experiments. A small part of the electrons (those at higher levels of energy) manage to escape from the target and some of those that have escaped, are retained by the potential built in the target. Therefore, at the target rear surface interface, the remaining electrons form a dense sheath over a Debye length λ_D [33] [34]:

$$\lambda_D = \sqrt{\frac{\epsilon_0 T_e\, k_B}{n_e e^2}},$$

where ϵ_0 is the permittivity of vacuum, e is the electron charge, k_B is the Boltzmann constant, n_e the electron density and T_e the electrons temperature. In the case of electrons with a temperature of T = 1 MeV and a density of $10^{20}\ cm^{-3}$, the resulting Debye length has a value of about 0.7 µm.
This means that the electrostatic potential is concentrated in an extremely small region and because of the electrons' high density, the electrostatic field gradient becomes extremely steep. Thanks to the density and temperature of electrons on the rear surface of the target and to the value of λ_D the electric field confined in that region is in the order of some TV/m, as detected experimentally and numerically.
The field on the rear surface of the target can be calculated by

$$E_0 = \sqrt{\frac{n_e T_e k_B}{\epsilon_0}} = \frac{k_B T_e}{e\lambda_D},$$

giving a value of $\sim 10^{12}$ V/m for an electron temperature of $\sim$1 MeV and a Debye length of $\sim$1 µm.
This field ionizes the atoms of the contaminants on the back side of the target, mainly Hydrogen from vapor, and rapidly accelerates them normally to the initially unperturbed surface. As a result, a bunch of Hydrogen ions, i.e. protons, and ions coming from the bulk of the target (Carbon ions in case of plastic targets and metallic ions in case of Au, Al of Ag targets), is accelerated from the rear surface of the irradiated target.

4.3.2 Theoretical model for the maximum energy of TNSA proton beams

An acceleration model has been developed to obtain predictions of maximum ion energies which can be useful for experimentalists [35]. This model uses theoretical results on the isothermal expansion of a hot plasma, coupled to a model of characteristic ion acceleration time. By studying the dependence of this characteristic time on various parameters, it has been possible to extend the validity of this model to very short pulse durations. This study has also allowed to link the characteristics of TNSA accelerated ion beams to the characteristics of the energetic electron population, in order to develop a new diagnostic for this electron population for laser-plasma interaction experiments [36]. To obtain an analytical estimate of the maximum energy that can be gained by protons accelerated forward from the back surface of the target [12] [35] [37] it is possible to use the approach chosen by Mora [38], which was based on an approach initiated in the seventies to treat the expansion of a plasma in vacuum, and adapted to the case of a hot electron burst initiating the expansion. In the case of a self-similar isothermal expansion, a simple evaluation of the accelerated ions maximum energy is:

$$E_{max} = 2 \cdot ZT_{hot} \cdot \left[\ln\left(t_p + \left(t_p^2 + 1\right)^{1/2}\right)\right]^2, \tag{4.1}$$

where T_{hot} is the electron temperature in the sheath on the rear surface of the target and $t_p = \omega_{pl} \times t_{acc}/(2 \cdot \exp(1))^{1/2}$ with t_{acc} the acceleration time and $\omega_{pl} = \sqrt{\frac{n_{e0}Ze^2}{m_i \epsilon_0}}$ the ion plasma frequency (n_{e0} is the initial electron sheath density at the back of the target and m_i the ion mass). As already mentioned, in most experiments, a plasma is located on the front surface during the target irradiation by the main pulse. In this case, T_{hot} can be well approximated using the ponderomotive potential. Starting from a hot electron cloud, there is a progressive energy transfer through the electrostatic fields to the ions. Nevertheless, such an adiabatic model cannot be solved analytically but only numerically. The ambition of the model represented by Eq. 4.1 is to use an isothermal model that has the advantage of being simple and easy to be used analytically: it considers a finite (determined) acceleration time and the hot electron population is maintained at a constant temperature. The acceleration time t_{acc} is in the order of magnitude of tens of fs (up to ps, depending from the duration of the laser pulse), with a minimum of 60 fs, as confirmed by PIC simulations [35]. The initial electron sheath density n_{e0} depends from the dimension of the laser-pulse, focused on the target, and the thickness of the target itself [35] [36] [39].

In conclusion, the analytical work on the maximum proton energy produced on the back side of the irradiated target, has allowed to obtain an evaluation tool that is able to correctly reproduce existing data obtained from various experiments and to extrapolate it to other laser parameters.

4.3.3 Typical parameters of TNSA accelerated proton beams

Because of the high energy required for electrons to escape the target from the rear surface, the TNSA mechanism was only made possible by the advent of high power laser with short pulse durations. However, presently available commercial TW-power class laser systems allow exploiting the TNSA mechanism routinely.
Therefore, the acceleration mechanism described is a standard proton acceleration mechanism that produce ion beams with interesting features like low emittance, high brightness, high laminarity, short duration and high spectral cut-off, as shown in Fig. 4 where a typical energy spectrum of a TNSA accelerated proton beam is reported.
The energy spectrum of a typical TNSA accelerated proton beam covers energies starting from a few hundreds of keV and has a maximum energy cut-off as high as tens of MeV (the specific cut-off energy depends from the laser and target parameters that have been used). The decay of the number of protons from the low energy range to the maximum energy is exponential, as $dN/dE \propto \exp(-(2E/T_{hot})^{1/2}$ [12].

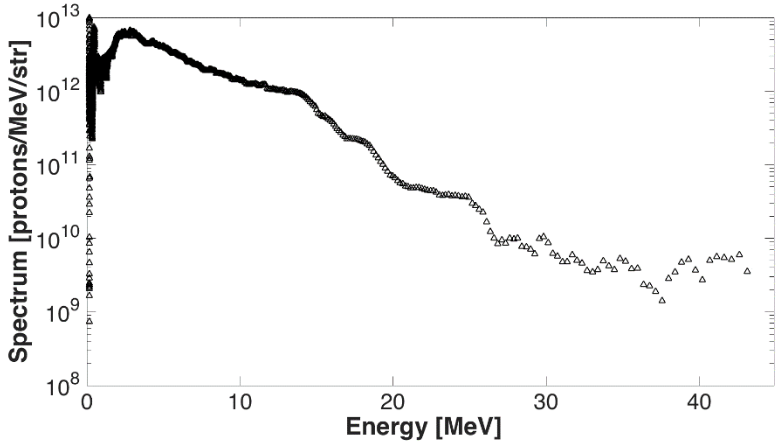

Fig. 4 – Typical energy spectrum of a TNSA accelerated proton beam as obtained on the TITAN laser facility in 2016. The number of protons decays exponentially, reaching a maximum energy of tens of MeV.

We have already said that protons are accelerated by the hot electron sheath. Indeed, the proton beam divergence is linked to the electron sheath topology.
A deeper insight of the electron sheath topology has been investigated experimentally by Cowan et al. [17] who could establish, that for protons above 4.5 MeV, the decrease in the angular envelope with energy is due to a decrease of the emitting zone, but not due to a strong change in the divergence (i.e. magnification) of the beam envelope).
The protons, when ejected from the target, do not propagate all straight in the same direction but have a certain divergence: high energy protons are less divergent than low energy protons, i.e. low energy protons spread out of the target within a larger angle, as described in Fig. 5. The higher energy protons are accelerated from the tip of the sheath with a very small divergence angle. As the proton energy decreases, the divergence angle of the proton beam gets larger (protons are accelerated from the wings of the sheath distribution). It is possible to measure the divergence of proton beams with RCFs, as shown in Fig. 6 and reported by Gaillard et al. [40].

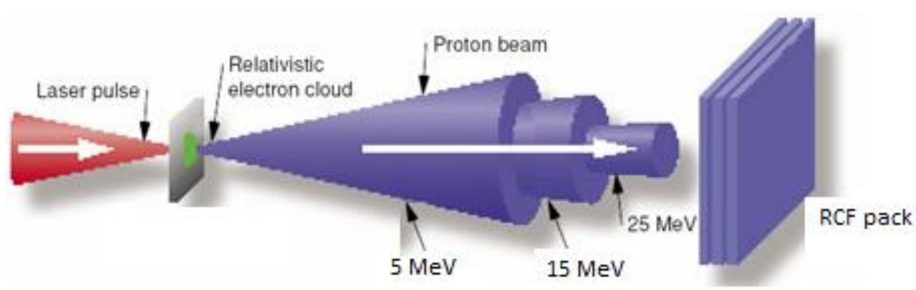

Fig. 5 – Simplified graph of the acceleration cone for the TNSA mechanism. The low energy protons are accelerated within a larger angle, whereas the high energy protons have a smaller divergence.

Measurements of the proton divergence angle as a function of the energy, performed by Mancic et al. [9] are shown in Fig. 7. This figure summarizes the advantages and disadvantages of a TNSA proton beam. The advantage is to routinely have a high number of particles (especially at medium-low energies where up to $\sim 10^{13}$ part/MeV/srad can be obtained) accelerated to energies up to tens of MeV. Disadvantages are that the energy spectrum is of almost 100 % and the angular distribution of the protons is as wide as tens of degrees, making the control and transport of the beam challenging.

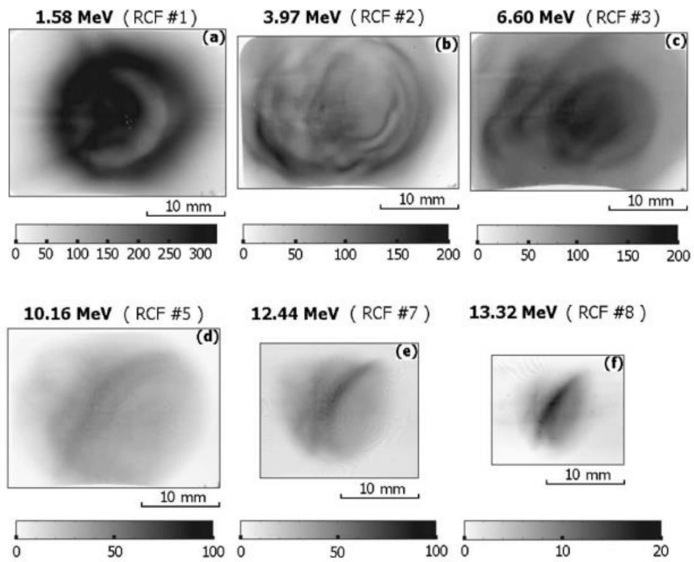

Fig. 6 – Detection of the accelerated proton beam with RCFs. It is visible how the beam divergence is higher at lower energies. The protons are centered around a) 1.58, b) 3.97, c) 6.60, d) 10.16, e) 12.44, f) 13.32 MeV. The beam has been accelerated using the LULI 100 TW laser in combination with a 25 µm thick Al foil. Extracted from Ref. [40].

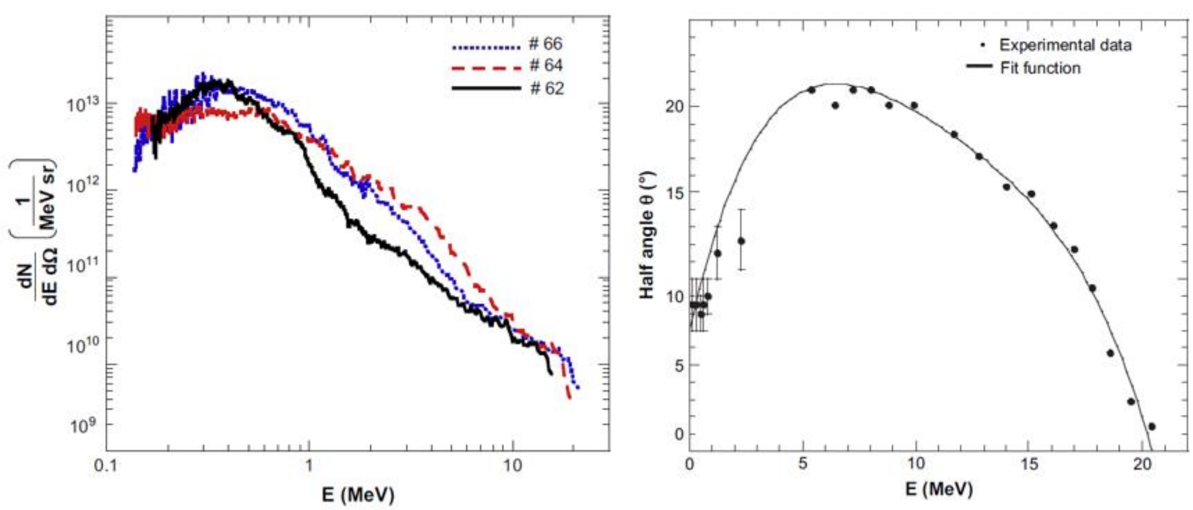

Fig. 7 – Left plot: proton spectra of three different shots, using a 100 TW laser system at $\lambda = 1057\ nm$ wavelength, on a 10 µm thick Au target. Right plot: measurements of the proton beam divergence as a function of the energy. Extracted from Ref. [9].

Even though proton acceleration occurs also on the front surface of the target (i.e. the surface irradiated by the laser pulse), the acceleration process on the rear surface is the most suited to produce a high quality and laminar beam, if no particular set-ups concerning laser contrast or targets dimensions are used. Moreover, with nowadays lasers, more energetic ions are generated on the back of the target than on the front. Unless special methods are used to attenuate the laser pre-pulse (e.g. with plasma mirrors, as it has been done in Ref. [41]), the target front surface is damaged by the laser pre-pulse before the TNSA mechanism can occur when the main pulse arrives. Acceleration from the front surface produces less energetic protons for different laser-target conditions as confirmed by PIC simulations performed in a wide range of parameters (for laser intensities going from 10^{17} to $10^{20}\ W \cdot cm^{-2}$, and for laser pulse duration ranging from 10 fs to 500 fs) and experimental evidence. A comparison between proton spectra accelerated from the front and rear surface of a solid target is shown in Fig. 8.

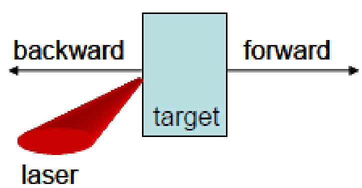

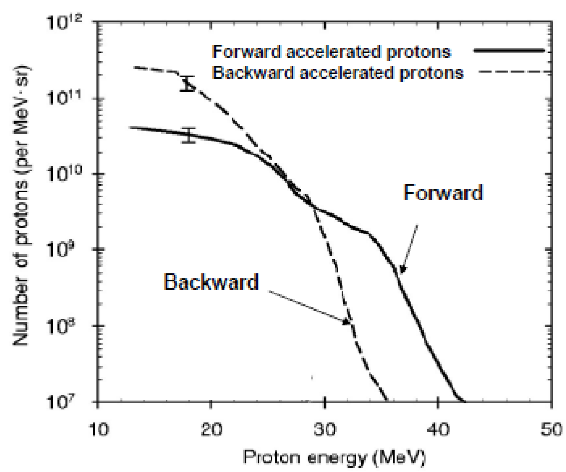

Fig. 8 – On the left, a schematic for defining backward and forward acceleration from the solid target, irradiated by the laser pulse. On the right, a comparison for the energy spectra of protons steming from the two sides of the target. The beam coming from the front surface shows ~1 order of magnitude less protons and ~7 MeV less maximum energy, compared to the rear surface. Extracted from McKenna et al. [52] who used 700 fs long laser pulses (energy up to 400 J) irradiating 100 μm thick iron foils in order to generte the accelerated protons.

In conclusion, the TNSA acceleration is a reliable mechanism that delivers high energy proton beams routinely. In the next paragraph we will discuss some of the applications that can rely on the TNSA mechanism, from a point of view of the required proton energy, but still require an improvement of the beam quality in terms of energy spread and angular divergence.

4.4 Applications of TNSA laser-driven proton beams

Laser-plasma accelerated protons can be used for several applications, exploiting the energy range that is obtainable with the TNSA mechanism, i.e. from hundreds of keV up to tens of MeV. In this paragraph we discuss two of the applications that can be exploited, from the point of view of the required maximum energy, with proton beams accelerated with the TNSA mechanism, i.e. routinely available using TW-power class laser systems.
Moreover, the beam parameters that we aim to achieve with the proton beam line of Paragraphs 4.5 and 4.6, are those required by the applications in the domain of material science (the analysis of Cultural Heritage), which we report here.

4.4.1 Ion beam analysis of Cultural Heritage

The use of laser-generated proton beams, even at low energy (<10 MeV), is exploitable for the Ion Beam Analysis (IBA) of materials, i.e. investigating the elemental composition of a material irradiating it with energetic proton (or heavier ion) beams. However, when depth precision is required for the material analysis, quasi-monoenergetic proton beams are necessary.
Materials irradiated with an energetic proton beam will emit photons as X- and Gamma-rays (Proton-induce X-ray emission (PIXE) and Proton-induced Gamma-ray emission (PIGE)), with an energy that is typical of the electrons of their K-shell. [42] [43] By detecting the emitted radiation, it is possible to retrieve information about the elements that compose the sample that has been irradiated.
This technique is widely used and can be applied to the analysis of cultural heritage artifacts (CH). In numerous laboratories and museums (e.g. at the Louvre in Paris or at the Uffizi in Florence) the analysis of CH with proton beams is performed with conventional electrostatic accelerators, delivering a proton beam of ∼3 MeV. [44] [45] Bronze, marble, gold artifacts are analyzed, as well as pigments such as those of ancient paintings, shown in Fig. 9.

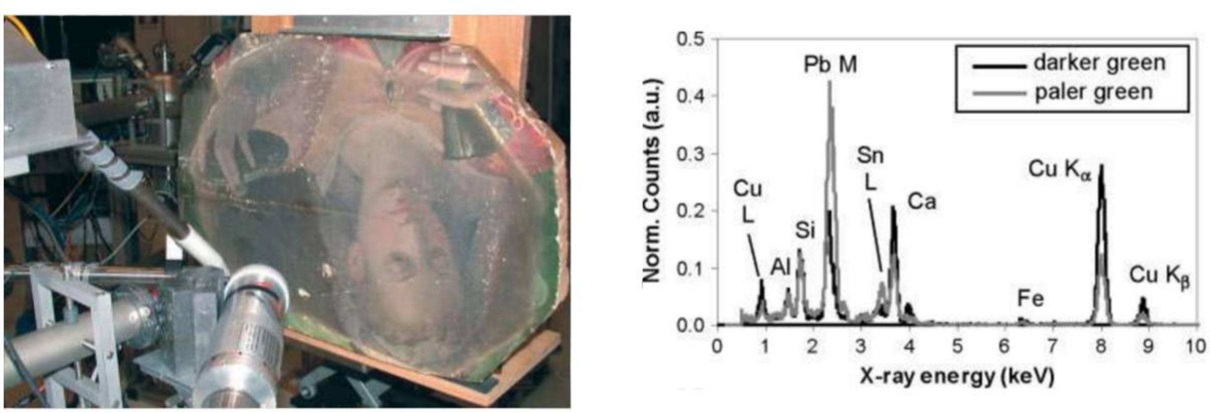

Fig. 9 – PIXE analysis of a painting by Giorgio Vasari with a conventional accelerator. On the left, X-ray spectra as measured for green areas with different pigments. Extraxted from Ref. [45].

The drawback of using conventional machines, is that they provide a beam with a low, almost continuous current which does not allow to perform the material analysis over a short time: as the peak of the proton flux is low, the emitted radiation is strongly affected by noise. Hence, a time integrated detection of the emitted radiation is necessary in order to have a clean signal. This leads to the necessity to irradiate the sample over several minutes, increasing the risk of damaging the artifact or alter its features permanently.

The high number of protons of a typical TNSA beam, combined with the short bunch duration, leads to a high peak current that would possibly allow a more efficient emission of the x-rays carrying the information about the sample's material. This could lead to a decrease of the necessary dose delivered to the target, in order to perform a precise analysis.

Moreover, having a low-energy, tunable, proton beam with a low energy spread allows performing a scan of materials such as bronze, marbles and pigments (i.e. common materials in CH artifacts) at a depth of tens (up to a few hundreds) µm, with a sensitivity of ppm.

The narrow energy spread allows having a high precision of the depth of the material layer that is analyzed (i.e. the depth at which the protons deposit the majority of their energy due to the Bragg-peak).

4.4.2 Laser-plasma based injector for conventional acceleration schemes

TNSA beams, due to their potential high repetition rate and high charge, are a suitable candidate for the injection in post-acceleration schemes based on conventional accelerating structures.

If the beam parameters are improved after the laser-plasma source, in terms of energy spread and transverse divergence, laser-accelerated proton bunches can be injected into resonant cavities for a further increase of their energy, as reported in previous studies. [24]

In Ref. [24] numerical simulations have been performed using an initial TNSA beam with a mean energy of 7 MeV, having an energy spread of a few %, showing that the use of Drift-tube-linac accelerating cells (i.e. conventional resonant cavities used for proton accelerators, as shown in Fig. 10) can be used for a post-acceleration scheme.

The narrow energy spread is assumed to be achieved via the use of a micro-lens that selects the beam in the longitudinal phase space. However, such a device requires the use of a second laser pulse and represents a challenge from the point of view of the synchronization.

The use of a beam line based on passive devices, such as those studied in this work, would allow to obtain a narrow energy spread of the initial TNSA beam without increasing significantly the complexity of the experimental setup.

In conventional proton accelerators, e.g. a proton linac, the low energy stage represents the biggest challenge, since at low energy the space-charge effects are much more significant. For this reason, Radio-Frequency-Quadrupoles [46] are often implemented (for accelerating the beam up to typically ~ 5 MeV), in order to keep the transverse dimension of the beam under control along the initial path of the accelerator where the protons are accelerated from the keV range to a few MeV. [47] Replacing the conventional low energy acceleration stage with a compact laser-plasma source, would represent a significant advantage for the design of a modern proton linear accelerator.

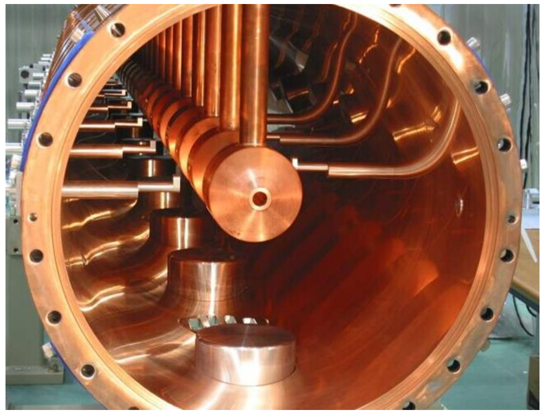

Fig. 10 – An accelerating resonant cavity, based on DTL cells. Such conventional devices are suitable for post-acceleration of TNSA proton beams.

4.5 Optimization of an energy selection device for laser-accelerated proton beams

As introduced before, one of the main drawbacks of the TNSA acceleration mechanism is the extremely broad energy spectrum of the proton beam that is generated at the laser-plasma source. As reported in Fig. 5 of paragraph 4.3, all energies, from the keV up to the multi-tens of MeV range, are covered. Hence, an energy selection device is necessary in the proton beam line, in order to decrease the energy spread of the proton beam, for the applications that require quasi-monoenergetic beams.

A possible design of a passive magnetic energy selector device consists of a magnetic chicane built with four permanent magnets, one entrance slit and one selecting slit. [29] [30] A qualitative scheme of such a device is pictured in Fig. 11.

The goal of this configuration is to generate a dispersion of the multi-energetic proton beam via the Lorentz force, leading to a correlation between the particles' energy and their transverse position.

A magnetic dipole bends the trajectory of the accelerated charges particles that travel through the magnetic field with a force as

$$\overrightarrow{F_L} = q\left(\vec{v} \times \vec{B}\right),$$

where v is the velocity of the particles, q their electric charge and $\vec{B}$ the vector of the magnetic field of the dipole. Since the modulus of the Lorentz force is related to the value of the velocity, particles are bent according to their momentum p (i.e. their energy, if they all have the same rest mass) with a bending radius that is given by the beam rigidity $B\rho$:

$$B\rho = \frac{p}{q}. \tag{4.2}$$

The magnetic chicane of Fig. 11 displaces the particles from the propagation axis, i.e. the trajectory a particle with infinite energy would have. On the transverse plane $x - z$, their displacement x_D is related to the parameters of the dipole (i.e. magnetic field and magnetic length) and on the momentum of the particle.
The result is that a proton beam with an energy spread will be dispersed on the $x - z$ plane with a correlation between the transverse position x and the energy of the single particles. As shown in Fig. 11, by moving the selecting slit along the x-axis, it is possible to select different central energies of the proton beam. The slit selects a spatial portion of the beam on the dispersion plane, which results in an energy selection due to the relationship between bending radius and momentum of Eq. 4.2. To each transverse position x of the aperture of the selecting slit of Fig. 11, corresponds a central, reference energy p_S that is selected.

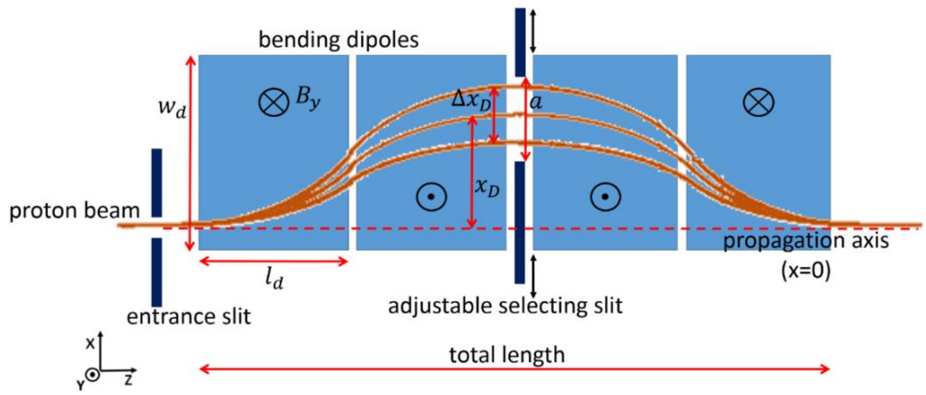

Fig. 11 – Scheme of the selection device based on conventional magnetic dipoles. The proton beam is bent throughout the magnetic chicane and the dispersion has its maximum between the second and third dipole. The selecting slit can be adjusted transversely in both position and aperture.

Particles with a different energy from the reference energy go through the slit, due to the spatial aperture a: the particles of the beam with $\Delta x_D = D \cdot \frac{\Delta p}{p_S} < a$ pass through the ES. Δp is the energy difference with respect to the central energy p_S of the selecting slit and D is the dispersion function of the magnetic chicane.
The four dipoles are placed symmetrically with respect to the central selecting slit, allowing the proton beam to return on its original propagation axis, at the exit of the selector.

The slit at the entrance of the ES is required to reduce the divergence of the incoming beam, which is in the order of tens of degrees at the source. [9] This is necessary in order to avoid that the intrinsic divergence of the particles influences their transverse position along the ES and alters the energy selection process (as discussed in Paragraph 4.5.3, the transverse position x in a dipole, also depends from the initial divergence x'_0). It is impossible to cancel this effect completely, however, reducing the divergence of the beam from a fraction of radians to a few mrad, significantly increases the effectiveness of the energy selection (as we will discuss more into detail in the Paragraph 4.5.3).

The energy range of our interest is 2 to 20 MeV and we aim to study the effectiveness of the energy selection process of the ES for this class of proton beams. With numerical particle tracking simulations, we analyzed how the length l_d of the dipoles, their width w_d and the strength of the magnetic field B_y have an impact on the energy selection process of this device in terms of energy bandwidth and efficiency. We define the efficiency of the selection process as the ratio between the particles coming out of the ES and those entering the entrance slit (see Fig. 11), at the selected central energy of the final beam. Thus the efficiency is

$$\eta = \frac{N_{out}|_{p_s}}{N_{in}|_{p_s}} \ . \tag{4.3}$$

Furthermore, we investigated the sensibility of the system to changes of the aperture a of the selecting slit and the initial divergence x_0' of the proton beam.

With numerical codes used for beam dynamics studies of conventional accelerators, it is possible to analyze the dispersion of the proton beam travelling through the magnetic chicane. The parameters of the dipoles, such as their length and the strength of the magnetic field, have an influence on the trajectory of the laser-accelerated protons. Hence, it is useful to investigate the sensitivity of the energy selection process to a variation of these parameters.
For this reason, we performed a parametric study of the device of Fig. 11 by running several series of particle tracking simulations with the code TSTEP. Every series of simulations has the aim of monitoring the efficiency of the energy selection process in case of a variation of one of the physical parameters of the ES. All the other parameters are kept constant, as well as the input parameters of the proton beam.

4.5.1 Beam displacement and energy range of the energy selector

We studied how the dimensions of the magnetic dipoles, i.e. the length l_d and the width w_d, and their field strength B_y, can affect the device's energy range and the ability to select a narrow energy band of the beam.
The total length and the width of the device are key aspects when the interaction chamber has limited dimensions. Therefore, keeping the size of the selector as compact as possible (i.e. using short dipoles with a narrow width) is important.

In Fig. 12 we show simulation results, obtained with TSTEP, for the displacement x_D of the particles of the beam for different central energies, measured at the z-position of the central slit (i.e. between the second and third dipole). The length of the dipoles is $l_d = 10\ cm$ for this set of simulations and we suppose that there is no empty drift space between the dipoles. Stronger magnets deflect the particles by a greater angle, thus their displacement x_D after the second dipole is greater. Particles with lower energy undergo a greater displacement: this defines the lower limit of the energy range of the ES. The dipoles must be wide enough to cover the maximum displacement of the particles at low energies: it must be that $x_D < w_d$ for all the energies within the range of the ES. For example, data show that with magnets using $B_y = 1\,T$ a length $l_d = 10\,cm$ and a width $w_d = 12\,cm$, the lower limit of the ES is about 0.7 MeV. Longer dipoles having a higher field strength, need to be wider for selecting correctly the proton beam at low energies.

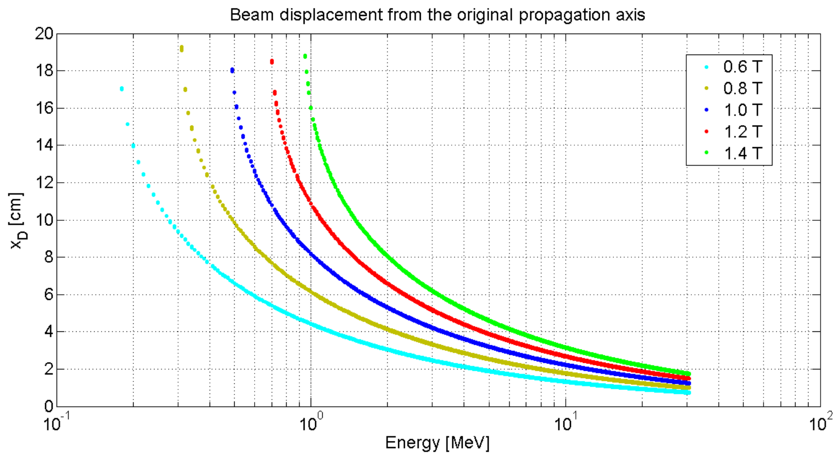

Fig. 12 – Transverse displacement of the beam induced by the magnetic dipoles, at the z-position of the selecting slit (i.e. between the 2nd and 3rd dipole), as a function of the energy. The simulations have been run for 10 cm long dipoles with B_y fields ranging from 0.6 to 1.4 T.

With the information from the data of of Fig. 12, it is possible to tune the energy range of the ES by adjusting the vertical position (i.e. the position along the x-axis) of the chicane's dipoles. By moving the two central dipoles in x-direction, it is possible to cover a wider range of energies (i.e. decreasing the lower limit of the energy range), since the trajectory of the protons with a greater displacement becomes covered by the magnetic field of the central dipoles. Obviously, by doing so, the upper limit of the energy range is decreased, as the protons with a higher energy, that have their trajectory closer to the propagation axis, do not enter into the magnetic field of the central dipoles.

The curves illustrated in Fig. 12 are useful, as they show the transverse position of the particles as a function of the energy, along the trajectory through the magnetic fields of the chicane.

4.5.2 Parametric analysis of the field intensity and the dipole length

As discussed in paragraph 4.5, the dispersion of the proton beam depends from the length of the magnetic dipoles and their field strength. In Fig. 13 and 14, we study the effect of these two parameters on the energy selection process.

For all the simulations of these series (see Fig. 13 and 14), we took the same input distribution for the proton beam: the beam has a transverse dimension of 500 µm (uniform distribution) and a divergence of 3 mrad (half-angle, position-correlated) both on the x- and y-direction. These initial parameters can be obtained by putting an entrance slit with an aperture of 500 µm, about 8 cm away from the proton source (a reasonable distance, considering the typical dimensions of an interaction chamber, which usually have a diameter of ~1 m). As shown in Fig. 11, using an

entrance slit before the first dipole is the easiest way to collimate the beam, lowering its divergence to the order of magnitude of mrad, allowing the ES to work correctly (for further details, see the simulation series concerning the initial beam divergence, in paragraph 4.5.3).
The input energy spectrum is a uniform distribution ranging from 7.5 to 12.5 MeV, i.e. having a central energy of 10 MeV ±25 %. This energy range allows having a good comparison between the unselected beam and the final beam, as the energy selection process is expected to yield a final energy spread of <20 % (see Fig. 15 and 16). We chose to select a central energy of 10 MeV, using a central slit with an aperture of a = 500 µm.

In the simulations, we used a particle distribution with a uniform energy spectrum, as input for the particle tracking code. The units of the number of particles are arbitrary. The energy distribution does not reproduce the exponential decay that is typical for TNSA proton beams. However, our goal was to characterize the selection process of the ES only: the final bandwidth and the ratio between the number of protons at the entrance and at the exit of the ES are relevant in this section of our study. In order to have a prediction of the energy selection process on a realistic energy spectrum, it is sufficient to scale the data that we report, with the values of proton quantities that have been found in TNSA experiments.

In Fig. 13 we show numerical results of the ES with different dipole lengths, with an ideal magnetic field B_y of 1 T.
The simulations show how longer dipoles provide the ability to select a narrower energy spectrum, but have a lower efficiency. For instance, with four 16 cm-long dipoles (light-blue curve) we obtain a bandwidth of <1 MeV Full-Width-Half-Maximum (FWHM) and an efficiency of 18.6 %. Whereas with 8 cm long dipoles the final energy spread is $\sim$2 MeV (FWHM) wide and the efficiency is 25.7 %. These data show how using longer magnets provides an advantage in terms of final energy spread but leads to a lower efficiency.
For the energy range of our interest, there is a minimum length of the dipoles that is required for a given strength of the B_y_field: with 4 cm long dipoles, it appears to be impossible to select the beam at 10 MeV central energy, with a narrow final energy spread: the beam coming out of the ES has an energy bandwidth that is almost as wide as the one of the input distribution (see the blue and black curves of Fig. 13).

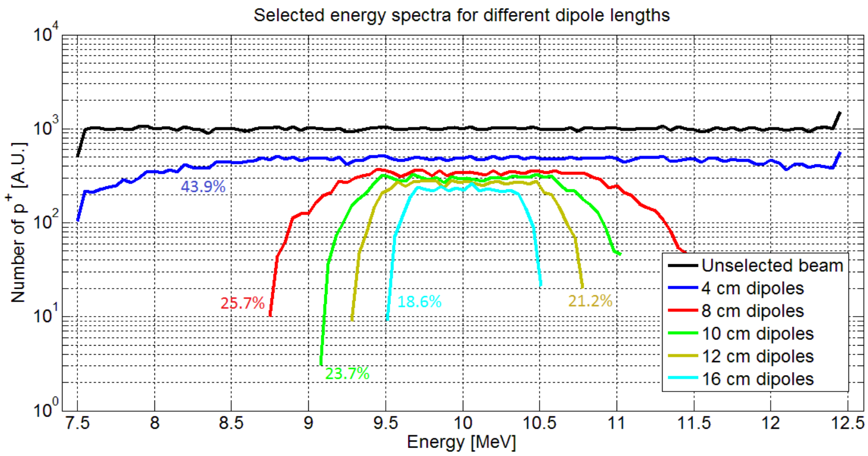

Fig. 13 – Beam energy spectrum of the protons passing through the ES. The black curve represents the energy spread of the proton distribution before entering the ES. The colored curves represent the final energy spectra of the protons at the exit of the ES, for different values of the dipole length l_d. The field intensity is fixed at 1 T and the selecting slit has an aperture of a=500 µm. The incoming proton beam is collimated to an initial divergence of 3 mrad half-angle. Percentages next to the plots indicate the efficiency of the selection process, as defined by Eq. 4.3.

The maximum strength of the magnetic axial field B_y of the dipoles depends on the material the permanent magnets are made of. As reported by many manufacturers, Nd-Fe-B sintered magnets represent the state of the art for permanent-magnet-based devices. Commercial magnets built of this rare-earth material can reach a remanence magnetic field of up to 1.45 T. [48]
We took this value as a reference for our simulations: we performed simulations with field strengths going from 0.6 to 1.4 T, in order to cover all reasonable values for the magnetic dipoles of the ES (we consider values below 0.6 T as too low for selecting energies as high as 20 MeV, using dipoles with compact dimensions).

Fig. 14 shows how the use of dipoles with different B_y fields reduces the energy spectrum of the selected proton beam. We compare five simulations, varying the magnetic field B_y of the dipoles from 0.6 to 1.4 T. The length of the dipoles is $l_d = 10\ cm$ for all the cases and the selecting slit has an aperture of a = 500 µm. The divergence of the incoming beam is fixed at 3 mrad (half-angle). The dipoles we have simulated are ideal, i.e. they don't present fringe fields and the strength of the magnetic field is uniform over the whole length of the magnets.
Since a stronger magnetic field generates a greater spatial dispersion in the chromatic proton beam, the energy displacement curve shown in Fig. 12 has a steeper slope at the position of the selecting slit, i.e. the particles having $\Delta x_D < a$ have an energy that is closer to the selected energy p_s. Fig. 14 shows that the efficiency of the device is almost unaltered and that the use of dipoles with a higher field strength, gives a moderate advantage in terms of bandwidth. Even if dipoles with a stronger B field lead to higher manufacturing costs, due to more expensive materials of the magnets, they can be used if a narrow final energy spread is required and it is not possible to increase the length of the dipoles (as discussed in Fig. 13), e.g. due to space constrains.

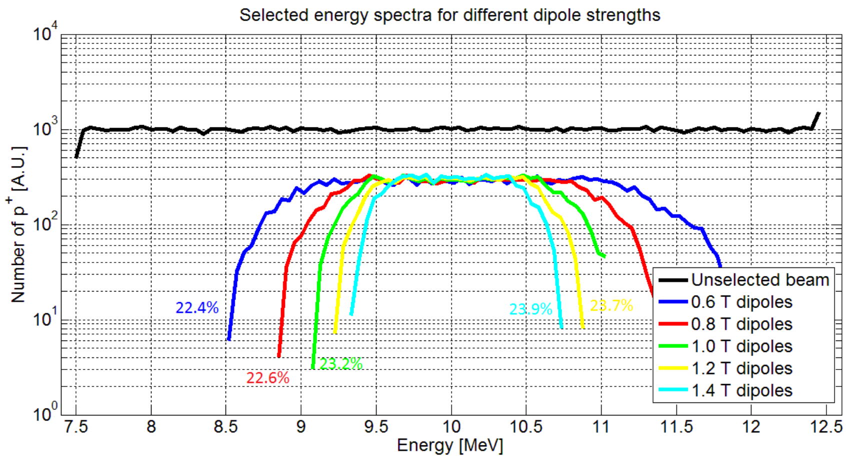

Fig. 14 - Beam energy spectrum of the protons passing through the ES. The black curve represents the energy spread of the proton distribution before entering the ES. The colored curves represent the final energy spectra of the protons at the exit of the ES, for different values of the magnetic field B_y. The dipole length is fixed at 10 cm and the selecting slit has an aperture of a=500 µm. The incoming proton beam is collimated to an initial divergence of 3 mrad half-angle. Percentages next to the plots indicate the efficiency of the selection process, as defined by Eq. 4.3.

4.5.3. Parametric analysis of the selecting slit's width and the initial beam divergence

The aperture of the selecting slit is a key parameter accounting for both the final energy spread of the proton beam and the number of particles that are transmitted throughout the ES. As we discuss here, the choice of the width of the selecting slit must be a compromise between proton fluency at the end of the ES and the final energy spread of the beam. Indeed, the results reported in Fig. 15 show that the energy bandwidth of the final beam is narrower if a smaller slit is used, but, on the other hand, the final number of transmitted protons decreases significantly.
The parameters of the ES geometry, for this set of simulations are: 10 cm long dipoles with a field intensity of 1 T. The curves show how the $a = 50\ \mu m$ slit has an efficiency almost ten times lower that the $a = 500\ \mu m$ slit (3.1 % against 23.2 %). In the case of a 50 µm slit, the selected beam has a bandwidth of ~1.6 MeV, whereas in the case of a 500 µm slit, it is ~1.8 MeV.
These data show how a wide selecting slit is preferable when dealing with applications that require a high proton number and the requirement concerning the final energy spread is more relaxed. In general, for low central energies, the displacement curve shown in Fig. 12 has a steeper slope, which means that even particles with similar energies are separated by a relatively large space and, therefore, a wider selecting slit is sufficient for obtaining an efficient energy selection.

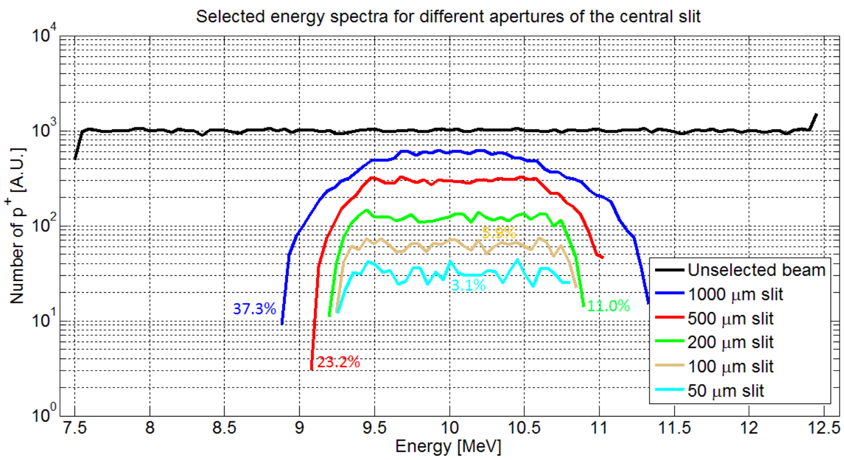

Fig. 15 – Beam energy spectrum of the protons passing through the ES. The black curve represents the energy spread of the proton distribution before entering the ES. The colored curves represent the final energy spectra of the protons at the exit of the ES, for different values of the aperture of the selecting slit a. The dipole length is fixed at 10 cm and the magnetic field has an intensity of 1 T. The incoming proton beam is collimated to an initial divergence of 3 mrad half-angle. Percentages next to the plots indicate the efficiency of the selection process, as defined by Eq. 4.3.

Furthermore, we studied the effect of the intrinsic divergence of the incoming proton beam, on the energy selection process.

At the source, protons are accelerated within a cone with an aperture of tens of degrees with a non-uniform angular distribution (the protons with higher energies are accelerated within a narrower cone). [9] Even if the entrance slit of the ES reduces the divergence of the entering beam by several orders of magnitude, the transverse momentum of the protons interferes with the spatial displacement induced by the dipoles. The trajectory of the particles is influenced by their initial divergence and their transverse position at the center of the magnetic chicane is not given only by the displacement by the dipoles.

Even a beam divergence of a few mrad has a relevant effect on energy selection process, especially at higher energies where the displacement from the original axis is small (see Fig. 12) and the perturbation induced by the initial divergence is not negligible.

The behavior of the ES for beams with different divergences is reported in Fig. 16. The simulations were run using distributions of the proton bunch having different divergences. The beams of these simulations travel through the same ES (10 cm long dipoles wiht a fileld strength of 1 T). The selecting slit is 500 μm wide for all cases.

The curves of Fig. 16 show the final energy spectra of proton beams with intrinsic divergences that range between 0.5 to 10 mrad (half-angle). The initial transverse dimension of the proton beam is given by the collimating entrance slit. For these simulations, the initial beam spot size is 500 μm. At a distance in the range of a few cm from the laser-plasma source, the use of a 500 μm wide slit is sufficient for obtaining a divergence of a few mrad. If the ES needs to be placed nearer to the laser-plasma source (e.g. due to less available space in the interaction chamber), a smaller slit is required for collimating the proton beam at an angle of a few mrad.

Fig. 16 shows how the intrinsic divergence of the proton beam has a significant influence on the final energy spread. For example, after going through the ES, a beam with a divergence of 3 mrad

half-angle has about three times the energy bandwidth than the one with 1 mrad half-angle divergence, i.e. ~0.9 MeV half-width for the first case and ~0.3 MeV half-width for the latter.
The efficiency of the ES, as well, is improved when the beam is confined within a tighter angle: considering the initial and final number of particles at the selected central energy, about 57 % of the particles of the incoming beam are transmitted through the ES if the divergence is 0.5 mrad. This value decreases to 10 % for the case of a beam with a divergence of 10 mrad. A tighter collimation (i.e. less divergence) of the beam that enters the chicane of the ES, requires using a smaller slit that will block a greater part of the protons steaming out of the TNSA source. Thus, the size of the entrance slit should be a compromise between (I) the number of particles that are necessary for a given application, (II) the required energy bandwidth after the ES (i.e. the intrinsic divergence the ES can tolerate), (III) the physical space available in the interaction chamber (i.e. the distance between the source and the exit ES) and (IV) the features of the source (i.e. number of produced particles, correlation between energy and emission angle at the energy range of interest). Nevertheless, as we will discuss in paragraph 4.6, using a focusing system between the laser-plasma source and the ES allows decreasing the losses, in terms of proton fluency, that are caused by the presence of the collimating slit.

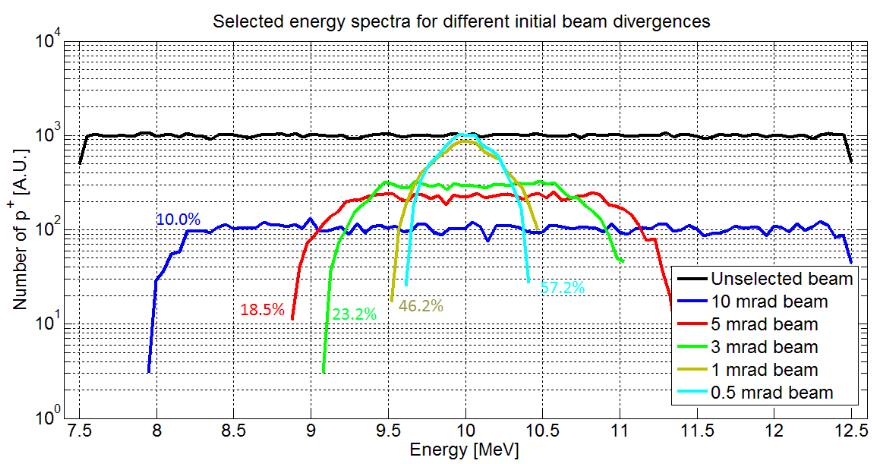

Fig. 16 - Beam energy spectrum of the protons passing through the ES. The black curve represents the energy spread of the proton distribution before entering the ES. The colored curves represent the final energy spectra of the protons at the exit of the ES, for different values of the initial beam divergence. The dipole length is fixed at 10 cm, the magnetic field has an intensity of 1 T and the selecting slit has a width of 500 µm. Percentages next to the plots indicate the efficiency of the selection process, as defined by Eq. 4.3.

The initial number of protons, after the beam has passed through the initial slit, strongly depends from the angular distribution at the source. The aim of this set of simulations is to compare the energy selection process independently from the features of the laser-plasma source.
For this reason, the plots of Fig. 16 show the same initial proton distribution for different initial beam divergences (black curve). The black energy spectrum, which is the input for all simulations, represents an ideal case scenario, where reducing the divergence of the beam does not affect the number of particles. Even if the input particle distribution of these simulations do not represent realistic cases, it is useful to compare the final energy spectra of the different beams with the only influence of the intrinsic beam divergence. The aim of this part of the study is to

indicate an acceptable initial divergence of the proton beam that allows an efficient energy selection process of the ES. As we will discuss in paragraph 4.6, these data allow optimizing the focusing stage of the beam line in terms of proton fluency and final energy spectrum.
For obtaining realistic values for the final proton fluency, it is sufficient to scale the final quantity of protons reported in the figure, using a typical TNSA spectrum such as those reported in Ref. [9] or [3].

4.5.4. Optimization of the energy selector's working point with particle tracking simulations

The goal of the parametric study of the ES is to analyze the dependence of the two key indicators of the energy selection process, i.e. energy bandwidth and efficiency, from the physical parameters of the ES.
As a following step of our research, we investigated the sensitivity of the energy selection process to the variation of l_d and B_y in more detail. We performed additional series of particle tracking simulations (again with the code TSTEP) aiming to characterize every possible combination of parameters of the ES.

For the simulations of this paragraph, we fixed the initial beam divergence, the width of the selecting slit and the central energy that is selected by the ES. For a given set of these parameters, we interpolated the values of the final energy spread of the beam, obtained with different combinations of l_d and B_y. By doing so, it is possible to indicate the optimal values of these two parameters if the initial beam conditions are fixed and the required value of the final energy spread is given.
Fig. 17 shows data interpolation (performed with the numerical code MATLAB) from TSTEP simulations where l_d and B_y vary from 4 to 16 cm and from 0.6 to 1.4 T, respectively. The selected energy is the same for all the combinations and the initial beam parameters. The color-scale indicates the value of the final energy spread that is obtained as a function of l_d and B_y.
We have run a series of these simulations for all the energies within the range of our interest, i.e. 2-20 MeV. This procedure has then been repeated for different values of initial beam divergence, in the range 1-5 mrad. For all simulations of this paragraph, the aperture of the selecting slit is fixed at 500 µm, as a compromise between final proton fluency and final energy spread (see the discussion of the previous paragraph).
From the data reported in Fig. 17 it possible to establish a "working point" of the optimized ES for a given selected energy: the colored areas indicating the final value of energy spread, allow identifying the possible combinations of physical parameters of the ES that allow achieving the required energy spectrum. The expected proton fluency after the ES can be evaluated by the efficiency of the device that is reported (in terms of order of magnitude) for the different cases of energy and beam divergences.

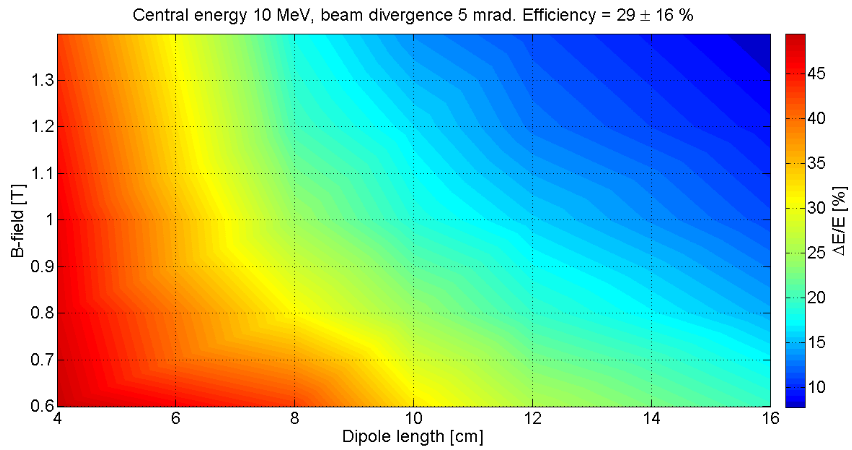

Fig. 17 – Final energy spread (colored areas) as a function of length and magnetic field strength of the dipoles of the ES. The central selected energy is 10 MeV for all the combinations. The initial beam divergence is fixed at 5 mrad. The value of the efficiency indicates the range for this particular central energy.

The results shown in Fig. 17 represent only one example of the working point maps that we have obtained. In Appendix II we report the interpolated data of particle tracking simulations of the other energies we have analyzed (5, 10 and 20 MeV). In Appendix II initial beam divergence from 0.5 mrad to 5 mrad are reported.

4.5.5. Analysis of the energy selector with optimized parameters

The parametric analysis of the ES allows optimizing the dimensions and the field of the dipoles, according to the requirements of a given application. For example, applications in the domain of material science (as discussed in Paragraphs 4.4.1 and 4.4.3) require the final proton beam to be quasi-monoenergetic, in order to achieve a sufficient depth precision of the analyzed material sample. As a rule of thumb, an energy spread of a few tens percent allows having a depth precision of tens of µm in the most common materials of CH (see Paragraph 4.4.1). Hence, we established the goal value of the final energy spread to be <20 % (FWHM). The energy range that is of interest goes from 2 to 20 MeV (the typical range of TNSA proton beams from hundreds-TW power class lasers), in order to allow scanning the material sample at different depths (ranging from a few µm depth to ∼100 µm depth using the high energy part of the beam). The data discussed in the previous paragraph indicate possible combinations of dipole length and field strength that yield a final energy spread meeting this requirement.
The light-blue area of Fig. 17, for example, indicates a possible set of parameters of the ES at a central energy of 10 MeV. The choice of the parameters of the optimized ES need to be done by analyzing the working point maps, such as in Fig. 17, for all the energies within the range 2-20 MeV (or, at least, for the minimum and maximum energy of the range). The data reported in all the working point maps we have generated (see Appendix II), allowed us to choose an optimized set of parameters for the ES. According to the data from the simulations, we choose to study the optimized device more in detail using the following parameters:

$l_d = 10\ cm$
$w_d = 8\ cm$
$B_y \approx 0.95\ T$
$a = 500\ \mu m$

These parameters lead the total dimensions of the device $\sim 48 \times 18 \times 12\ cm$ (L x H x W).

The set of four dipoles has been simulated with the code SUPERFISH [49] (using the parameters of commercially available rare-earth-materials) in order to obtain realistic field profiles (both longitudinally and transversely). The data of the magnetic simulations have been imported in the particle tracking code TSTEP in order to run accurate simulations with a realistic magnetic field configuration.
In Fig. 18 we report the longitudinal profile of the vertical component of the B-field generated by the dipole chicane, as obtained with SUPERFISH. For this simulation, we used the magnetic parameters of commercially available rare-earth permanent magnets [48]. The gap between the magnets' surfaces is 1 cm. The spacing between the outer magnets is 1 cm, whereas the spacing between the central magnets is 2 cm, in order to have enough space to place the adjustable selecting slit (see Fig. 11).

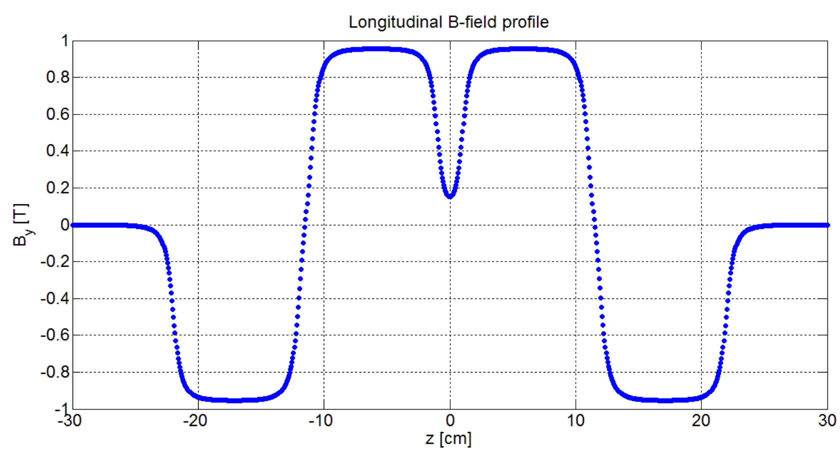

Fig. 18 – Longitudinal B-field profile of the four dipoles of the ES. The static magnetic field has been calculated with the code SUPERFISH. The realistic field profile has been used for the particle tracking simulations of the optimized selection device.

Fig. 19 and Fig. 20 show particle tracking simulation results for the beam displacement (i.e. energy range) and energy selection of the optimized ES. These simulations were run using realistic field profiles for the magnetic dipoles, as they include fringe fields and non-uniformity of the magnetic area.
From Fig. 19 we can establish the lower energy range of the ES to be about 1 MeV, as the displacement for particles with this energy is < 8 cm, i.e. the width of the dipoles. Moreover, from this curve, it is possible to tune the ES by placing the selection slit at the correct distance from the original propagation axis, according to the desired central energy.

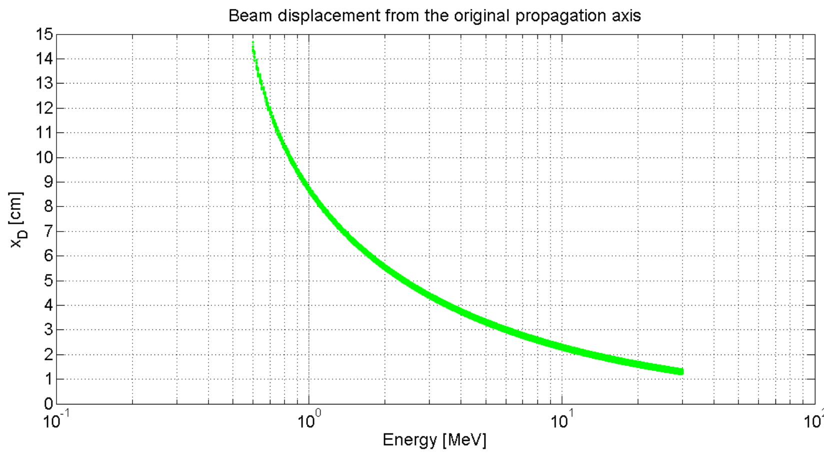

Fig. 19 – Displacement of the protons as a function of the energy, for the optimized ES, as obtained with the particle tracking code TSTEP. The parameters of the device are those mentioned above, using the realistic B-field profile of Fig.20.

Fig. 20 shows the final energy spread of the TNSA proton beam before and after the optimized ES, simulated with a realistic longitudinal field profile. The device yields a final energy spread of <20 % FWHM for all central energies from the desired range. Indeed, the energy spread after the selection process is 6.25 %, 11.5 %, 15.25 % and 17.77 % FWHM for a central energy of 2, 5, 10 and 20 MeV respectively. The efficiency of the device is ∼20 % for all energies. This value of efficiency refers to the ratio between the quantity of particle entering the ES and those passing through it, as defined by Eq. 4.3. Hence, the efficiency is evaluated for the energy selection process only, i.e. it does not take into account the losses due to the beam collimation provided by the first entrance slit.

The input particle distribution (black curve) is obtained by scaling the energy of a proton spectrum coming from a 2D-PIC simulation of proton acceleration driven by laser-plasma interaction [50]. The PIC simulation takes into account the typical features of the ALLS TW-class laser system: 800 nm wavelength, 30 fs laser-pulse duration, ∼2 J laser energy on target impinging on a solid foil made of aluminum with a thickness of 120 nm [41]. The distribution used for the TSTEP simulations reproduces the exponential decay of the number of protons for growing energies. The PIC simulatios of Ref. [50] use the laser parameters mentioned above and yield a maximum energy of ∼10 MeV generated by the TNSA mechanism [41]. However, the used laser parameters underestimate the features of state-of-the-art commercial, high-repetition rate laser systems that can accelerate protons to higher energies via TNSA. For this reason, we increased the energy of the proton beam up to ∼ 27 MeV in order to obtain a spectrum coherent with those found in several experiments of proton acceleration with TW-class lasers [9] [19]. The exponential slope of the spectrum is the same of Ref. [50]. The results of Fig. 22 are obtained for an initial divergence of the proton beam (provided by the initial entrance slit) of 5 mrad half angle and a selecting slit with an aperture of 500 µm.

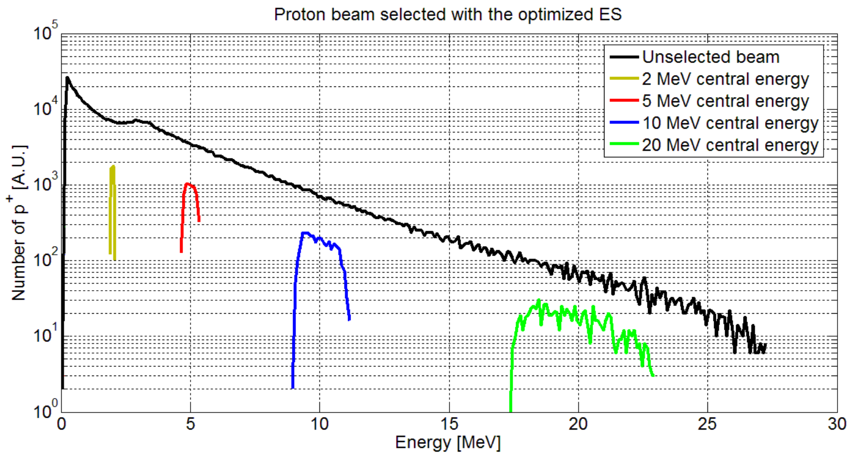

Fig. 20 – Particle tracking simulations of the ES with optimized parameters (TSTEP code). Energy spectrum of the unselected beam (black), imported from a PIC simulation, and energy spectra of the selected beams. The central energies that have been simulated are 2, 5, 10 and 20 MeV.

4.6. Analysis of the proton beam line's focusing stage, based on permanent magnet quadrupoles

For an efficient transmission of the proton beam from the laser-plasma source to the ES, a collimation system is required that reduces the divergence of the beam at the entrance of the ES. The numerical results discussed so far, take into account proton beams that have a divergence in the order of magnitude of mrad and, thereafter, require a device that lowers the divergence that is typical for TNSA beams.

Using a slit for blocking the protons with a divergence larger than what is acceptable for the ES (i.e. a few mrad, see Fig. 16) is a possible solution. The scheme of Fig. 11 can be placed right after the laser-plasma source: the combination between distance and aperture of the entrance slit, defines the divergence of the beam entering the ES. However, this method leads to significant losses in terms of bunch charge: the beam has a divergence of tens of degrees at the source [9], thus the great majority of the particles are blocked by the entrance slit.

An improved solution is represented by the use of a focusing system, based on PMQs, that captures the beam from the TNSA source and collimates the protons into the entrance slit of the ES. Compared to the scheme that uses a slit only, a beam line with a focusing stage based on magnetic quadrupoles, allows capturing a greater fraction of the initial TNSA beam and collimating it into the ES. As reference parameters, i.e. the dimensions and the achievable magnetic gradient, we took the results reported in Ref. [51].

4.6.1. Optimization and magneto-static analysis of the focusing permanent magnet quadrupoles

For studying the focusing system we considered the following main aspects: I) The focusing quadrupoles need to have compact dimensions, be easy to implement and be commercially available. II) The focusing stage of the beam line needs to be adaptable to multiple energies in the range 2-20 MeV.

Especially the second condition represents a challenge, since optimizing the parameters of a focusing array of quadrupoles usually is done for one given energy of the beam. Using the same quadrupoles to focus particles at different energies, requires a tradeoff between efficiency of the focusing and versatility of the devices.

As first step of our analysis we run simulations with both a magnetic field solver, called PANDIRA (an extension of SUPERFISH), and the beam optics code TRACE3D. The aim was to study, at the same time, the feasibility of a given permanent magnet quadrupole (PMQ) design [51] and its versatility to focus a range of energies as wide as possible.

With TRACE3D we looked for optimized parameters of the focusing quadrupoles by running a matching algorithm that gave the optimal values of focusing strength and spacing between the magnetic elements. This gave us approximated parameters for the PMQs that we have simulated further on to check the feasibility of the focusing devices and perform more accurate simulations with a particle tracking code (see later).

We set goal parameters, in terms of Twiss α and Twiss β, for the final proton beam, as obtained at the end of the PMQ array. Optimizing the quadrupoles for $\alpha = 0$ and $\beta = 100\ m$, allows obtaining collimated beam with a divergence of a few mrad at the entrance of the ES. For even lower values of β, i.e. an even more tight focusing of the beam, the algorithm fails to optimize the spacing between the quadrupoles.

At first, we run simulations by keeping both the magnetic field gradient of the quadrupoles and the spacing between them as free parameters. By doing so we were able to evaluate the most versatile parameters of the quadrupoles, that can be used to implement a beam line that is adaptable to multiple central energies. The data that we have obtained indicate that with two types of quadrupoles, having a field gradient of 160 and 300 T/m (reported in Fig. 23 with Q1 and Q2, respectively), it is possible to capture the particles from the source, adjusting the beam line to the energies within the range 2-20 MeV of our interest. Obviously, for different central energies of the beam line, the spacing between the quadrupoles needs to be adjusted accordingly.

In order to optimize the spacing between the quadrupoles, according to the central energy that will be selected by the ES, a second set of simulations has been run with TRACE3D by keeping the parameters of the quadrupoles as fixed variables. We analyzed several combinations, i.e. sequences, of quadrupoles by running the matching algorithm for multiple central energies, with the aim to find the optimal spacing between the quadrupoles. The code delivered an optimized focusing line for the energies within the range of interest.

In Fig. 21 we report TRACE3D results showing a focusing scheme optimized for a central energy of 10 MeV.

The blue curve and the top-right phase space plot of Fig. 21 show that the beam is collimated in the x-plane. It is sufficient to lower the divergence of the proton beam in the dispersion plane of the ES (see previous paragraph). The quadrupoles are not capable to capture all the particles of the beam, as it is visible from the red curve of Fig. 21 indicating the beam transverse dimension in the y-plane (the beam vertical dimension exceeds the quadrupole's bore diameter). However, we managed with these simulations to obtain optimized parameters for the quadrupoles of the focusing stage. From the results of Fig. 21, we obtained the spacing between 6 quadrupoles of the beam line focusing the protons with an energy of 10 MeV. In the plot only four devices are pictured because the first and last quadrupole in the plot have double length with respect to the central ones and so can be replaced by two shorter quadrupoles, placed at a close distance. By doing so, the optimization algorithm of TRACE3D delivered more accurate results since the free variables (i.e. the spacing between the quadrupoles) are reduced.

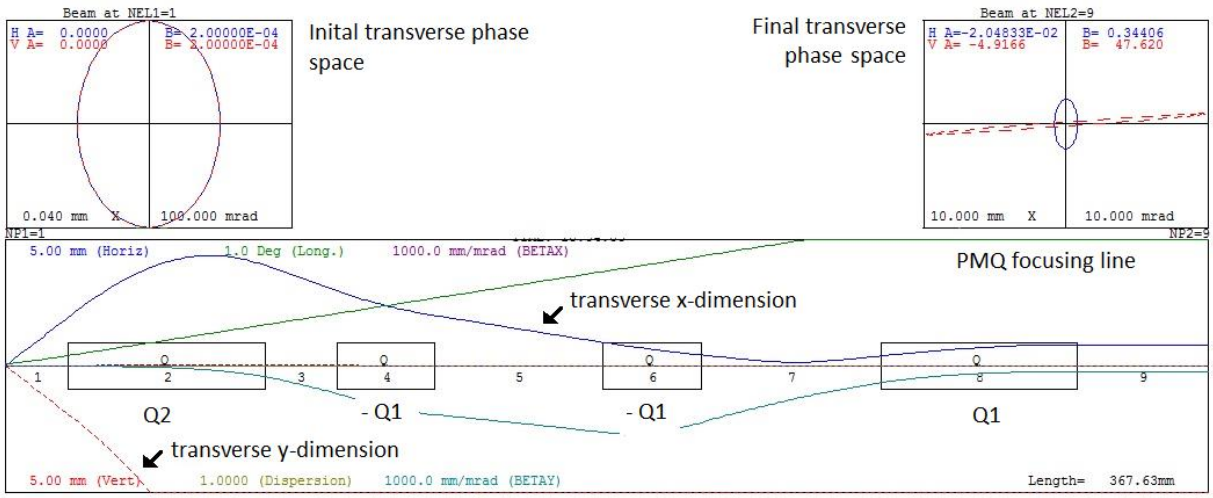

Fig. 21 - Proton beam transverse dimensions and divergence as obtained by the code TRACE3D for a 10 MeV beam. Top-left plot: phase space of the initial proton beam. Top-right plot: phase space of the final proton beam. Bottom plots: Transverse dimensions of the proton beam (blue and purple curve: x-dimension; red and green curve: y-dimension), as a function of the distance from the laser-plasma source (z=0). As visible, the four PMQs are capable of collimating the proton beam in the x-direction. The two outer quadrupoles have a double length: they can be split into four quadrupoles with the same length as the central ones.

Both the field gradients that have been calculated with TRACE3D are achievable with state-of-the-art permanent magnet materials. In Fig. 22 and 23 we report the results of a PANDIRA (an extension of SUPERFISH) simulation. The analyzed PMQs are made of differently polarized rare-earth permanent magnet (FeNeB) segments, as available commercially. We took the parameters of the material directly from the data sheets that are available on the web sites of magnet manufacturers: the magnetic characteristics of the simulated material are similar to those of VACOMAX 225 by Vacuumschmelze [48].

As shown in the two figures, by changing the geometry of the quadrupole, it is possible to obtain magnetic field gradients of different strengths. The two solutions reported here, are made of 12 sectors of permanent magnet material, with a bore radius of 1 and 0.5 cm respectively. The magnetic field gradients, as shown in the plots, are of 160 T/m and 300 T/m. These high gradients are required to compensate the high divergence of the proton beam at the source.

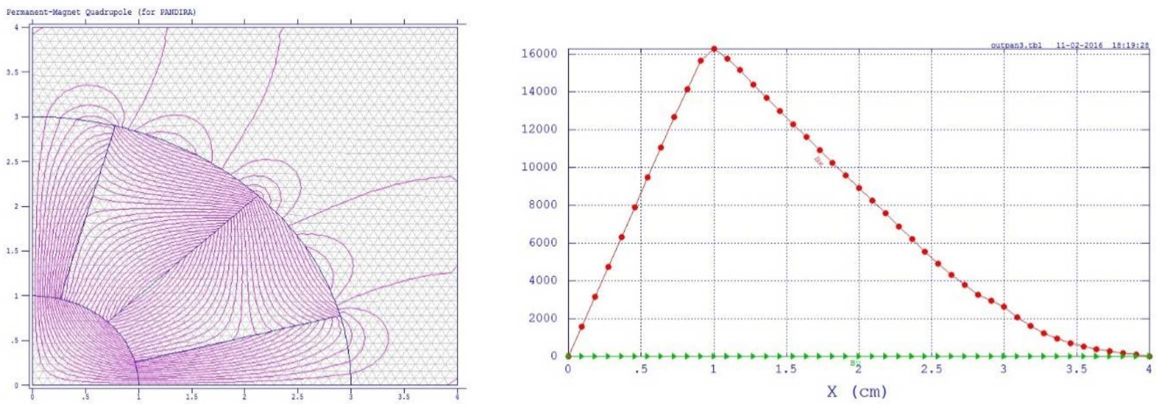

Fig. 22 – Results from the static magnetic field solver provided by SUPERFISH. On the left, the schematic of the PMQ's geometry and the magnetic field map. The bore radius is of 1 cm and the outer radius is of 3 cm. On the right, the magnetic field profile along the x-axis, from the center of the PMQ to the outer edge.

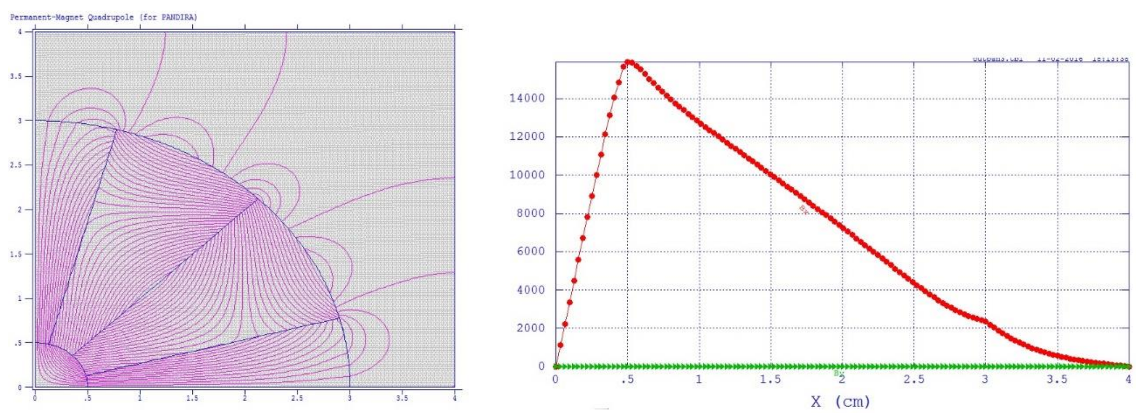

Fig. 23 - Results from the static magnetic field solver provided by SUPERFISH. On the left, the schematic of the PMQ's geometry and the magnetic field map. The bore radius is of 0.5 cm and the outer radius is of 3 cm. On the right, the magnetic field profile along the x-axis, from the center of the PMQ to the outer edge.

4.6.2. Particle tracking start-to-end analysis of the proton beam line

The last part of our numerical study regarding the quadrupole based focusing stage was to run more accurate particle tracking simulations with the code TSTEP.
With TSTEP it is possible to customize the input particle distribution making it possible to simulate an energy vs. divergence distribution typical of a TNSA source, as the one reported in Ref. [9]. In the study of Mancic et al. a typical TNSA energy spectrum has been measured and the dependence between the proton divergence and energy has been analyzed. Taking these experimental results as input for the numerical simulations allowed us to obtain realistic results. We created a particle distribution representing the features of a TNSA source, as we report in Fig. 24, where the TSTEP input distribution and the experimental data of Ref. [9] are compared.

We adapted the fitting curve of the plot on the right to a proton beam with a maximum energy of ~27 MeV, obtaining the input distribution for TSTEP reported on the left. All the simulations of the series we are discussing in the following, have as input the distribution of the left plot in Fig. 24.

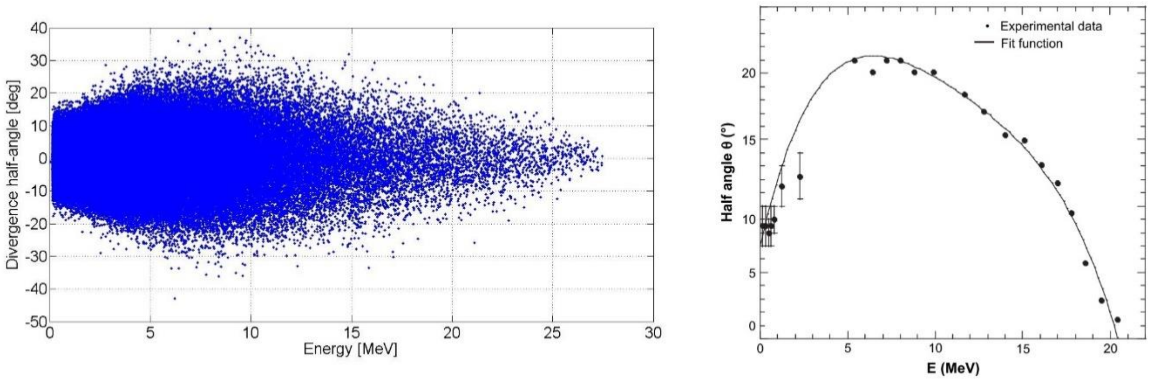

Fig. 24 – On the left, the energy-divergence phase space of the input distribution for the particle tracking simulations (TSTEP). On the right, for comparison, the divergence of a typical TNSA proton beam as a function of the particles' energy. The plot on the right is extracted from Ref. [9].

We run particle tracking simulations for the central energies 3, 5, 10 and 20 MeV, as they represent good examples for our range of interest (see Appendix III for the optimized focusing stage of the beam line). For each energy, the configuration of the quadrupole array has been modified, according to the optimal spacing delivered by the TRACE3D simulations performed previously. The use of the two types of PMQs is indicated by the previous beam optics simulations.

In Fig. 25, we show a snapshot of the simulation representing the energy-divergence phase space of the proton beam at the end of the PMQ line, before entering the ES. As can be seen in Fig. 25, the quadrupoles are optimized for collimating the protons only at the energy that will be selected by the ES.
Focusing a proton beam with an energy spread of 100% introduces chromatic effects, since particles with different energies are focused at different distances. Thus, the PMQ line already acts as an initial energy selection stage, if coupled with the entrance slit of the ES. Further downstream the beam line, the chicane of the ES accounts for a finer energy selection, leading to the final energy spread of the proton beam.

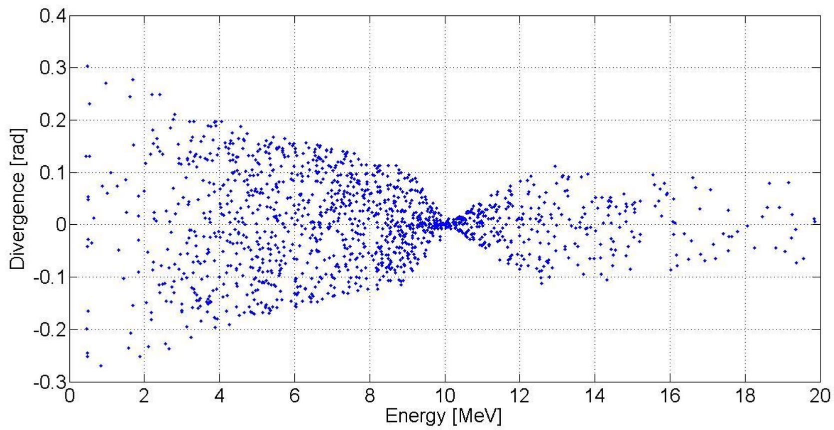

Fig. 25 – Energy vs. divergence phase space of the proton beam as calculated by TSTEP. The snapshot is taken at the exit of the quadrupole array that captures the beam from the laser-plasma source. The spacing between the PMQs is optimized for an energy of 10 MeV. As visible from the plot, at 10 MeV the protons have a low divergence, i.e. they are collimated and can be efficiently sent into the energy selector.

The final step of our study concerns the analysis of the complete beam line made of a focusing stage based on quadrupoles, followed by the energy selection stage made of the dipole chicane that was previously optimized. We have performed a series of particle tracking simulations with TSTEP, using the input particle distribution as reported in Fig. 24. The start-to-end simulations account for all the components of the beam line.

In Fig. 26 we report the scheme of the complete beam line, consisting of both focusing and energy selection stage. The central energy of this particular case is 10 MeV and the devices, i.e. the focusing PMQs and the energy selector, have been simulated with TSTEP, in order to test the performance of the complete beam line and evaluate the efficiency of the energy selection process with a beam focused by the PMQs.
In Appendix III we report the detailed lattice structure of the beam line's focusing stage, optimized for different energies within our range of interest. We have optimized the quadrupole array for 3, 5, 10 and 20 MeV (see Appendix III).

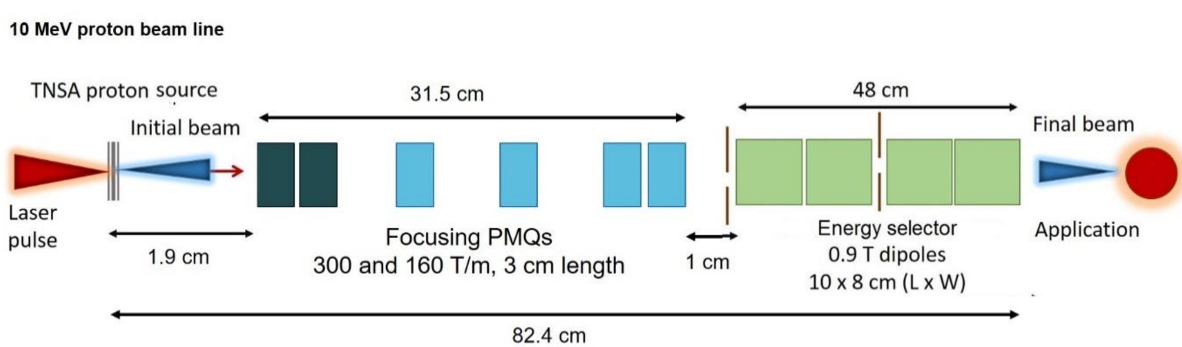

Fig. 26 – Start-to-end scheme of the proton beam line. The protons are captured from the laser-plasma source by an array of 6 MPQs that is optimized for the central energy one wants to obtain. The beam is then sent into the ES, where a finer energy selection process takes place.

The final result of our study is reported in Fig. 27, where the complete beam line is simulated and the initial and final energy spread of the beam are shown. With these start to end simulations, we can finally analyze the energy selection process of the beam line, taking into account all the losses from the laser-plasma source to the end of the beam line. The initial energy spectrum of the beam has the typical shape of a TNSA proton beam (the energy spectrum we have used as an input is the same as the one for the study of the ES only, reported previously in Fig. 20). The colored final energy spectra represent the proton beam at the exit of the ES. The components that are simulated here, have the parameters that have been optimized with the separate analysis reported in the previous paragraphs, i.e. the optimized dimensions and B-field of the ES and the optimized focusing gradient and spacing of the quadrupoles.
From Fig. 27 can be seen that losses, in terms of final particle number, cannot be avoided but the focusing stage reduces the divergence of the beam and enhances the overall efficiency of the beam line, compared to the case with the entrance slit only. The energy spectra show how the quadrupoles act as energy selection devices, as well, but the ES is still necessary to achieve a final energy spread of <20%.

It is important to stress the fact that the efficiency shown in Fig. 20 only takes the losses of the selecting slit in ES into account. Reducing the divergence of the beam using the entrance slit only leads to a loss factor of $\sim 10^3$.
In Fig. 27 (where the ratio between number of protons at the TNSA source and number of protons after the ES is considered) we show that the focusing stage allows improving the start-to-end efficiency to $\geq 1\%$. The final energy spread of the beam is kept below 20% for all energies.

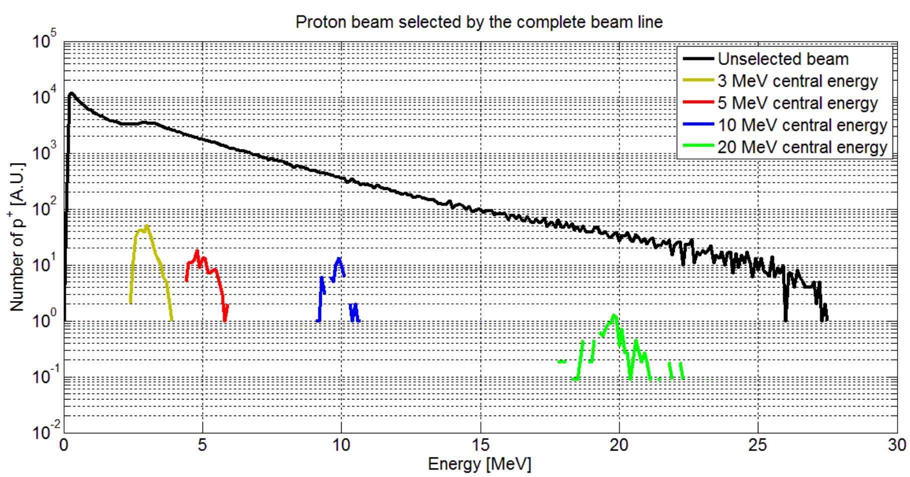

Fig. 27 - Start-to-end simulations of the proton beam line. The colored curves show the energy spectrum of the final proton beam after the beam line devices for focusing and energy selection (i.e. after the PMQ array and the ES), for different selected energies. The initial TNSA proton beam (black) is considered at the laser-plasma source. This set of simulations takes into account all the losses, in terms of number of particles, from the source to the exit of the energy selector.

4.7. Conclusions

We have analyzed a beam line for laser-accelerated proton beams. The calculations we have performed are based on methodologies and tools that are typical of the analysis of beam dynamics issues in the case of conventional accelerators. We have adapted these methods to the case of a laser-driven proton beam with initial parameters that are obtainable with the TNSA acceleration mechanism (i.e. routinely achievable with a hundred TW-class laser system).
The goal of this work was to obtain a final proton beam with a quasi-monoenergetic energy spectrum and a high bunch charge. In order to obtain such a beam, we have optimized the elements of the beam line separately and finally we have run particle tracking simulations in order to investigate the performance of the complete beam line, made of a focusing stage based on PMQs and an energy selection device based on permanent magnet dipoles.

We have shown that the quality of the energy selection process can be enhanced by tuning several parameters, i.e. the strength of the field in the dipoles, their length, the dimension of the entrance- and the selecting-slit.
Particle tracking simulations confirmed that an ES with 10 cm long dipoles, delivering a magnetic field of ~0.95 T, is capable of selecting the initial TNSA proton beam.
Moreover, numerical results prove that the beam divergence that is imposed by the entrance slit has considerable impact on the ability to select a narrow energy band of this kind of devices. From the parametric study concerning the influence of the divergence of the initial proton beam, we could establish that the energy selection process is sufficiently efficient only for initial divergences in the order of magnitude of a few mrad.
Hence, we have studied a focusing system for the proton beam (which has a divergence of tens of degrees at the source), leading to a more efficient collimation, compared to the case where the protons enter in the ES through the initial slit only.

With beam dynamics codes and magnetic field solver, we were able to design the focusing stage of the beam line, based on two types of PMQs (i.e. PMQs with two different focusing gradients, 160 and 300 T/m respectively). The spacing between the quadrupoles needs to be adjusted according to the central energy of the final proton beam. The calculations concerning the optimization of the quadrupole line have been performed using the optimization algorithm of TRACE3D and TSTEP particle tracking simulations. The latter, in order to simulate correctly the initial beam divergence of a TNSA proton beam (i.e. the correlation between energy and divergence of the particles).

The final series of particle tracking simulations take into account all the devices of the proton beam line. The results show that the optimized elements allow obtaining an energy spread of the final proton beam of <20 % (FWHM). The overall efficiency of the beam line, in terms of number of particles that are available at the given central energy, is about 1 %.
This result has been possible only with the use of a collimation system that improves the proton fluency with respect to the case where only the entering slit of the ES is used for reducing the initial proton divergence (in that case, decreasing the divergence from fraction of radiant to mrad, leads to a loss of about a factor 10^3).

The calculations show that this performance is obtainable for all the energies in the range 2-20 MeV, making it possible to implement such type of compact beam line for laser-driven proton applications that require low energy, quasi-monoenergetic beams.

References

[1] F. Begay and W. Forslund, *Phys. Fluids,* vol. 25, p. 1675, 1982.

[2] R. Snavely, M. H. Key, S. P. Hatchett, T. E. Cowan, M. Roth, T. W. Phillips, M. Stoyer, E. Henry, T. C. Sangster, M. S. Singh, S. C. Wilks, A. MacKinnon, A. Offenberger, D. Pennington, K. Yasuike, B. Langdon, B. F. Lasinski, J. Johnson, M. D. Perry and E. M. Campbell, *Phys. Rev. Lett.,* vol. 85, p. 14, 2000.

[3] K. Zeil, S. D. Kraft, S. Bock, M. Bussmann, T. E. Cowan, T. Kluge, J. Metzkes, T. Richter, R. Sauerbrey and U. Schramm, *New J. Phys.,* vol. 12, p. 045015, 2010.

[4] K. A. Flippo, E. d'Humières, S. A. Gaillard, J. Rassuchin, D. C. Gautier, M. Schollmeier, F. Nuernberg, J. L. Kline, J. Adams, B. Albright, M. Bakeman, K. Harres, R. P. Johnson, G. Korgan, S. Letzring, S. Malekos, N. R.-L. Galloudec, Y. Sentoku, T. Shimada, M. Roth, T. E. Cowan, J. C. Fernandez and B. M. Hegelich, *Phys. Plasmas,* vol. 15, p. 056709, 2008.

[5] M. Borghesi, J. Fuchs, S. V. Bulanov, A. J. MacKinnon, P. K. Patel and M. Roth, *Fusion Sci. Technol.,* vol. 49, 2006.

[6] A. Macchi, M. Borghesi and M. Passoni, *Rev. Mod. Phys.,* vol. 85, 2013.

[7] J. Fuchs, P. Audbert, M. Borghesi, H. Pépin and O. Willi, *C. R. Physique,* vol. 10, pp. 176-187, 2009.

[8] J. A. Cobble, R. P. Johnson, T. E. Cowan, N. R.-L. Galloudec and M. Allen, *J. Appl. Phys.,* vol. 92, p. 1775, 2002.

[9] A. Mancic, J. Robiche, P. Antici, P. Audebert, C. Blancard, P. Combis, F. Dorchies, G. Faussurier, S. Fourmaux, M. Harmand, R. Kodama, L. Lancia, S. Mazevet, M. Nakatsutsumi, O. Peyrusse, V. Recoules, P. Renaudin, R. Shepherd and J. Fuchs, *High Energy Density Physics,* vol. 6, pp. 21-28, 2010.

[10] P. Antici, J. Fuchs, S. Atzeni, A. Benuzzi, E. Brambrink, M. Esposito, M. Koenig, A. Ravasio, J. Schreiber, A. Schiavi and P. Audbert, *J. Phys. IV France,* vol. 133, pp. 1077-1079, 2006.

[11] P. K. Patel, A. J. Mackinnon, M. H. Key, T. E. Cowan, M. E. Foord, M. Allen, D. F. Price, H. Ruhl, P. T. Springer and R. Stephens, *Phys. Rev. Lett.,* vol. 91, p. 12, 2003.

[12] J. Fuchs, P. Antici, E. d'Humières, E. Lefebvre, M. Borghesi, E. Brambrink, C. A. Cecchetti, M. Kaluza, V. Malka, M. Manclossi, S. Meyroneinc, P. Mora, J. Schreiber, T. Toncian, H. Pépin and P. Audebert, *Nature Phys.,* vol. 2, pp. 48-54, 2006.

[13] T. Ozaki, J. C. Kieffer, R. Toth, S. Fourmaux and H. Bandulet, *Laser Part. Beams,* vol. 24, pp. 101-106, 2006.

[14] A. Bacci, D. Batani, G. Cirrone, C. D. Martinis, D. D. Side, A. Fazzi, D. Giove, D. Giulietti, L. Gizzi, L. Labate, T. Levato, P. Londrillo, M. Maggiore, L. Martina, V. Nassisi, M. Passoni and A. Sgattoni, *"Plasmi, Sorgenti, Biofisica ed Applicazioni" Workshop reports,* 2010.

[15] L. Roso, *Proc. SPIE 8001, International Conference on Applications of Optics and Photonics,* p. 800113, 2011.

[16] G. Morou and T. Tajima, *Optics and Photonics News,* vol. 22, pp. 47-51, 2011.

[17] T. E. Cowan, J. Fuchs, H. Ruhl, A. Kemp, P. Audebert, M. Roth, R. Stephens, I. Barton, A. Blazevic, E. Brambrink, J. Cobble, J. Fernandez, J.-C. Gauthier, M. Geissel, M. Hegelich, J. Kaae, S. Karsch, G. P. L. Sage, S. Letzring, M. Manclossi, S. Meyroneinc, A. Newkirk, H. Pépin and N. Ranard-Le Galloudec, *Phys. Rev. Lett.,* vol. 92, p. 204810, 2004.

[18] P. Antici, E. Boella, S. N. Chen, M. Barberio, J. Boeker, F. Cardelli, J. L. Feugeas, M. Glesser, P. Nicolai, L. Romagnani, M. Scisciò, M. Starodubtsev, O. Willi, J. C. Kieffer, V. Tikhonschuk, H. Pépin, L. O. Silva, E. D' Humieres and J. Fuchs, *submitted to Phys. Rev. Lett.,* 2016.

[19] *Phys. Plasmas,* vol. 14, p. 030701, 2007.

[20] M. Passoni, L. Bertagna and A. Zani, *New. J. Phys.,* vol. 12, p. 045012, 2010.

[21] L. O. Silva, M. Marti, J. R. Davies, R. A. Fonseca, C. Ren, F. S. Tsung and W. B. Mori, *Phys. Rev. Lett.,* vol. 92, p. 015002, 2004.

[22] B. M. Hegelich, D. Jung, B. J. Albright, M. Cheung, B. Dromey, D. C. Gautier, C. Hamilton, S. Letzring, R. Munchhausen, S. Palaniyappan, R. Shah, H.-C. Wu, L. Yin and J. C. Fernandez, *http://arxiv.org/abs/1310.8650.*

[23] P. Antici, M. Migliorati, A. Mostacci, L. Picardi, L. Palumbo and C. Ronsivalle, *Phys. Plasmas,* vol. 18, p. 073103, 2011.

[24] P. Antici, M. Fazi, A. Lombardi, M. Migliorati, L. Palumbo, P. Audebert and J. Fuchs, *J. Appl. Phys.,* vol. 104, p. 124901, 2008.

[25] M. Barberio, M. Scisciò, S. Veltri and P. Antici, *Superlattices and Microstructures,* vol. 95, pp. 159-163, 2016.

[26] E. d'Humières, P. Antici, M. Glesser, J. Boeker, F. Cardelli, S. Chen, J. L. Feugeas, F. Filippi, M. Gauthier, A. Levy, P. Nicolai, H. Pépin, L. Romagnani, M. Scisciò, V. T. Tikhonchuk, O. Willi, J. C. Kieffer and J. Fuchs, *Plasma Phys. Control. Fusion,* vol. 55, p. 124025, 2013.

[27] K. R. Crandall and D. P. Rusthoi, *Los Alamos National Laboratory Report LA-UR-97-886,* 1997.

[28] L. M. Young, *Los Alamos National Laboratory Report LA-UR-96-1835,* 1996.

[29] S. N. Chen, M. Gauthier, D. P. Higginson, S. Dorard, F. Mangia, R. Riquier, S. Atzeni, J. R. Marques and J. Fuchs, *Rev. Sci. Instr.,* vol. 85, p. 043504, 2014.

[30] V. Scuderi, S. B. Jia, M. Carpinelli, G. A. P. Cirrone, G. Cuttone, G. Korn, T. Licciardello, M. Maggiore, D. Margarone, P. Pisciotta, F. Romano, F. Schillaci, C. Stancampiano and A. Tramontana, *Nucl. Instr. Methods Pys. Res. A,* vol. 740, pp. 87-93, 2014.

[31] M. Borghesi, A. J. Mackinnon, D. H. Campbell, D. G. Hicks, S. Kar, P. K. Patel, D. Price, L. Romagnani, A. Schiavi and O. Willi, *Phys. Rev. Lett.,* vol. 92, p. 055003, 2004.

[32] M. Borghesi, D. H. Campbell, A. Schiavi, M. G. Haines, O. Willi, A. J. MacKinnon, P. Patel, L. A. Gizzi, M. Galimberti, R. J. Clarke, F. Pegoraro, H. Ruhl and S. Bulanov, *Phys. Plasmas,* vol. 9, p. 2214, 2002.

[33] S. C. Wilks, A. B. Langdon, T. E. Cowan, M. Roth, M. Singh, S. Hatchett, M. H. Key, D. Pennington, A. MacKinnon and R. A. Snavely, *Phys. Plasmas,* vol. 8, p. 542, 2001.

[34] S. P. Hatchett, C. G. Brown, T. E. Cowan, E. A. Henry, J. S. Johnson, M. H. Key, J. A. Koch, A. B. Langdon, B. F. Lasinski, R. W. Lee, A. J. Mackinnon, D. M. Pennington, M. D. Perry, T. W. Phillips, M. Roth, T. C. Sangster, M. S. Singh, R. A. Snavely, M. A. Stoyer, S. C. Wilks and K. Yasuike, *Phys. Plasmas,* vol. 7, p. 2076, 2000.

[35] E. d'Humières, in *Laser Pulses - Theory, Technology, and Applications*, INTECH, 2012, p. Chapter 11.

[36] P. Antici, J. Fuchs, M. Borghesi, L. Gremillet, T. Grismayer, Y. Sentoku, E. d’Humières, C. A. Cecchetti, A. Mančić, A. C. Pipahl, T. Toncian, O. Willi, P. Mora and P. Audebert, *Phys. Rev. Lett.,* vol. 101, p. 105004, 2008.

[37] J. Fuchs, Y. Sentoku, E. d’Humières, T. E. Cowan, J. Cobble, P. Audebert, A. Kemp, A. Nikroo, P. Antici, E. Brambrink, A. Blazevic, E. M. Campbell, J. C. Fernández, J.-C. Gauthier, M. Geissel, M. Hegelich, S. Karsch, H. Popescu, N. Renard-LeGalloudec, M. Roth, J. Schreiber, R. Stephens and H. Pépin, *Phys. Plasmas,* vol. 14, p. 053105, 2007.

[38] P. Mora, *Phys. Rev. Lett.,* vol. 90, p. 185002, 2003.

[39] M. Kaluza, J. Schreiber, M. I. K. Santala, G. D. Tsakiris, K. Eidmann, J. Meyer-ter-Vehn and K. J. Witte, *Phys. Rev. Lett.,* vol. 93, p. 045003, 2004.

[40] S. Gaillard, J. Fuchs, N. R.-L. Galloudec and T. E. Cowan, *Rev. Sci. Instrum.,* vol. 78, p. 013304, 2007.

[41] S. Fourmaux, S. Buffechoux, B. Albertazzi, D. Capelli, A. Levy, S. Gnedyuk, L. Lecherbourg, P. Lassonde, S. Payeur, P. Antici, H. Pépin, R. S. Marjoribanks, J. Fuchs and J. C. Kieffer, *Phys. Plasmas,* vol. 20, p. 013110, 2013.

[42] S. A. E. Johansson, J. L. Campbell and K. G. Malmqvist, Particle Induced X-ray Emission Spectrometry, 1995.

[43] C. G. Ryan, D. N. Jamieson, C. L. Churms and J. V. Pilcher, *Nucl. Instr. Methods Phys. Res. B,* vol. 104, pp. 157-165, 1995.

[44] J. Salomon, J.-C. Dran, T. Guillou, B. Moignard, L. Pichon, P. Walter and F. Mathias, *Appl. Phys. A,* vol. 92, pp. 43-50, 2008.

[45] N. Grassi, P. Bonanni, C. Mazzotta, A. Migliori and P. A. Mando', *X-Ray Spectrometry,* vol. 38, pp. 301-307, 2009.

[46] P. -Y. Beauvais, in *Proceedings of EPAC*, Lucerne, Switzerland, 2004.

[47] H. Safa, in *Proceedings of the 1999 Workshop on RF Superconductivity*, Santa Fe, New Mexico, USA, 1999.

[48] *See http://www.vacuumschmelze.com/en/products/permanent-magnets-assemblies.html for commercial permanent magnets.*

[49] K. Halbach and R. F. Holsinger, *Particle Accelerators,* vol. 7, pp. 213-222, 1976.

[50] M. Scsiciò, E. d'Humières, S. Fourmaux, J. C. Kieffer, L. Palumbo and P. Antici, *Phys. Plasmas,* vol. 21, p. 123104, 2014.

[51] T. Eichner, F. Gruener, S. Becker, M. Fuchs, D. Habs, R. Weingartner, U. Schramm, H. Backe, P. Kunz and W. Lauth, *Phys. Rev. Spec. Top. - Accel. Beams,* vol. 10, p. 082401, 2007.

[52] P. McKenna, K. W. D. Ledingham, J. M. Yang, L. Robson, T. McCanny, S. Shimizu, R. J. Clarke, D. Neely, K. Spohr, R. Chapman, R. P. Singhal, K. Krushelnick, M. S. Wei and P. A. Norreys, *Phys. Rev. E,* vol. 70, p. 036405, 2004.

[53] P. Antici, Ph.D. Thesis: Laser-acceleration of high-energy short proton beams and applications, Ed. Ecole Polytechnique, 2007.

5. General conclusions and future prospects

In this thesis, I have reported the results, obtained within the time span of my doctoral studies lasting the last three years, which are strictly related to the topic of laser-driven hybrid beam lines.
The numerical results of Chapters 3 and 4 provide important information concerning the feasibility and the performance of hybrid beam lines, addressing both areas of interest of protons and electrons. The discussed analysis indicate the beam parameters that can be obtained when using laser-plasma sources, coupled with conventional transport and manipulation elements.

The results about laser-driven electron beam lines of Chapter 3 provide guidelines for research groups that attempt to use laser-generated electron beams for FEL application. The presented analysis indicates goal parameters of the laser-plasma source that need to be achieved for implementing efficient transport systems based on conventional elements.
The discussed results have been presented at the 2nd European Advanced Accelerator Concepts Workshop (Elba, Italy) in 2015 and have been published in 2016 on Journal of Applied Physics [1].
In future, we intend to collaborate with the research center INRS (Montreal, Canada), in order to implement a beam line such as those discussed in Chapter 3, although no experiments are yet planned for the near future.
Concerning the topic of laser-accelerated electrons, in June 2016, I have had the opportunity to participate to an experiment dealing with laser-plasma electron acceleration at the ALLS laser facility (located at INRS). The experiment focused on material science applications of low-energy (keV range), laser-plasma generated electrons. The obtained results have been published on Applied Physics Letters and have recently undergone peer review for Applied Surface Science with positive outcome [2] [3].

Within the frame of laser-driven proton acceleration, I have dealt with topics related to the laser-plasma acceleration process and the analysis of hybrid beam lines.
Concerning the study of the acceleration mechanism, the scientific results that we have obtained are related to numerical Particle In Cell simulations about the use of ultra-thin targets (nm thickness) for TNSA acceleration, using a ultra-high contrast laser. These results are not discussed within this thesis, which is focused on the analysis of hybrid beam lines, but have been published on Physics of Plasmas in 2014 [4].
The analysis of an hybrid proton beam line has the aim of indicating optimized parameters for the experimental implementation, since a vast quantity of parameters have to be considered (and chosen) when implementing devices such as those discussed in Chapter 4. The study that I have reported it is useful to define the features of the beam line elements that are necessary in order to obtain final beam parameters of a given quality.
Part of the numerical results of Chapter 4 have been presented at the 2nd European Advanced Accelerator Concepts Workshop (Elba, Italy) in 2015 and a manuscript addressing the calculations about the complete beam line system (energy selection and beam focusing) is currently in preparation.

The components for the optimized energy selection device, discussed in Paragraph 4.5, have been purchased and assembled at the JLF laser facility (LLNL laboratories, Livermore, USA), where I have participated to an experiment about laser-plasma proton acceleration, in August 2016. The assembled device is shown in Fig. 1.
Although, the main goal of the experimental campaign at JLF was to investigate the possibility of creating nano-structured materials via the irradiation with TNSA proton beams, we have performed preliminary calibration shots of the energy selector, using the TITAN laser system. We measured the beam displacement curve of the ES (such as the one reported in Fig. 21 of Paragraph 4.5.5) and the collected data are currently being analysed.
The implementation of the focusing stage of the proton beam line, based on PMQs, is planned for second phase, when the tests and the optimization of the ES will be completed.

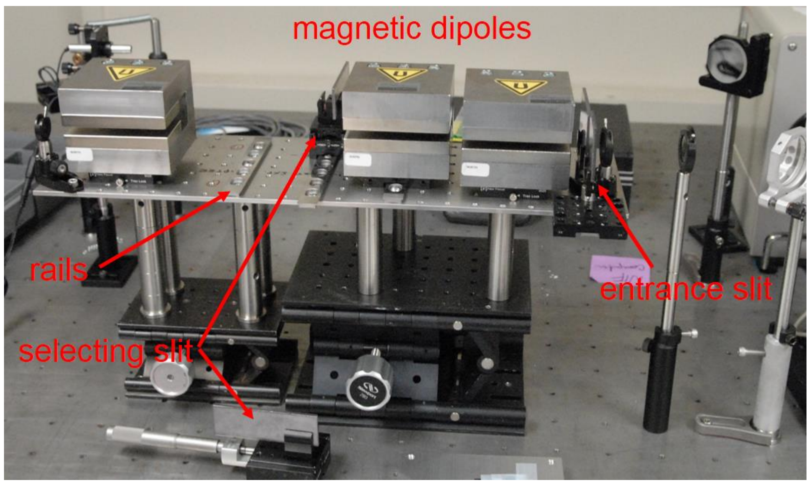

Fig. 1 – Picture of the ES as assembled at the JLF laser facility. The rails allow to move the dipoles longitudinally or transversally, in order to tune the energy selection range of the device. The selecting slit (partially unmounted) is made of a 3.5 mm thick Tantalum plate. In this picture, the 3rd dipole has been removed from the device.

We plan to test the ES in the near future (Summer 2017) using the ALLS 500 TW power laser system at INRS. The higher repetition rate of the ALLS laser (up to 10 Hz) will possibly enable to perform test shots more rapidly and correct the trajectory of the selected proton beam more efficiently than what has been possible using the TITAN laser system (with the TITAN laser only a shot every ~1-2 hours is possible).
Currently we are even looking for the possibility to test and calibrate the ES using a conventional proton accelerator, which would provide a proton beam with a better stability and quality (e.g. a lower divergence) compared to what can be obtained with laser-plasma acceleration.

The results discussed in this work are promising for the future implementation of laser-plasma particle acceleration schemes. On the other hand, there are numerous issues that still remain open and that the scientific community still needs to face. However, the striving for innovative applications based on compact particle accelerators, motivates and confers merit to the research activity of many physicist and engineers, all over the world. The work I have presented in this thesis will hopefully contribute to an advance in this challenging but fascinating field of science.

References

[1] M. Scisciò, L. Lancia, M. Migliorati, A. Mostacci, L. Palumbo, Y. Papaphilippou and P. Antici, *J. Appl. Phys.,* vol. 119, p. 094905, 2016.

[2] S. Veltri, M. Barberio, C. Liberatore, M. Scisciò, A. Laramée, L. Palumbo, F. Legaré and P. Antici, *Appl. Phys. Lett.,* vol. 110, p. 021114, 2017.

[3] M. Scisciò, M. Barberio, C. Liberatore, S. Veltri, A. Laramée, L. Palumbo, F. Legaré and P. Antici, *Appl. Surf. Sci. (in press),* 2017.

[4] M. Scisciò, E. d'Humières, S. Fourmaux, J. C. Kieffer, L. Palumbo and P. Antici, *Phys. Plasmas,* vol. 21, p. 123104, 2014.

Appendix I

Particle beam emittance

The emittance of an accelerated particle beam is an important parameter in order to define the geometric features of the beam itself, for both the cases of electron and proton beams. Moreover, it often represents a constraint for beam quality for several applications: a low beam emittance is required, for instance, when dealing with particle colliders requiring high luminosity (protons and electrons), synchrotron light sources and accelerators driving Free Electron Lasers (electrons).
Here we report the basic concepts of geometric emittance and RMS emittance. The physical concepts that we discuss are typical of conventional accelerators, but can be extended to laser-plasma particle sources, too. In particular, the research results of Chapter 3, are strongly linked to the concept of beam emittance related to the characteristics of laser-accelerated electron beams, with a particular attention the specific application of FEL sources.
The topics discussed in Paragraphs I.I to I.III general concepts of accelerated particle beam dynamics, hence no particular references are indicated. The topic of Paragraph I.IV is referred to the study of Migliorati et al., published on Phys. Rev. ST – Accel. Beams in 2013 (see the Appendix's references).

I.I The geometric emittance

For an accelerated particle beam we can define the transverse position and transverse momentum of each particle of the bunch as x and x'(here in the x direction being the transverse plane $x-y$), respectively. The transverse momentum x' (i.e. the divergence of the particle) is $x' = p_x/p_z$, with p_x the momentum in the transverse direction and p_z the momentum in longitudinal direction.

The motion of the particles in the transverse plane is described by the Hill's equation:

$$x''(s) + K(s)x(s) = 0\,, \tag{1}$$

Where s is the longitudinal position of the particles.

The general solution of the Hills equation is

$$x(s) = \sqrt{\varepsilon}\sqrt{\beta(s)}\cos(\phi(s)\,, \tag{2}$$

$$x'(s) = -\frac{\sqrt{\varepsilon}}{\beta(s)}\{\alpha(s)\cos(\varphi(s)+\phi) + \sin(\varphi(s)+\phi)\}\,, \tag{3}$$

With ε and and ϕ integration constants given by the initial conditions.

From Eq. 2 and 3 it is possible to derive the quantity

$$\varepsilon = \gamma(s)x(s)^2 + 2\alpha(s)x(s)x'(s) + \beta(s)x'(s)^2 \,, \tag{4}$$

with

$$\alpha(s) = -\frac{1}{2}\beta'(s) \,, \tag{5}$$

$$\gamma(s) = \frac{1+\alpha(s)^2}{\beta(s)} \tag{6}$$

If we consider a transverse phase space $x - x'$, ε is the parametric representation of an ellipse, as reported in Fig. 1.

α, β and γ, called Twiss parameters, describe the shape of the ellipse in the phase space and, hence, the geometric characteristics of the particle in the transverse plane. The area of the ellipse described by ε is a Courant-Snyder invariant [1] [2] and represents the geometric emittance of the particle beam, i.e. the area that is occupied by the particles of the beam in the $x - x'$ plane. The quantityε, is constant if the particles of the beam are not accelerated (i.e. the longitudinal momentum is constant) and the forces acting on the particles are linear (i.e. they scale linearly with the transverse position of the particles, e.g. such as in a magnetic quadrupole).

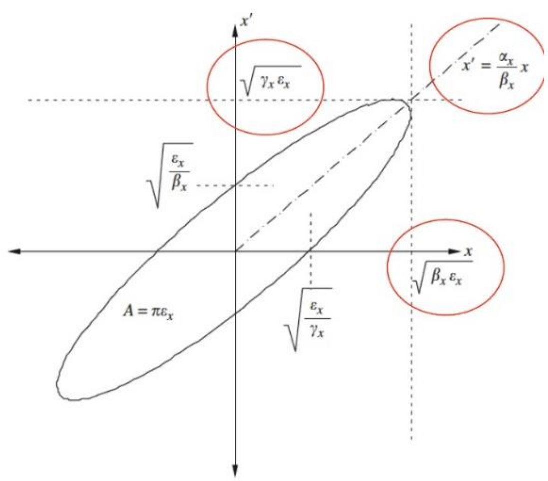

Fig. 9 – Phase space ellipse on the transverse plane x-x'. The beam transverse dimension and the divergence are given by the Twiss parameters α, β and γ. The area covered by the ellipse is represents the geometric emittance ε of the beam.

We can define the transverse dimension of the beam (i.e. the spot-size) as the width σ_x of the beam in the phase space and the divergence σ'_x of the beam (i.e. the maximum transverse momentum of the particles) as the high of the ellipse. As shown in Fig. 1, it is that

$$\sigma_x = \sqrt{\beta\varepsilon}\ , \tag{7}$$

$$\sigma'_x = \sqrt{\gamma\varepsilon}\ . \tag{8}$$

The geometric characteristics of the beam are defined by the Twiss parameters and the quantity ε is the geometric emittance of the particle beam, representing the area of the phase space ellipse.

I.II The normalized RMS emittance

The geometric emittance discussed so far can be used to characterize particle beams that are not under the influence of non-linear forces. When, for example, space charge effects or other non-linear effects are significant, the area occupied by the beam in the transverse phase space becomes distorted and the representation using the ellipse area is not accurate. In such cases, it is more useful to use an alternative definition of beam emittance.
The root-mean-square (RMS) envelope of the beam in the phase space is a more accurate indicator of the beam's characteristics when the area does not have an ellipse shape. It is possible to define a RMS beam emittance as

$$\varepsilon_{rms} = \gamma x + 2\alpha x x' + \beta x'^2\ . \tag{9}$$

We indicate, as it follows, the beam RMS transverse dimension and divergence by redefining σ_x and σ'_x .

Since the relationship $\alpha = -\frac{\beta'}{2}$ is still valid, we can write

$$\alpha = -\frac{1}{2\varepsilon_{rms}}\frac{d}{dz}\langle x^2\rangle = -\frac{\langle x x'\rangle}{\varepsilon_{rms}} = -\frac{\sigma_{xx'}}{\varepsilon_{rms}}$$

Obtaining the quantities

$$\sigma_x = \sqrt{\langle x^2\rangle} = \sqrt{\beta\varepsilon_{rms}}\ ,$$

$$\sigma'_x = \sqrt{\langle x'^2\rangle} = \sqrt{\gamma\varepsilon_{rms}}\ ,$$

$$\sigma_{xx'} = \langle x x'\rangle = -\alpha\varepsilon_{rms}\ .$$

The quantities in the triangular brackets represent the RMS values of the transverse dimension and transverse divergence of the beam, averaged over all the particles of the bunch.

Being that the relationship $\gamma\beta - \alpha^2 = 1$ holds, we can substitute α, β and γ in the expressions above and write that

$$\frac{\sigma_{x'}^2}{\varepsilon_{rms}}\frac{\sigma_x^2}{\varepsilon_{rms}} - \left(\frac{\sigma_{xx'}}{\varepsilon_{rms}}\right)^2 = 1$$

Finally we can express the RMS emittance that we defined before (Eq. 9) as

$$\varepsilon_{rms} = \sqrt{\sigma_x^2\sigma_{x'}^2 - \sigma_{xx'}^2} = \sqrt{\left(\langle x^2\rangle\langle x'^2\rangle - \langle xx'\rangle^2\right)}\,. \tag{10}$$

We have obtained a definition of emittance in terms of the second moments of a transverse particle distribution that is not necessarily represented by an ellipse in the phase space. This definition of emittance allows characterizing the particle beam in terms of the statistical distribution (RMS distribution) of the particles on the transverse plane $x - x'$.

Now we can define the normalized emittance $\varepsilon_{n,rms}$, taking into account the energy of the accelerated particle beam:

$$\varepsilon_{n,rms} = \sqrt{\sigma_x^2\sigma_{p_x}^2 - \sigma_{xp_x}^2} = \frac{1}{m_0 c}\sqrt{\left(\langle x^2\rangle\langle p_x^2\rangle - \langle xp_x\rangle^2\right)} \approx \langle\beta\gamma\rangle\varepsilon_{rms}\,. \tag{11}$$

The approximation giving the last expression on the right hand side assumes that $p_z \approx p$, i.e. the momentum of the particles p has a negligible component in transverse direction and the main contribution comes from the longitudinal component p_z. Being $x' = p_x \,/\, p_z$, it follows that

$$p_x = p_z x' = m_0 c\beta\gamma x'$$

which allows to obtaining the conventional (i.e. the most commonly used definition in the case conventionally accelerated particle beams) definition of normalized emittance as

$$\varepsilon_n = \beta\gamma\varepsilon\,, \tag{12}$$

which is used for both the geometric normalized emittance $\varepsilon_{n,g}$ (using Eq. 4) and the RMS normalized emittance $\varepsilon_{n,rms}$ (Eq. 11).

I.III Energy spread contribution to the normalized emittance growth

The expression of Eq. 11 can be rewritten as

$$\varepsilon_n^2 = \langle x^2\rangle\langle \beta^2\gamma^2 x'^2\rangle - \langle x\beta\gamma x'\rangle^2 \, , \tag{12}$$

where $\beta = v\,/\,c$, with v the velocity of the particles and c the speed of light. γ is the relativistic factor of the particles, x and x' the transverse position and divergence of the particles, respectively.
If there is no correlation between the energy of the particles and their transverse position (or the correlation is negligible), the term can be written as

$$\varepsilon_n^2 = \langle \beta^2\gamma^2\rangle\langle x^2\rangle\langle x'^2\rangle - \langle\beta\gamma\rangle^2\langle xx'\rangle^2 \, . \tag{13}$$

This is the case, for instance, of a beam traveling through a drift space without significant collective effects (i.e. effects between the single particles of the bunch).

By considering the definition of RMS energy spread of an accelerated particle bunch

$$\sigma_E^2 = \frac{\langle \beta^2\gamma^2\rangle - \langle\beta\gamma\rangle^2}{\langle\gamma\rangle^2} \, , \tag{14}$$

the normalized RMS emittance of a particle beam can be written as

$$\varepsilon_n^2 = \langle\gamma\rangle^2(\sigma_E^2\sigma_x^2\sigma_{x'}^2 + \varepsilon^2) \tag{15}$$

From Eq. 15, one can see that the first addend of the parenthesis on the right contains a term related to the energy spread of the beam. A high divergence $\sigma_{x'}$ leads to a growth of the beam transverse dimension σ_x and the addend on the left becomes dominant.
This will lead to the effect of an emittance growth even for a beam traveling through a free drift, if the energy spread σ_E is high, compared to the un-normalized emittance ε.

I.IV Emittance growth in laser-accelerated electron beams

In the case of laser-driven electron beam, the high energy spread at the laser-plasma source, leads to an effect of emittance growth that makes it challenging to keep the quality of the beam unaltered after an even short distance from the laser-plasma interaction point.

The growth of normalized emittance in the case of laser-accelerated electron beams is an effect that is taken into account and studied into detail in Chapter 3, where electron transport beam lines are analyzed. In order to better understand the results that will be presented in Chapter 3, we discuss here emittance evolution of a laser-driven electron beam in an empty drift space and when traveling through the magnetic devices of a transport system.

In the case of conventional electron accelerators, the first term of the parenthesis is negligible (the energy spread of conventional machines typically is below 0.1 %). Typically the electron are injected into the accelerating structure of an accelerator from a photo-injector: electrons are extracted from a photo-cathode with an energy of a few eV and are immediately accelerated by an electric field up to energies in the range of MeV. If the transverse momentum of the particle remains constant during the acceleration, the divergence of the beam is reduced by a factor 10^6, being the divergence $x' = p_x/p_z$ with p_x the transverse momentum of the particle and p_z the longitudinal momentum of the particle.

On the other hand, in a laser-plasma accelerator this effect is less efficient: the electrons stem out from a plasma region where strong focusing magnetic fields keep the bunch collimated but as soon as the particles leave the plasma and enter an empty drift space, the focusing force expires. The acceleration process takes place entirely in the plasma region, hence there is no accelerating field that can compensate the absence of the focusing force, reducing the beam divergence (as it is the case for a conventional photo-injector. This effect has been studied by Migliorati et al. [3], showing the intrinsic emittance growth of a laser-accelerated electron beam traveling in an empty drift space, as reported in Fig. 2 (top left plot).

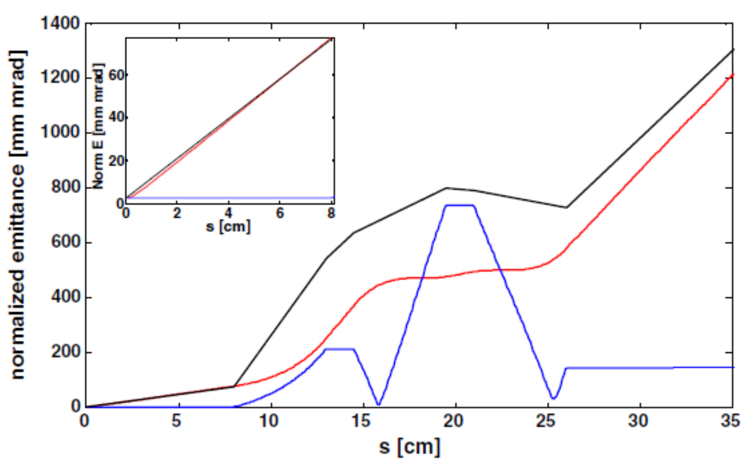

Fig. 2 – Normalized transverse emittance along a transport line using magnetic quadrupoles: comparison between TSTEP simulations (red curve), Eq. 9 (black curve) and the $\beta\gamma\varepsilon$ approximation (blue curve). Inset: zoom of the initial drift. Extracted from Ref. [3].

Moreover, when using magnetic devices to capture and transport the beam from the source, the high energy spread within the electron bunch leads to chromatic effects. Laser-accelerated electron beams typically have an energy spread that is orders of magnitude higher than what is obtained on conventional facilities. Typical values are in the range of a few percent (conventional linear accelerators easily deliver electron beams with less than 0.1 % energy spread).

The plot in Fig. 2 show the behavior, from the point of view of the normalized emittance, of a laser-accelerated electron beam that passes through a focusing system made of magnetic quadrupoles. The energy spread of the beam causes chromatic effects that increase the value of the first term of the parenthesis of Eq. 15 (red and black curve). The blue curve represents the value of normalized emittance evaluated with the approximation $\varepsilon_n = \beta\gamma\varepsilon$, which is commonly used for conventional machines. This approximation yields reliable results only if the energy spread and the transverse momentum of the beam are low enough, i.e. the first term in the parenthesis of Eq. 15 can be neglected.

For these reasons, the value of the normalized emittance grows intrinsically in the case of laser-accelerated electron beams and the implementation of an efficient transport line that keeps its value under control is challenging.

The effect of normalized emittance growth can be studied in detail with particle tracking simulations (see Paragraph 2.1) such as those we discuss in Chapter 3, since they can give an insight into the particle distribution of the bunch and its evolution along the transport line.

References

[1] E. Courant e H. Snyder, *Annals of Physics,* vol. 3, p. 1, 1958.

[2] S. Y. Lee, in *Accelerator Physics*, Singapore, World Scientific, 1999, p. 47.

[3] M. Migliorati, A. Bacci, C. Benedetti, E. Chiadroni, M. Ferrario, A. Mostacci, L. Palumbo, A. R. Rossi, L. Serafini e P. Antici, *Phys. Rev. Spec. Top. - Accel. Beams,* vol. 16, p. 011302, 2013.

Appendix II

Working point maps of the energy selector, obtained with TSTEP

In this appendix we report the working point maps of the energy selector, such as the one of Fig. 17 in Paragraph 4.5.4. The method that we have used for obtaining them is explained in Paragraph 4.5.4.

The maps in this appendix have been used for defining the optimal parameters of the ES in the energy range 2-20 MeV, as reported in Paragraph 4.5.5.
Although the data we report here address 5 MeV as the lowest energy, the performance of the ES was not expected to worsen for lower energies. The results of Paragraph xxx confirm this hypothesis.

All the working point maps indicate the dipole length l_d in cm on the x-axis and the magnetic field intensity B_y in Tesla on the y-axis. The color-scale indicates the energy spread $\Delta E/E$ (FWHM) in percent.
The selecting slit that has been simulated has a width of 500 µm for all simulations. The initial divergence of the incoming beam is indicated for the different cases.

The efficiency that is reported is calculated as defined in Eq. 4.3 of Paragraph 4.5. It is important to remember that the efficiency refers to the ES only, i.e. the losses from the entrance slit are not taken into account. For the efficiency of the complete beam line, see the results of Paragraph 4.6.2.

5 MeV central energy

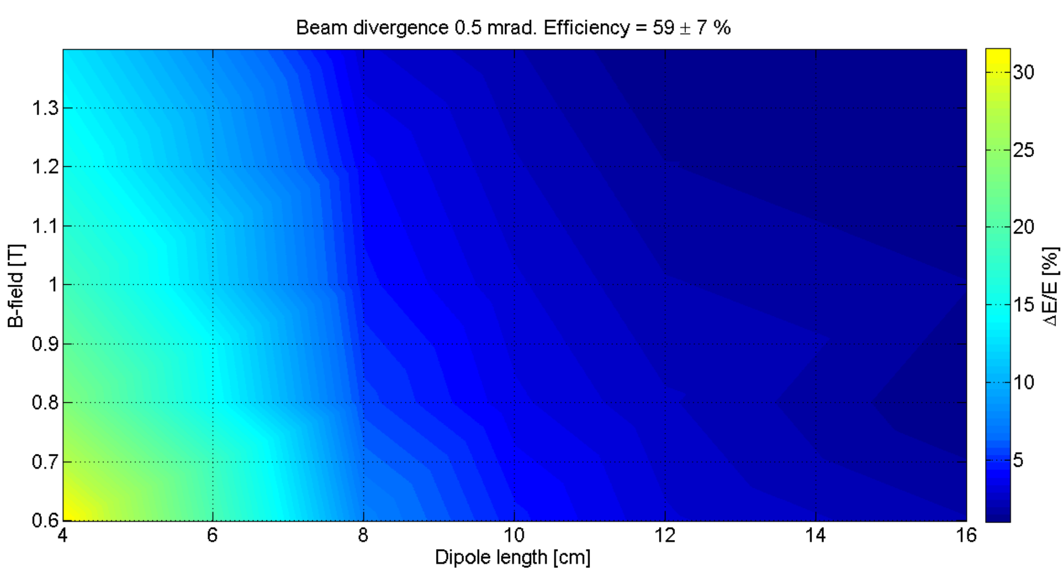

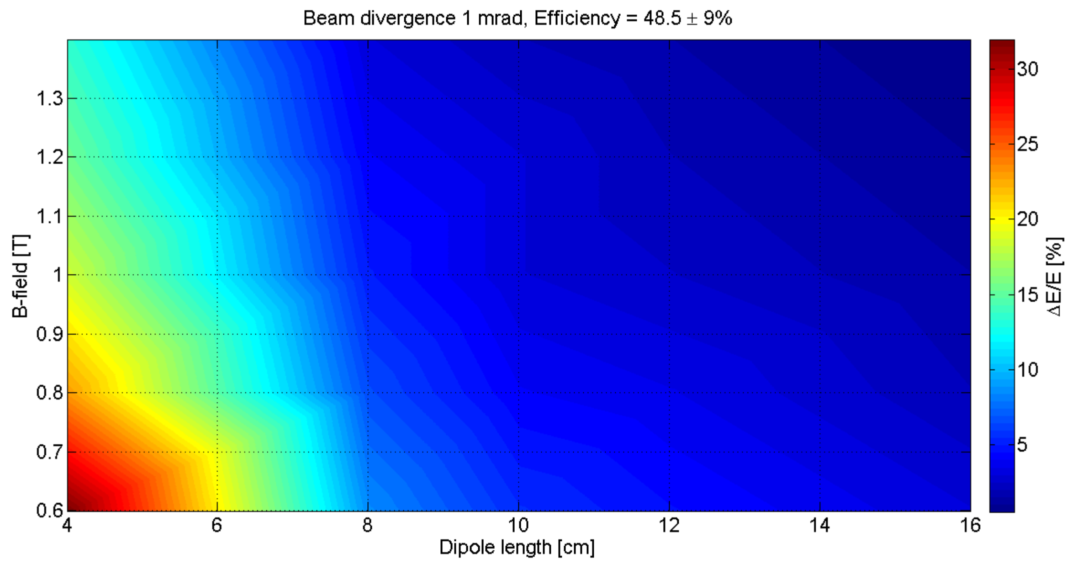
Beam divergence 1 mrad, Efficiency = 48.5 ± 9%
B-field [T]
Dipole length [cm]
ΔE/E [%]
4
6
8
10
12
14
16
0.6
0.7
0.8
0.9
1
1.1
1.2
1.3
5
10
15
20
25
30

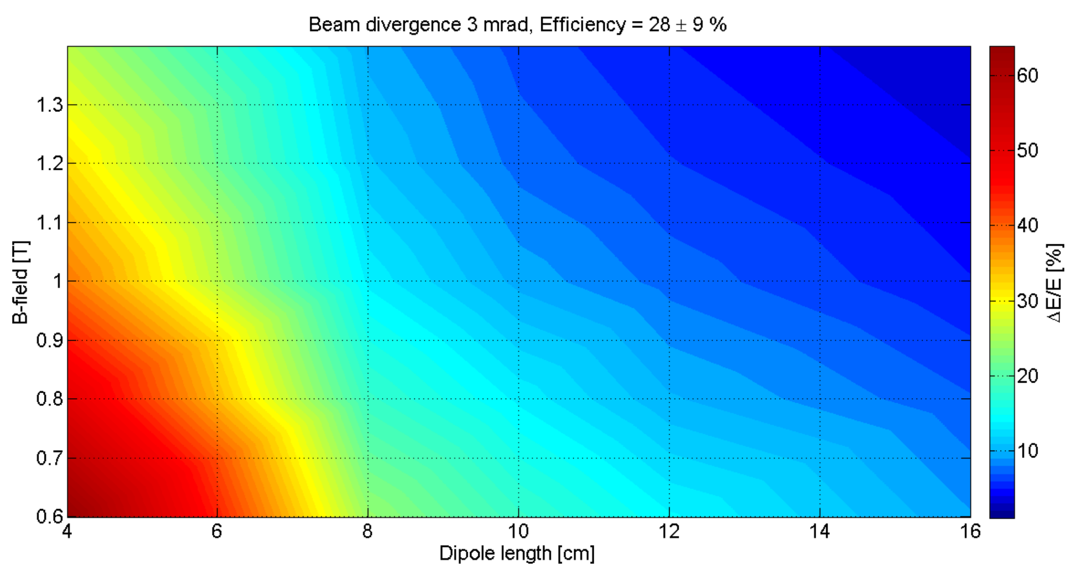
Beam divergence 3 mrad, Efficiency = 28 ± 9 %
B-field [T]
Dipole length [cm]
ΔE/E [%]
4
6
8
10
12
14
16
0.6
0.7
0.8
0.9
1
1.1
1.2
1.3
10
20
30
40
50
60

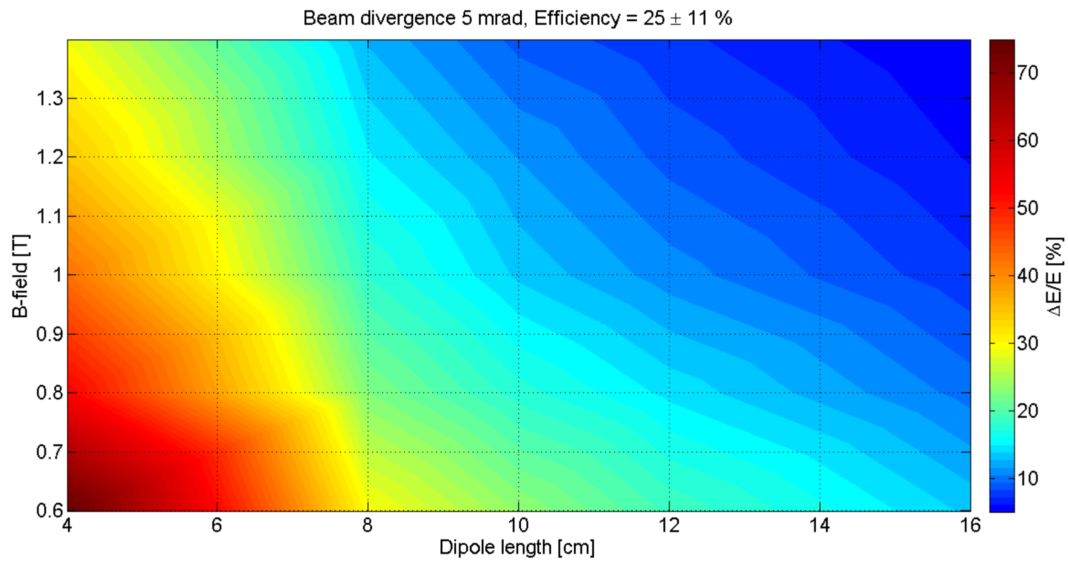

10 MeV central energy

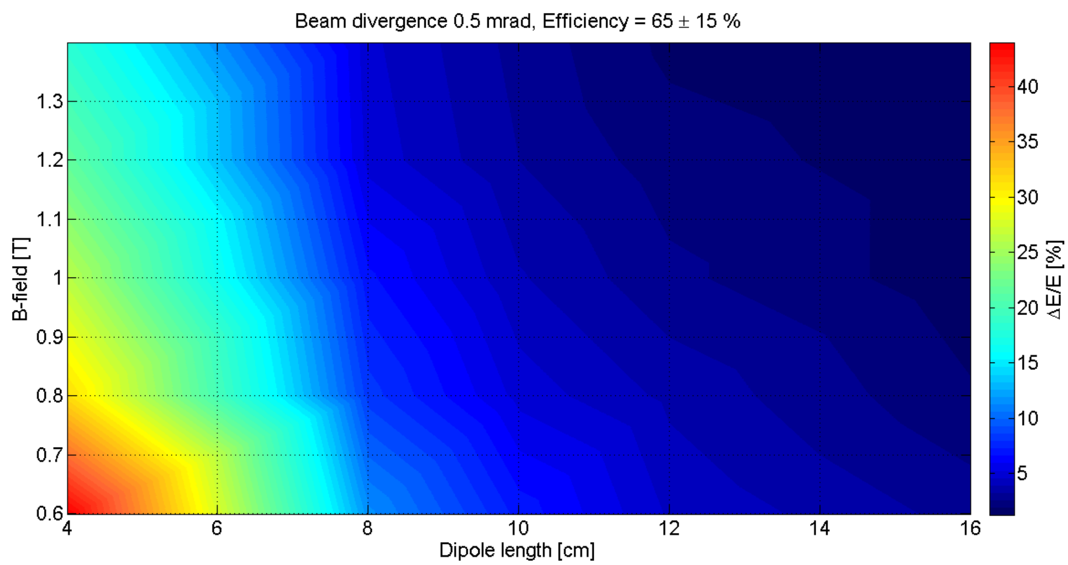

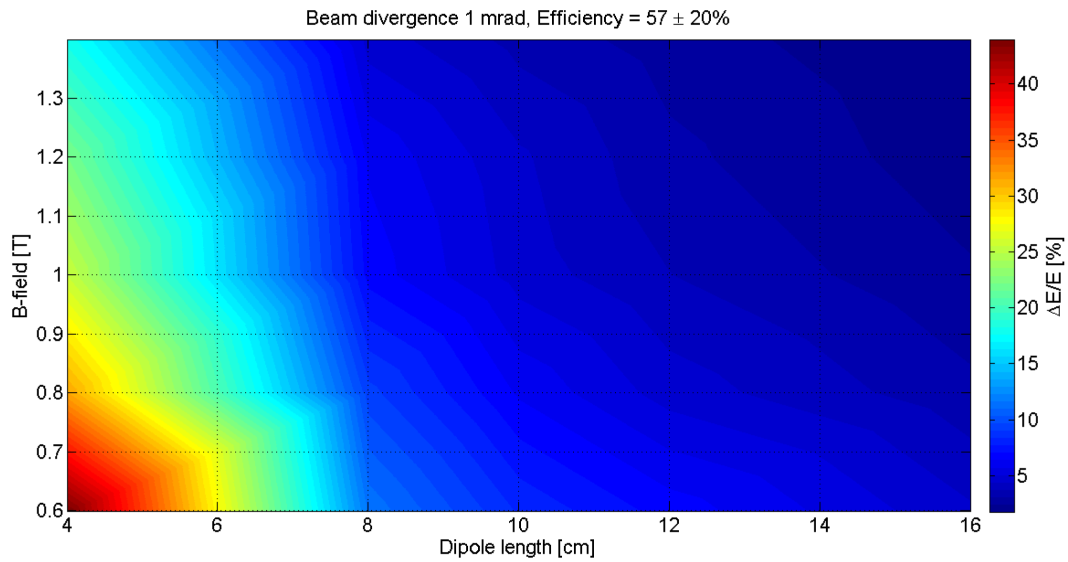
Beam divergence 1 mrad, Efficiency = 57 ± 20%
B-field [T]
Dipole length [cm]
ΔE/E [%]

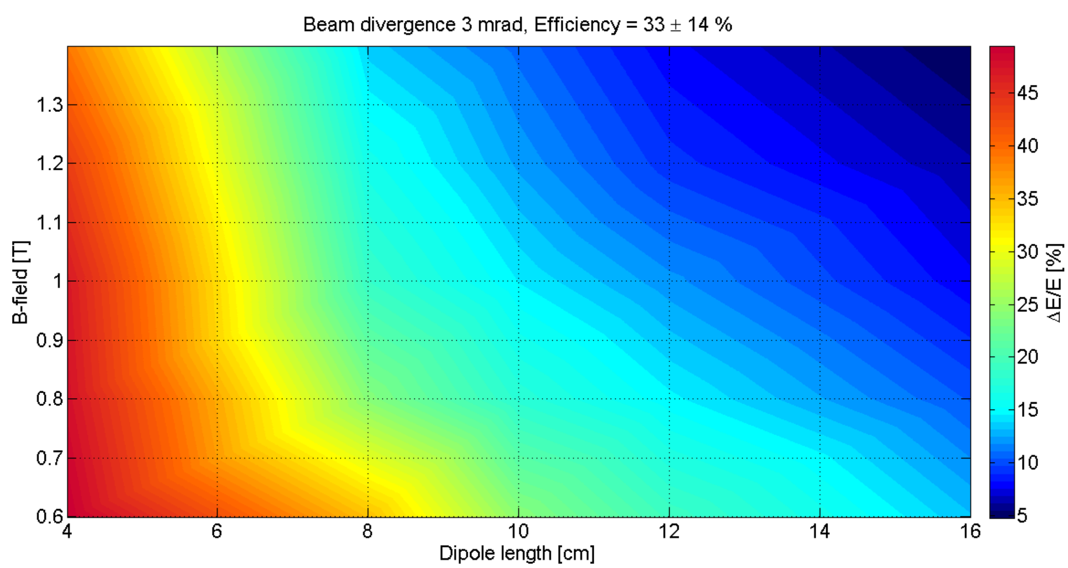
Beam divergence 3 mrad, Efficiency = 33 ± 14 %
B-field [T]
Dipole length [cm]
ΔE/E [%]

Beam divergence 5 mrad, Efficiency = 29 ± 16 %

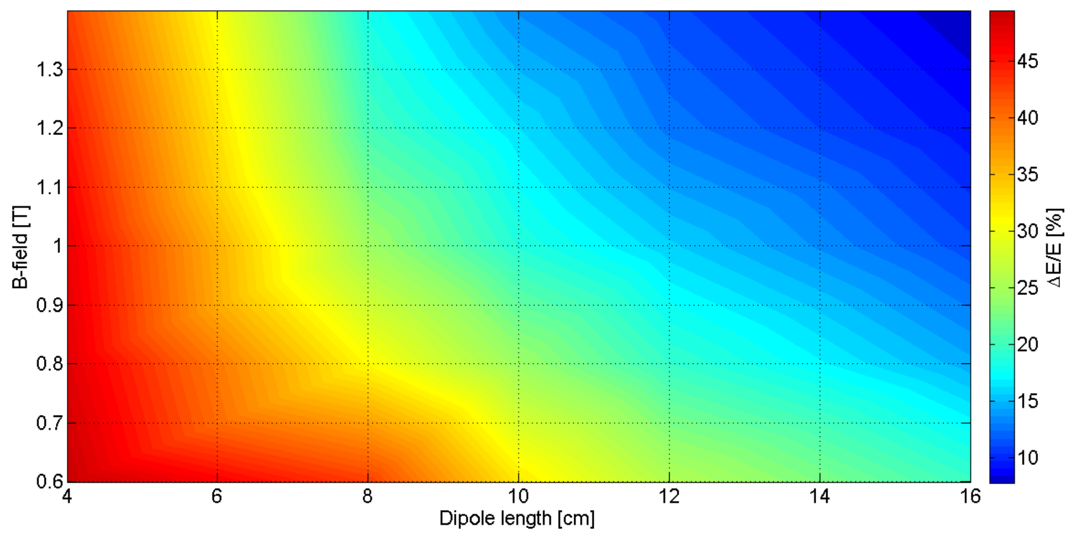

20 MeV central energy

Beam divergence 0.5 mrad, Efficiency = 62 ± 12 %

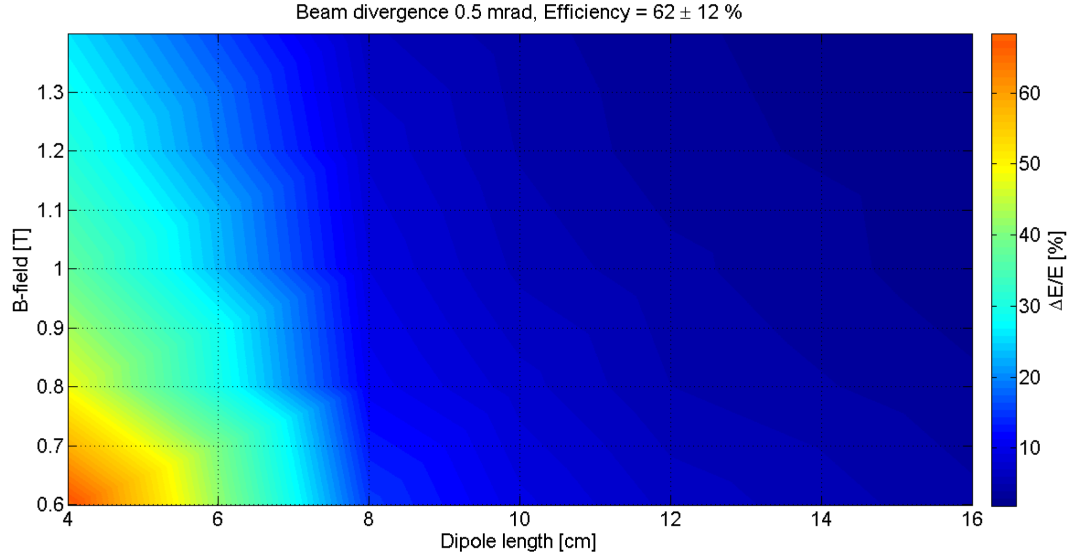

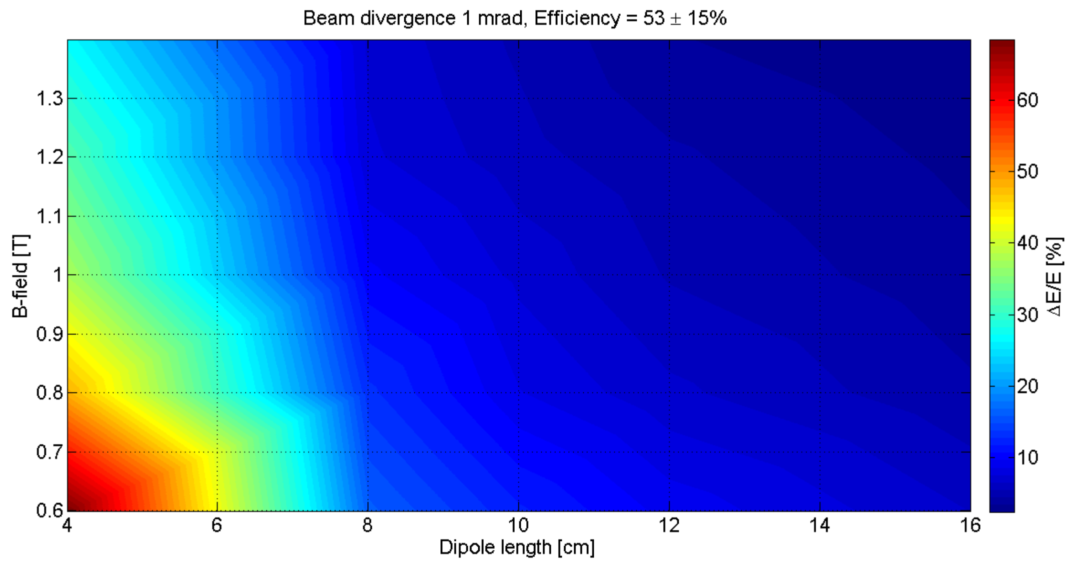

Beam divergence 1 mrad, Efficiency = 53 ± 15%
B-field [T]
Dipole length [cm]
ΔE/E [%]
0.6
0.7
0.8
0.9
1
1.1
1.2
1.3
4
6
8
10
12
14
16
10
20
30
40
50
60

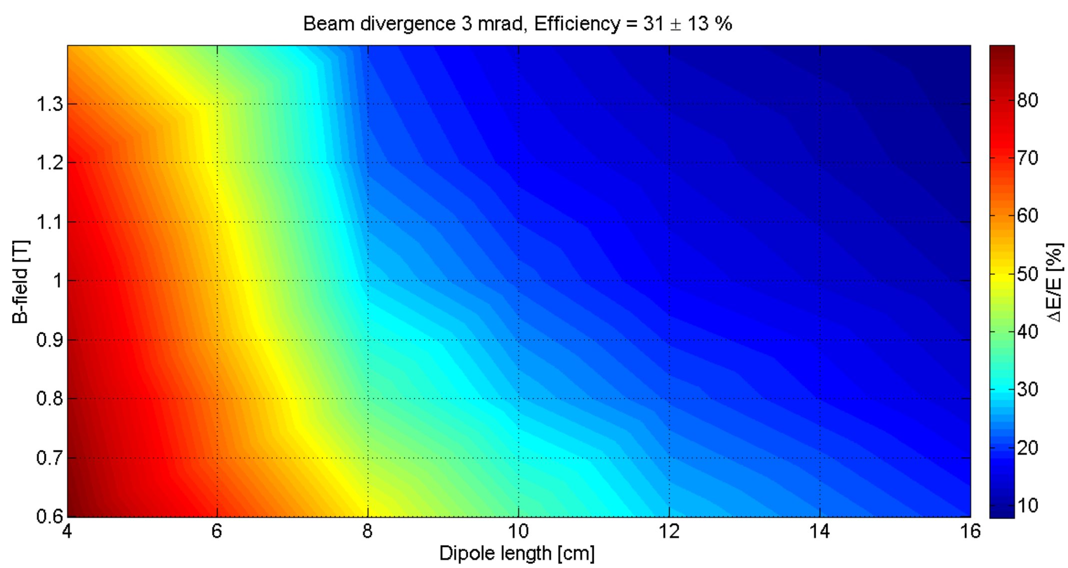

Beam divergence 3 mrad, Efficiency = 31 ± 13 %
B-field [T]
Dipole length [cm]
ΔE/E [%]
0.6
0.7
0.8
0.9
1
1.1
1.2
1.3
4
6
8
10
12
14
16
10
20
30
40
50
60
70
80

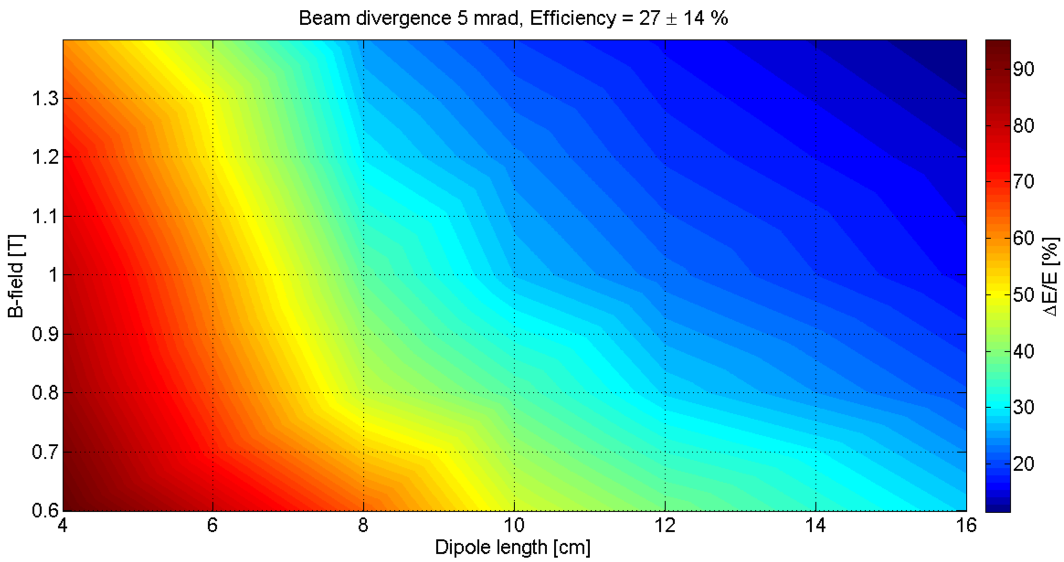
Beam divergence 5 mrad, Efficiency = 27 ± 14 %
B-field [T]
1.3
1.2
1.1
1
0.9
0.8
0.7
0.6
4
6
8
10
12
14
16
Dipole length [cm]
ΔE/E [%]
90
80
70
60
50
40
30
20

Appendix III

Optimized lattice configurations of the laser-driven beam line's focusing stage for different energies

In this appendix we report the schemes of the lattice structures, based on permanent magnet quadrupoles, that we have used for the simulations of the laser-driven proton beam line.
The spacing between the quadrupoles needs to be optimized according to the central energy of the beam line, i.e. the central energy selected by the energy selector. The optimization of the focusing stage for different energies that we show in this appendix, has been obtained with the beam optics code TRACE3D.

All the quadrupoles that have been used are of the type discussed in Paragraph 4.6.1. The magnetic length of all the quadrupoles is 3 cm.
The quadrupoles indicated with the blue squares (Q1) have a magnetic gradient of 160 T/m and a bore radius of 1 cm. The quadrupoles indicated with the grey squares (Q2) have a magnetic gradient of 300 T/m and a bore radius of 0.5 cm.
The sign "-" in the squares indicates a defocusing quadrupole.

3 MeV beam line

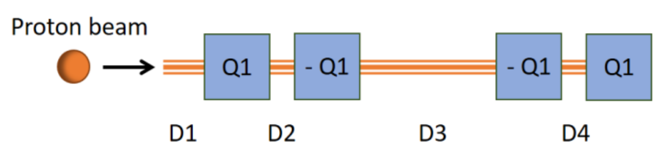

D1 = 0.25 cm
D2 = 0.1 cm
D3 = 0.6 cm
D4 = 0.1 cm

5 MeV beam line

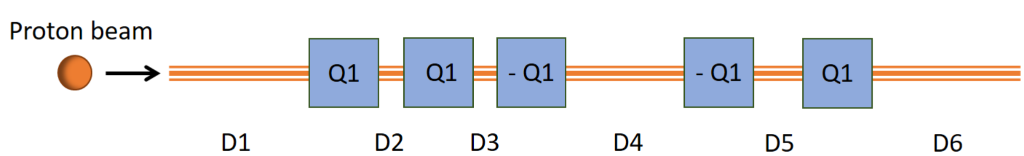

D1 = 3.1 cm
D2 = 0.1 cm
D3 = 0.1 cm
D4 = 0.7 cm
D5 = 0.45 cm
D6 = 8.0 cm

10 MeV beam line

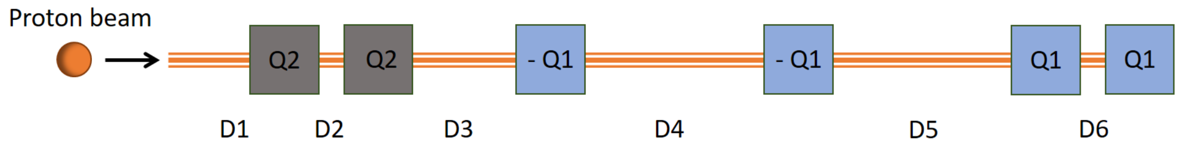

D1 = 1.9 cm
D2 = 0.1 cm
D3 = 2.2 cm
D4 = 5.1 cm
D5 = 5.9 cm
D6 = 0.1 cm

20 MeV beam line

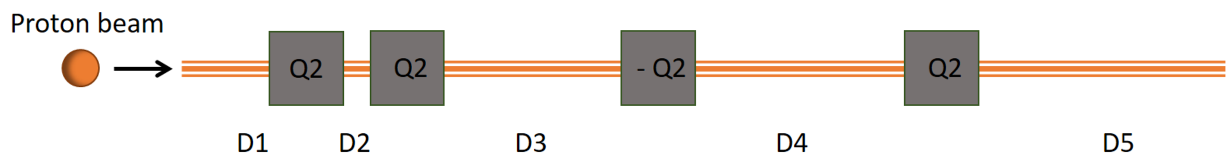

D1 = 3.8 cm
D2 = 0.1 cm
D3 = 6.7 cm
D4 = 9.7 cm
D5 = 50 cm